Search for physics beyond the Standard Model in photon + missing transverse momentum final state in proton-proton collisions, using the Compact Muon Solenoid detector at the Large Hadron Collider, and study of Calorimetry for High Energy Physics experiments

By

Ashim Roy

PHYS05201204005

Saha Institute of Nuclear Physics, Kolkata

A thesis submitted to the

Board of Studies in Physical Sciences

In partial fulfillment of requirements

For the Degree of

DOCTOR OF PHILOSOPHY

of

HOMI BHABHA NATIONAL INSTITUTE

June, 2018

Homi Bhabha National Institute[1]

Recommendations of the Viva Voce Committee

As members of the Viva Voce Committee, we certify that we have read the dissertation prepared by **Ashim Roy** entitled **Search for physics beyond the Standard Model in photon + missing transverse momentum final state in proton-proton collisions, using the Compact Muon Solenoid detector at the Large Hadron Collider, and study of Calorimetry for High Energy Physics experiments** and recommend that it maybe accepted as fulfilling the dissertation requirement for the Degree of Doctor of Philosophy.

_____ Date:
Chair - Prof. Satyajit Saha

_____ Date:
Guide/Convener - Prof. Satyaki Bhattacharya

_____ Date:
Co-Guide - Prof. Manoj Sharan

_____ Date:
Examiner - Prof. B.K. Nandi

_____ Date:
Member 1 - Prof. Debashis Majumdar

_____ Date:
Member 2 - Prof. Subir Sarker

Final approval and acceptance of this dissertation is contingent upon the candidate's submission of the final copies of the dissertation to HBNI.

We hereby certify that we have read this dissertation prepared under our direction and recommend that it may be accepted as fulfilling the dissertation requirement.

Date:
Place:

_____ Co-guide

_____ Guide

[1]This page is to be included only for final submission after successful completion of viva voce.

STATEMENT BY AUTHOR

This dissertation has been submitted in partial fulfillment of requirements for an advanced degree at Homi Bhabha National Institute (HBNI) and is deposited in the Library to be made available to borrowers under rules of the HBNI.

Brief quotations from this dissertation are allowable without special permission, provided that accurate acknowledgement of source is made. Requests for permission for extended quotation from or reproduction of this manuscript in whole or in part may be granted by the Competent Authority of HBNI when in his or her judgment the proposed use of the material is in the interests of scholarship. In all other instances, however, permission must be obtained from the author.

Ashim Roy

DECLARATION

I, hereby declare that the investigation presented in the thesis has been carried out by me. The work is original and has not been submitted earlier as a whole or in part for a degree / diploma at this or any other Institution / University.

Ashim Roy

List of Publications arising from the thesis

Journal

1. "Simulation study of energy resolution, position resolution and π^0-γ separation of a sampling electromagnetic calorimeter at high energies", **Ashim Roy**, Shilpi Jain, Gobinda Majumder, Satyaki Bhattacharya and Sunanda Banerjee, *JINST 12* (**2017**) *P07013* [arXiv: 1703.05246 [physics.ins-det]]
doi: 10.1088/1748-0221/12/07/P07

2. "Search for new physics in the monophoton final state in proton-proton collisions at $\sqrt{s} = 13$ TeV", The CMS Collaboration,
JHEP (**2017**) *1710* 073, [arXiv: 1706.03794 [hep-ex]]
doi: 10.1007/JHEP10(2017)073

3. "Measurement of the $Z\gamma \to \nu\bar{\nu}\gamma$ production cross section in pp collisions at $\sqrt{s} = 8$ TeV and limits on anomalous $ZZ\gamma$ and $Z\gamma\gamma$ trilinear gauge boson couplings", The CMS Collaboration,
Phys. Lett. (**2016**) *B760*, 448-468, [arXiv:1602.07152 [hep-ex]]
doi: 10.1016/j.physletb.2016.06.080

Conferences

4. "Simulation of π^0-γ Separation Study for Proposed CMS Forward Electromagnetic Calorimeter", **Ashim Roy**, Shilpi Jain, Gobinda Majumder, Satyaki Bhattacharya and Sunanda Banerjee,
XXVII IUPAP Conference on Computational Physics (CCP2015), Guwahati (India),
Journal of Physics: Conference Series **(2016)** *759* 01207
doi: 10.1088/1742-6596/759/1/0120

5. "Search for Dark Matter and Large Extra Dimensions in the photon + MET final state in pp Collisions at $\sqrt{s} = 13$ TeV", **Ashim Roy**,
XXII DAE-BRNS High Energy Physics Symposium, 12-16 Dec 2016, University of Delhi, Delhi (India),
Springer Proceedings in Physics (**2018**) *203* 205-208
doi: 10.1007/978-3-319-73171-1_46

Others

6. "Search for Dark Matter and Large Extra Dimensions in the γ + MET final state in pp Collisions at $\sqrt{s} = 13$ TeV", The CMS Collaboration, *CMS PAS EXO-16-014*

7. "Measurement of the production cross section for $pp \to Z\gamma \to \nu\bar{\nu}\gamma$ at $\sqrt{s} = 13$ TeV at CMS", The CMS Collaboration, *CMS PAS SMP-16-004*

8. "First beam tests of prototype silicon modules for the CMS High Granularity Calorimeter", The CMS Collaboration, *CMS Detector note: DN-17-011*

9. "Search for dark matter and large extra dimensions in monophoton final state using 2016 data", A. Askew, B. Allen, S. Bhattacharya, J. Buchanan, S. Dasu, S. Ghosh, B. Gomber, Y. Iiyama, D. Kovalskyi, C. Paus, **A. Roy**, and M. Tripathi, *CMS Analysis note: AN-16-475*

Ashim Roy

DEDICATIONS

To my parents and my brothers,
who have educated me and enabled me
to come this far in life.

ACKNOWLEDGEMENTS

This work was carried out during the years 2013-2017 at the Saha Institute of Nuclear Physics (SINP), at the European Organization for Nuclear Research (CERN) and at the Fermi National Accelerator Laboratory (Fermilab).

First of all, I express my sincere gratitude to my supervisor Prof. Satyaki Bhattacharya for his continuous support during my Ph.D., for his patience, motivation, and immense knowledge. His guidance has helped me throughout the time of research and writing of this thesis.

I would like to express my deepest gratitude to Prof. Sunanda Banerjee for his guidance and support. I am deeply grateful to him for his numerous help in all aspects of my thesis work, specially during my visit to Fermilab. I have been fortunate to work with him closely. I am also thankful to the joint-supervisor of my thesis, Prof. Manoj Kumar Sharan, for his help, co-operation and encouragement throughout my Ph.D tenure.

I would like to thank Prof. Gobinda Majumder for valuable discussions on Shashlik paper. I would like to acknowledge Prof. Subir Sarkar, who helped me a lot regarding coding, computation and administrative support at SINP. I am also thankful to Prof. Suchandra Dutta for helping me during tracker DQM shifts.

My earnest thanks to Shilpi di who helped me a lot in each and every step during my Ph.D. work. I am thankful to Savvas for helping me in the Photon-ID tuning work. I am thankful to Prof. Andrew Askew for his valuable discussions and suggestions on the mono-photon analysis work. I would like to thank to my senior Bhawna and junior Shamik for helping me in the mono-photon analysis.

I would like to thank my classmates Kuntal and Suvankar for making the journey joyful in the SINP CMS group and for many useful discussions. I take this opportunity to sincerely thank my seniors of HENPP division: Sreemoyee di, Mahatsab da, Palash da, Atanu da, Kalyanmoy da, Biswarup da, Souvik da, Swagata di, Dabarati di, Sourav da and Sandhya di who have always supported me during my Ph.D. work. I am thankful to my juniors Arnab, Rajarshi, Biswarup, Arghya, Debabrata, Prasant, Wadut, Jhuma, Pritam and Shubhi for making the working environment stress-less.

I acknowledge the Department of Atomic Energy (DAE), Government of India for providing me with the necessary funding and fellowship to pursue research at SINP.

I am grateful to my sisters-in-law and my nephews for making my stay at home pleasant during the vacations. Their love, care and support helped me to stay happy and positive during my Ph.D. days. Last but foremost, this journey would not have been possible without the unconditional love and support from my parents and my brothers. They have always been on my side in all my decisions.

Contents

Synopsis

The Standard Model (SM) of Particle Physics is a quantum field theoretic model, describing three of the four known fundamental forces of the universe (the electromagnetic, weak, and strong interactions), as well as classifying all known elementary particles. Developed in the early 1970s, it has successfully explained almost all experimental results and precisely predicted a wide variety of phenomena. Discovery of the W and Z boson at CERN was a great experimental evidence of the Standard Model. Over time and through many precision measurements at the Large Electron Position Collider (LEP) at CERN, discovery of top quark and other measurements at Tevatron, Fermilab and many other experiments, the Standard Model has become established as a well-tested theory. Even though the Standard Model is currently the best description there is of the subatomic world, it does not explain the complete picture. The theory incorporates only three out of the four fundamental forces, omitting gravity. There are also other important questions that it does not answer. One such important question is the nature of dark matter (DM). While DM is thought to be the dominant non-baryonic contribution to the matter density of the universe [1], its detection and identification in terrestrial and space-borne experiments remains elusive. At the Large Hadron Collider (LHC), CERN the DM particles may be produced in high-energy proton-proton collisions, if the DM particles interact with the standard model (SM) quarks or gluons via new couplings at the electroweak scale [2, 3]. Although DM particles cannot be directly detected at the LHC, their production could be inferred from an observation of events with

a large transverse momentum imbalance (missing transverse momentum, p_{T}^{miss}).

Another highly important issue is the hierarchy problem, which involves the large energy gap between the electroweak (M_{EW}) and Planck (M_{Pl}) scales [4]. Proposed solutions to this problem include theories with large extra dimensions, such as the model of Arkani-Hamed, Dimopoulos, Dvali (ADD) [5, 6]. The ADD model postulates that there exist n compactified extra dimensions, in which gravitons can propagate freely, and that the true scale of the gravitational interaction in this $4+n$ dimension spacetime (M_D) is of the same order as M_{EW}. The compactification scale R of the additional dimensions is related to the two gravitational scales by $M_{Pl} \sim R^n M_D^{n+2}. For M_D \sim M_{EW}, R >> 1/M_{EW}$ for a wide range of n, leading to a nearcontinuous mass spectrum of KaluzaVKlein graviton states. Although the gravitons would not be observed directly at the LHC, their production would be manifest as events broadly distributed in p_{T}^{miss}.

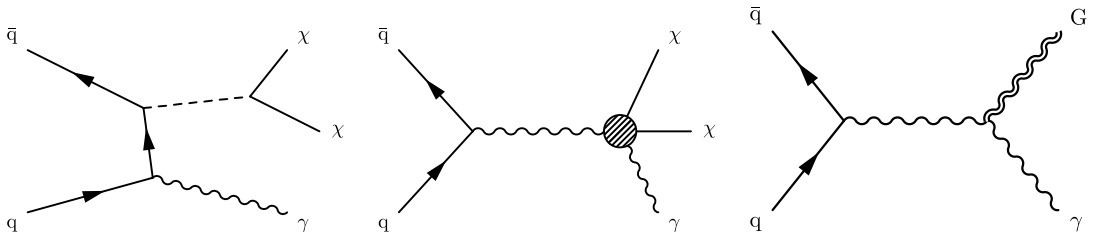

Figure 1: Leading-order diagrams of the simplified DM model (left), electroweak-DM effective interaction (center), and graviton (G) production in the ADD model (right), with a final state of γ and large p_{T}^{miss}.

Events with large missing transverse momentum exist only if there are visible objects recoiling against the invisible particles. Among the many possibilities, a recoiling photon (γ) has the advantage of being identifiable with high efficiency and purity. In DM production through a vector or axial vector mediator, a photon can be radiated from incident quarks (Fig. 1 left). Models of this process have been developed by the CMS-ATLAS Dark Matter Forum [7]. It is also possible that the DM sector couples preferentially to the electroweak sector, leading to an effective interaction

$q\bar{q} \to \gamma \to \gamma\chi\overline{\chi}$ [8], where c is the DM particle (Fig. 1 center). In ADD graviton production, the graviton can couple directly to the photon (Fig. 1 right) or to a quark. In this thesis, I examine final states containing large p_{T}^{miss} in the presence of a photon with large transverse momentum (p_{T}), and search for an excess of events over the SM prediction. Data collected by the CMS detector [9] in 2016 are analyzed. Results are interpreted in the context of these three models.

Events are required to have $p_{\mathrm{T}}^{miss} > 170$ GeV and at least one photon with $p_{\mathrm{T}}^{\gamma} > 175$ GeV in the central region ($|\eta| < 1.44$) of the detector and vetoed with well-identified electrons and muons. Events are rejected if the minimum azimuthal opening angle ($\Delta\phi$) between p_{T}^{miss} and up to four leading jets is less than 0.5 radian. This requirement significantly suppresses the background where jet energy mismeasurement gives rise to large p_{T}^{miss}. Only jets with $p_T > 30$ GeV and $|\eta| < 5$ are considered. The candidate photon and p_{T}^{miss} must also be separated by more than 2 radians. Finally, to reduce the contribution from the $W(\to l\nu) + \gamma$ process, events are also vetoed if they contain an electron or a muon with $p_T > 10$ GeV that is away from the photon by $\Delta R > 0.5$ radian.

The dominant SM backgrounds in this search are the associated productions of a Z or W boson with a high p_{T} photon ($Z(\to \nu\overline{\nu}) + \gamma$ and $W(\to l\nu) + \gamma$). When the Z boson decays into a neutrino-antineutrino pair, the final state exhibits a high p_{T} photon and large missing transverse momentum, which is the exact topology of the search signature. Similarly, if the W boson decays into a lepton-neutrino pair and the lepton is outside of the detector acceptance or is not identified, the event appears to be $\gamma +$ p_{T}^{miss}. Together, the two processes account for approximately 70% of the SM background. These backgrounds are estimated from Monte Carlo (MC) simulation and validated with data. Another control sample dominated by $\mathrm{W}(\to \mu\nu) + \gamma$ production is also studied from MC simulation. SM processes $t\bar{t}\gamma, VV\gamma(V = W, Z), Z(\to l\bar{l}) + \gamma), W \to l\nu$ and $\gamma + jets$ have minor contributions

to the candidate sample. The estimates of all five processes are taken from MC siimulation. Another important background consists of events (primarily $W \to e\nu$) in which the electron is misidentified as a photon. The misidentification occurs due to an inefficiency in seeding electron tracks in the pixel detector. The estimation is measured in data using a tag-and-probe method. Electromagnetic (EM) showers from hadronic activity can also mimic a photon signature. This process is estimated by fitting the shower shape distribution of the photons cluster in the Electromagnetic Calorimeter (ECAL) with template distributions constructing a control sample in data, enriched with multijet events. Finally, backgrounds due to beam halo and ECAL anomalous signals (Spikes) are estimated by fits to distributionss of the cluster seed time.

A total of 400 events are observed in data, which is in agreement with the total expected background of 386 $\pm$ 36 events. Distributions of p_T^{γ} and p_{T}^{miss} for the selected candidate events are shown in Fig. 2 together with respective estimated background distributions.

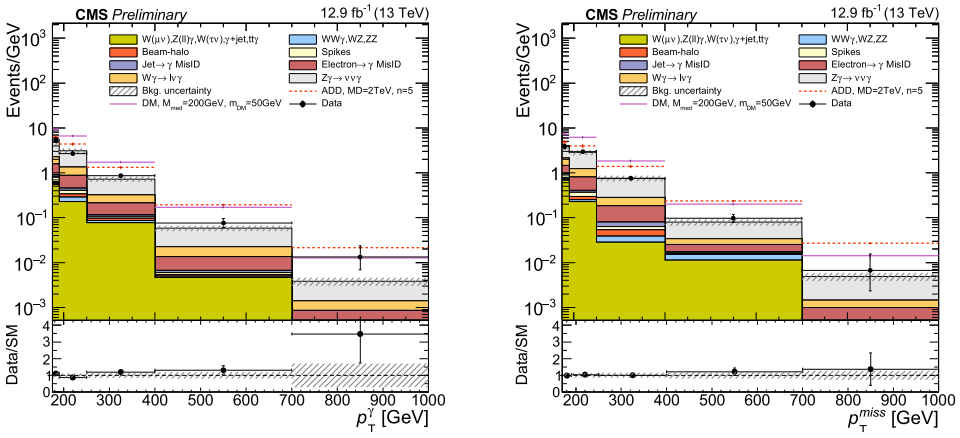

Figure 2: The p_T^{γ} (left) and p_{T}^{miss} (right) distributions for the candidate sample, compared with estimated contributions from SM backgrounds. The background uncertainties include statistical and systematic components. The last bin includes the overflow. The lower panel shows the ratio of data and SM background predictions, where the hatched band shows the systematic uncertainty.

Because no excess with respect to the SM prediction is observed, limits are set on the

considered DM production models and ADD extra dimension scenarios. For each signal model, a 95% confidence level (CL) cross section upper bound is obtained utilizing the asymptotic CL_s prescription [10–12]

The DM simplified models [7] are designed to facilitate the comparison and translation of various DM search results by limiting the degrees of freedom of the DM production interaction. In the models considered in this analysis, Dirac DM particles couple to a vector or axial-vector scalar or pseudoscalar mediator, which in turn has couplings to the SM quarks. Model points are identified by a set of four parameters: the DM mass m_{DM}, the mediator mass M_{med}, the universal mediator coupling to quarks g_q and the mediator coupling to DM g_{DM}. In this analysis vector and axial vector couplings are considered. We fix the values of g_q and g_{DM} to 0.25 and 1, respectively, and scan the M_{med}–m_{DM} plane. Figure 5.16 shows the

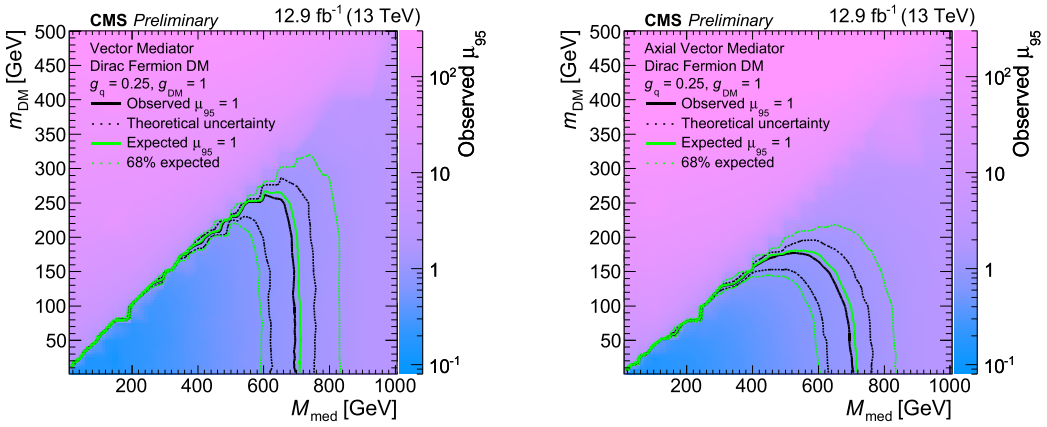

Figure 3: 95% CL upper limits on $\mu = \sigma/\sigma_{Theory}$ in the M_{med}–m_{DM} plane for vector and axial-vector mediator, assuming $g_q = 0.25$ and $g_{DM} = 1$. Expected and observed exclusion contours are overlaid, where mass points to the lower left of the curves are excluded.

cross section upper limits with respect to the corresponding theoretical cross section ($\mu = \sigma^{95\%}/\sigma_{Theory}$) for the vector and axial-vector mediator scenarios on the M_{med}–m_{DM} plane. The solid red and black curves are the expected and observed exclusion contours. The uncertainty on the expected upper limit includes the experimental uncertainties. The uncertainty in the theoretical cross section is translated

to the uncertainty in the observed exclusion contour. For the simplified DM models considered, mediator masses of up to 760 GeV are excluded for small m_{DM} [13].

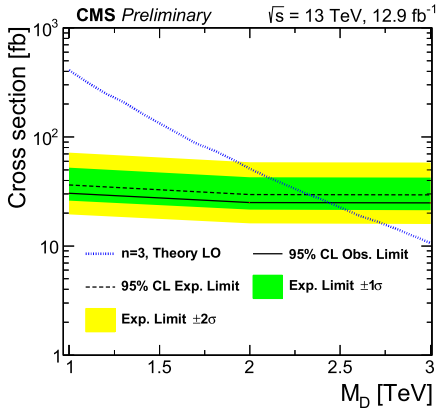

Figure 4: The 95% CL upper limits on the ADD graviton production cross sections as a function of M_D for $n = 3$ [13].

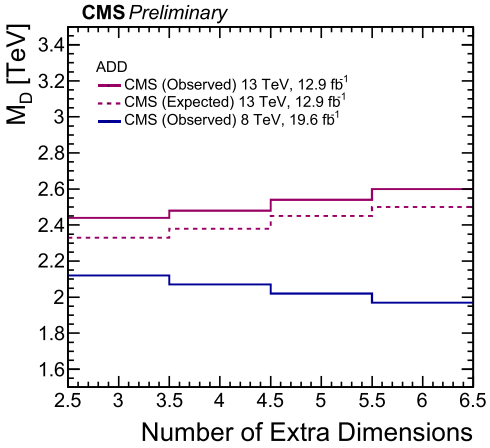

Figure 5: Lower limit on M_D as a function of n [13].

Figure 5.20 shows the upper limit and the theoretical calculation of ADD graviton production cross section for $n = 3$ as a function of M_D. Lower limits on M_D in different number of extra dimensions are compared to CMS Run1 [14] results in Fig. 5. The trends of the two results differ because the graviton production cross section can be increasing or decreasing in n depending on the values of $\sqrt{s}$ and M_D [15]. Values of M_D up to 2.60 TeV for $n = 6$ are excluded [13].

Also a simulation study of energy resolution, position resolution, and π^0-γ separation using multivariate methods of a sampling calorimeter is presented in the thesis. As a realistic example, the geometry of the calorimeter is taken from the design geometry of the Shashlik calorimeter which was considered as a candidate for CMS endcap for the phase II of LHC running. In this design LYSO is used as the sensitive detector. LYSO (cerium doped lutetium yttrium silicate) is a radiation hard, high light yield (about 4 times of BGO), high stopping power (ρ = 7.4 g/cm^3 , X_0 = 1.14 cm and $R_{Moliere}$ = 2.07 cm) and fast response (τ = 40 ns) inorganic scintillator [16, 17].

For absorber, lead and tungsten are taken as two possible choices. For this study, the baseline option uses 4 mm thick lead layers interleaved with 2 mm thick LYSO. The alternative scenario considered uses 2.5 mm thick tungsten with 1.5 mm thick LYSO [18]. The scintillation light is read out using four wavelength shifting fibers going all the way through a Shashlik tower.

The energy resolution is dominated by the sampling fluctuation which contributes to the stochastic term. The constant term is found to be better than 1% while the stochastic term is found to be $10.3\%/\sqrt{E}$ for light yield value of 4000 p.e./MeV. The energy resolution is found to be similar for lead/LYSO and tungsten/LYSO configurations and the optimum number of layers is found to be 28 which corresponds to ~25 radiation lengths deep detector. For 125 GeV Higgs boson decaying to a pair of photons, this detector will achieve a mass resolution of 0.64 GeV when both the photons are detected in the Shashlik detector.

The position resolution using information of the Shashlik detector alone is 2.0 mm for photons of 100 GeV. The resolution improves with energy of the photon and a better resolution is obtained when the center of gravity method uses logarithmic weighting (to 0.34 mm) or a correction is made for the S-shape (to 0.22 mm).

A study of the $\pi^0 - \gamma$ separation presented in the thesis shows that the fine grain information of the shower profile collected by individual fibers is useful for separation

between π^0 and γ at high energies. With the MVA technique a background rejection efficiency of 90% with signal efficiency 90% was achieved, which is approximately three times better than the best background rejection that could be achieved by cut-based methods. A method of virtual slicing of the hit tower and impact point based training of the network is presented, which gives an additional improvement of 8-10%. The conclusion drawn from this study is that the $\pi^0 - \gamma$ separation power of the Shashlik calorimeter can be improved significantly by emplyoying an MVA based method with fine grain information as input and impact point based training. In this study a Shashlik detector of a specific dimension and material is considered. However the methodology described in this thesis for the resolution studies as well as the techniques employed for distinguishing between the spatial patterns of energy deposits by a photon and a π^0, can be easily adapted to any sampling calorimeter.

References

1. R. Gaitskell, "Direct detection of dark matter," *Annual Review of Nuclear and Particle Science*, vol. 54, 2004.

2. P. J. Fox, R. Harnik, J. Kopp, and Y. Tsai, "Missing energy signatures of dark matter at the lhc," *Phys. Rev. D*, vol. 85, p. 056011, Mar 2012. [Online]. Available: https://link.aps.org/doi/10.1103/PhysRevD.85.056011

3. J. Goodman, M. Ibe, A. Rajaraman, W. Shepherd, T. M. Tait *et al.*, "Constraints on Dark Matter from Colliders," *Phys.Rev.*, vol. D82, p. 116010, 2010.

4. L. Susskind, "Dynamics of spontaneous symmetry breaking in the weinberg-salam theory," *Phys. Rev. D*, vol. 20, pp. 2619–2625, Nov 1979. [Online]. Available: https://link.aps.org/doi/10.1103/PhysRevD.20.2619

5. N. Arkani-Hamed, S. Dimopoulos, and G. Dvali, "The Hierarchy problem and new dimensions at a millimeter," *Phys. Lett. B*, vol. 429, p. 263, 1998.

6. N. Arkani Hamed, S. Dimopoulos, and G. Dvali, "Phenomenology, astrophysics, and cosmology of theories with submillimeter dimensions and tev scale quantum gravity," *Phys. Rev. D*, vol. 59, p. 086004, Mar 1999. [Online]. Available: https://link.aps.org/doi/10.1103/PhysRevD.59.086004

7. D. Abercrombie *et al.*, "Dark Matter Benchmark Models for Early LHC Run-2 Searches: Report of the ATLAS/CMS Dark Matter Forum," 2015.

8. A. Nelson, L. M. Carpenter, R. Cotta, A. Johnstone, and D. Whiteson, "Confronting the Fermi Line with LHC data: an Effective Theory of Dark Matter Interaction with Photons," *Phys. Rev.*, vol. D89, no. 5, p. 056011, 2014.

9. S. Chatrchyan *et al.*, "The CMS experiment at the CERN LHC," *JINST*, vol. 3, p. S08004, 2008.

10. ATLAS and CMS Collaborations, The LHC Higgs Combination Group, "Procedure for the LHC Higgs boson search combination in Summer 2011," CERN, Geneva, Tech. Rep. CMS-NOTE-2011-005. ATL-PHYS-PUB-2011-11, Aug 2011.

11. T. Junk, "Confidence level computation for combining searches with small statistics," *Nucl. Instrum. Meth.*, vol. A434, pp. 435–443, 1999.

12. A. L. Read, "Presentation of search results: The CL(s) technique," *J. Phys.*, vol. G28, pp. 2693–2704, 2002, [,11(2002)].

13. A. M. Sirunyan *et al.*, "Search for new physics in the monophoton final state in proton-proton collisions at sqrt(s) = 13 TeV," 2017.

14. V. Khachatryan *et al.*, "Search for new phenomena in monophoton final states in proton-proton collisions at $\sqrt{s} = 8$ TeV," *Phys. Lett.*, vol. B755, pp.

102–124, 2016.

15. G. F. Giudice, R. Rattazzi, and J. D. Wells, "Quantum gravity and extra dimensions at high-energy colliders," *Nucl. Phys.*, vol. B544, pp. 3–38, 1999.

16. D. W. Cooke, K. J. McClellan, B. Bennett, J. M. Roper, M. Whittaker, R. Muenchausen, and R. C. Sze, "Crystal growth and optical characterization of cerium-doped lu1.8y0.2sio5," vol. 88, pp. 7360 – 7362, 2000.

17. T. Kimble, M. Chou, and B. H. T. Chai, "Scintillation properties of lyso crystals," in *2002 IEEE Nuclear Science Symposium Conference Record*, vol. 3, Nov 2002, pp. 1434–1437 vol.3.

18. R.-Y. Zhu, "Private communication, Talk given at Geneva, Switzerland," 2012.

CHAPTER 1

Introduction

The Standard Model (SM) of Particle Physics is a quantum field theoretic model, describing three of the four known fundamental forces of the universe (the electromagnetic, weak, and strong interactions), as well as classifying all known elementary particles. Developed in the early 1970s, it has successfully explained almost all experimental results and precisely predicted a wide variety of phenomena. Discoveries of the W and Z boson at the European Organization for Nuclear Research (CERN), and of gluon at the Deutsche Elektron Synchrotron, (DESY) were great experimental evidences of the Standard Model. Over time and through many precision measurements at the Large Electron-Position Collider (LEP) at CERN [1], discovery of top quark and other measurements at Tevatron, Fermilab and many other experiments, the Standard Model has become established as a well-tested theory. With the discovery of Higgs boson at the Large Hadron Collider (LHC) at CERN, in Geneva in 2012, the Standard Model is now a fully experimentally verified theory. Even though the Standard Model is currently the best description of the subatomic world, it does not provide the complete picture of particle interactions at high energies. The hierarchy problem - that is the orders of magnitude difference between the Plank mass and electroweak symmetry breaking scale, the nature of dark matter, existence of multiple families of leptons and quarks, non zero mass of neutrinos are

facts of Nature unexplained by the Standard Model.

One particular case of phenomena beyond the Standard Model is the existence of dark matter (DM). Dark matter is thought to be the dominant non-baryonic contribution to the matter density of the universe, its detection and identification in terrestrial and space borne experiments remains elusive. At the Large Hadron Collider, CERN, the dark matter particles may be produced in high-energy proton-proton collisions, if the dark matter particles interact with the Standard Model quarks or gluons via new couplings at the electroweak scale. Although dark matter particles cannot be directly detected at the LHC, their production could be inferred from an observation of events with a large transverse momentum imbalance (missing transverse momentum, p_{T}^{miss}).

Another highly important issue is the hierarchy problem, which involves the large energy gap between the electroweak ($M_{\mathrm{EW}} \sim 10^3$GeV) and Planck ($M_{\mathrm{P}} \sim 10^{19}$GeV) scales [2]. Proposed solutions to this problem include theories with spatial extra dimensions, such as the model of Arkani-Hamed, Dimopoulos, Dvali (ADD). The ADD model postulates that there exist n compactified extra dimensions, which would have large (sub mm scale) compactification radius. Gravitons can propagate freely in the compactified extra dimensions and the true scale of the gravitational interaction in this $4+n$ dimension space time (M_D) is of the same order as M_{EW}. The compactification scale R of the additional dimensions is related to the two gravitational scales by $M_P \sim R^n M_D^{n+2}$. For $M_D \sim M_{EW}, R >> 1/M_{EW}$ for a wide range of n, leading to a near continuous mass spectrum of Kaluza-Klein graviton states. Although the gravitons would not be observed directly at the LHC, their production would be manifested as events broadly distributed in p_{T}^{miss}.

In this thesis, I examine mono photon channel, containing large missing transverse momentum (p_{T}^{miss}) in the presence of a photon with large transverse momentum, and search for an excess of events over the SM prediction. This analysis uses data

collected from the Compact Muon Solenoid detector at the Large Hadron Collider. This thesis is structured as follows. Chapter 2 gives a brief overview of the physical theories which are relevant for the following analyses, Standard Model as well as Beyond the Standard Model (BSM) theories. The layouts of the Large Hadron Collider and the Compact Muon Solenoid detector are described in chapter 3, and the reconstruction of collision events and physics objects are summarized in Chapter 4. Chapter 5 contains the details of the analysis performed with the 13 TeV, 2016 data. The last chapter of this thesis describes the simulation study performed for the upgrade project of the CMS endcap calorimeter.

CHAPTER 2

Theoretical Motivation

The idea that all matter is composed of elementary particles, came around 5th century BC when the Greek philosopher Democritus postulated that all matter was made up of *atomos*. Later the word *atom* is derived from the Greek word *atomos*, meaning indivisible and until the end of 19th century, atoms were thought to be fundamental building blocks of all form of matter. The modern era of particle physics began with the discovery of the first subatomic particle, the electron in 1897 by J.J. Thomson. Since then, there has been an explosion in the discovery of new sub-atomic particles by experimental physicists and theoretical physicists have been busy explaining the nature of these new particles and their interactions.

In the 1930s it was perceived that the atom as being composed of particles of three kinds: electrons, protons and neutrons. In the 1960s and 1970s a theory emerged that described all of the known elementary particle interactions, except gravity. (Gravity is too much weak to play any significant role in ordinary particle processes.) This theory or more accurately, this collection of related theories, based on two families of elementary particles (quarks and leptons), and incorporating quantum electrodynamics (QED), the Glashow-Weinberg-Salam theory of electroweak processes,and quantum chromodynamics (QCD) - has come to be known as the

Standard Model of prticle physics. This chapter contains a brief overview of the three forces incorporated into the Standard Model of particle physics (SM), why we search for physics beyond the Standard Model (BSM), what motivates searches for dark matter (DM), extra spatial dimensions, and proposed models of those. The explanation of Standard Model largely taken from the standard texts on the subject [3–6].

2.1 The Standard Model

The standard Model (SM) of elementary particle physics is a relativistic quantum field theory described by a $SU(3)_C \otimes SU(2)_L \otimes U(1)_Y$ gauge theory to relate the fundamental interactions of elementary and composite particles. The standard model is described by, quantum chromodynamics, the theory of strong interactions, and the electroweak model, which provides the theory of weak and electromagnetic interactions. Many experimental verifications obtained until now have consistently supported the Standard Model with very high precision. According to the SM, all matter is made out of elementary particles called fermions and the forces between fermions are manifested as an exchange of bosons.

Fermions can be organized into two elementary categories: quarks that take part in strong interaction and leptons that do not have strong interaction. Quarks and leptons are spin 1/2 point-like particles that have no substructure; they are defined by their mass and quantum numbers described in Tables 2.1,2.3.

Each force in the Standard Model is mediated by the exchange of the spin 1 bosons listed in Table 2.2. Gluons are mediators of strong force, $W^{\pm}$ and Z bosons mediate the weak force, and photons mediate the electromagnetic force. Fermions can interact via these forces if their internal quantum numbers transform under the symmetries of the theory. The interactions between all the particles described by the

	leptons	mass(MeV/c^2)	charge(e)	spin number
First generation	electron (e)	0.51	-1	1/2
	electron neutrino (ν_e)	$< 2 \times 10^{-6}$	0	1/2
Second generation	muon (μ)	105.7	-1	1/2
	muon neutrino (ν_μ)	< 0.19	0	1/2
Third generation	tau (τ)	1776.9	-1	1/2
	tau neutrino (ν_τ)	< 18.2	0	1/2

Table 2.1: Standard model particles: Lepton classification [7]

	quarks	mass(MeV/c^2)	charge(e)	spin number
First generation	up quark (u)	2.2	+2/3	1/2
	down quark (d)	4.7	-1/3	1/2
Second generation	charm quark (c)	1,270	+2/3	1/2
	strange quark (s)	96	-1/3	1/2
Third generation	top (t)	172,000	+2/3	1/2
	bottom (b)	4,180	-1/3	1/2

Table 2.2: Standard model particles: Quark classification [7]

gauge bosons	charge(e)	mass(GeV/c^2)	spin number
gluon (g)	0	0	1
photon (γ)	0	0	1
W boson ($W^\pm$)	± 1	80.4	1
Z boson (Z^0)	0	91.2	1
graviton (hypothetical)	0	0	2

Table 2.3: Standard model particles: Gauge Bosons [7]

Standard Model are summarized by the diagrams in Figure 2.1. The three theories comprising the Standard Model are constructed as gauge theories, which is discussed in the next section.

2.1.1 Gauge Theory

The different components of the Standard Model (electroweak dynamics and quantum chromodynamics) each start as a basic theory to model the interactions of

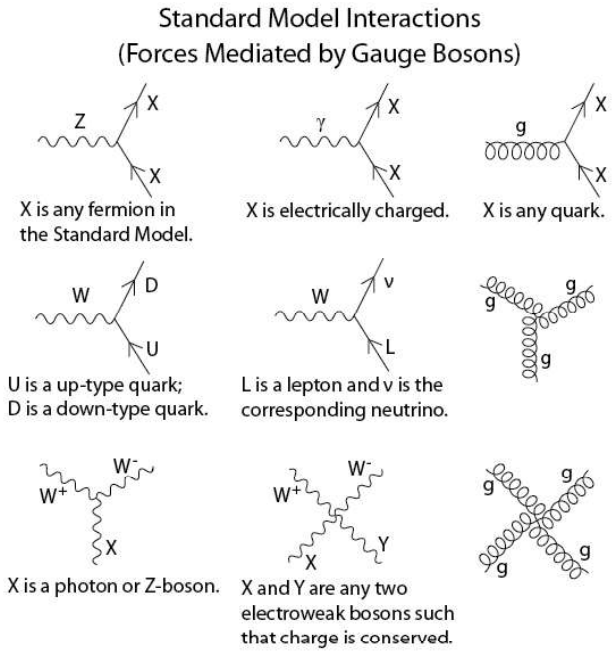

Figure 2.1: A list of the vertices that appear in Standard Model Feynman Diagrams. Higgs Boson interactions and neutrino oscillations are omitted. Feynman rule values of the vertices are also omitted [8].

fermions with a Dirac Lagrangian:

$$\mathcal{L} = \bar{\psi}(i\gamma^{\mu}\partial_{\mu} - m)\psi \tag{2.1}$$

where ψ are space-time dependent fields representing the particles, γ^{μ} are the gamma matrices, and m is the mass of the particles. In each case, the fields of the theory transform under a particular symmetry group. These symmetry groups are chosen to explain the experimentally observed constraints of the particle interactions represented through the internal quantum numbers. The fields are then modified to reflect the local position in space and time and establish invariance under local transformations. The Lagrangian is also tuned, according to the gauge symmetry group, to be locally gauge invariant by introducing the gauge fields. The gauge fields represent the gauge bosons via the covariant derivative, D_{μ}, which replaces the partial derivative, ∂_{μ}.

2.1.2 Quantum Electrodynamics

Electromagnetic interactions are formulated by a gauge theory with the symmetry group U(1), which transforms as

$$\psi \rightarrow \psi' = e^{-i\theta}\psi \tag{2.2}$$

where θ is a constant phase term. To make the global symmetry of the U(1) group local, the constant phase transformation is replaced by a space-time dependent phase ($\theta \rightarrow \theta(x)$) and an additional vector field is introduced to the Lagrangian via the covariant derivative,

$$D_\mu \equiv \partial_\mu - ieA_\mu(x) \tag{2.3}$$

where A_μ is a spin 1 vector field and e is the electromagnetic charge of the fermion described by the field. The field A_μ introduces the photon as the gauge boson that mediates the electromagnetic force between charged particles. In order to account for the kinetic energy of A_μ, we add the well-known gauge-invariant term $\frac{1}{4}F_{\mu\nu}F^{\mu\nu}$ to the Lagrangian, where the field strength tensor is defined as $F_{\mu\nu} = \partial_\mu A_\nu - \partial_\nu A_\mu$. The complete Lagrangian for the electromagnetic interactions between a charged particle and a photon is:

$$\mathcal{L} = \bar{\psi}(x)(i\gamma^\mu D_\mu - m)\psi(x) - \frac{1}{4}F_{\mu\nu}F^{\mu\nu} \tag{2.4}$$

This theory is called quantum electrodynamics (QED).

2.1.3 Quantum Chromodynamics

The theory describing the strong force between quarks and gluons, called quantum chromodynamics (QCD), is built in a similar way. Evidence for quarks were

first observed in $e-p$ scattering events at SLAC [9, 10]. The fields describing the quarks are composed of members of the SU(3) symmetry group to account for experimental evidence indicating that an additional internal characteristic generates three distinguishable states of quarks that have otherwise identical properties. This new quantum number, color, and its conservation requirements provide an explanation as to why observed baryons like $\Delta^{++}(uuu)$ don't violate the Pauli Exclusion principle [11], and why quarks are observed in pairs and triplets as color-anticolor mesons and triple color baryons, respectively. Branching ratio studies performed on e^+e^- collisions at SLAC [9, 10] indicate that this characteristic, named "color", comes in three variations, denoted as red, green, and blue. The resulting fields that describe quarks in terms of their color charge are written as $q = (q^R; q^G; q^B)$, and the mediating gauge boson, the gluon, appears in the Lagrangian as eight distinct color-anticolor vector fields. To create a locally gauge invariant Lagrangian, the partial derivative is again replaced by a covariant derivative which includes the eight vector boson fields of the gluons, A^i_μ, a term g_s related to the strong coupling constant, and the 3×3 Gell-Man matrices, λ^i [3, 12].

$$\partial_\mu \rightarrow D_\mu \equiv \partial_\mu - ig_s \frac{\lambda^i}{2} A^i_\mu \tag{2.5}$$

The magnitude of the force between color-charged particles, which is very small at short distances but increases asymptotically at larger distances, is reflected in the coupling constant $\alpha_s = g_s^2/4\pi$ and the non-Abelian construction of the gauge theory. By expressing a function for a QCD-predicted cross section in terms of a beta function, we find the relationship

$$\frac{1}{\alpha_s} \propto \log(Q/\Lambda) \tag{2.6}$$

relating α_s to Q, where Q is the momentum involved in the interaction, and Λ is the momentum scale, also known as the QCD scale and can be thought of as

the energy boundary between quasi-free quarks and gluons and the bound states of hadrons. From this relationship we can see that α_s becomes strong as Q^2 is decreased at a scale set by Λ. Strong interactions become asymptotically strong at distances $\sim 1/\Lambda$, which roughly correspond to the diameter of light hadrons [4]. The energy required to separate the quarks beyond that distance is greater than the pair production energy; rather than pull two quarks further apart, a new quark and antiquark are produced which form mesons with the originally separated quarks. This phenomenon is referred to as quark confinement.

2.1.4 Electroweak Theory

The Glashow-Weinberg-Salam electroweak gauge theory [13] is the first successful model that unifies two fundamental forces of nature: the electromagnetic and the weak force. The electromagnetic force is described earlier in this chapter, and the weak force describes flavor-changing processes in which heavy fermions decay into lighter ones, initially observed in β decay in nuclei: $n \to p + e^- + \bar{\nu}_e$, which take place among left-handed fermions. Both types of interactions are explained through transformations under the $\mathrm{SU}(2)_L \otimes \mathrm{U}(1)_Y$ symmetry group. Only left-handed particles carry the weak isospin quantum number, I_w, which allows for transformations under the $\mathrm{SU}(2)_L$ symmetry group, while both left- and right-handed particles carry weak hypercharge spin (Y), which transforms under $\mathrm{U}(1)_Y$ symmetry. As an example, if we consider the first generation of leptons, the electron and electron neutrino, the left-handed field components form a doublet while the right-handed field exists as a singlet:

$$\psi_L = \begin{pmatrix} \nu_e \\ e^- \end{pmatrix}_L \quad ; \quad \psi_R = e_R^- \tag{2.7}$$

which transform under both $\mathrm{SU}(2)_L$ and $\mathrm{U}(1)_Y$. In order to make the Lagrangian locally gauge invariant, the covariant derivative introduces four gauge bosons fields,

$\vec{W}_\mu$ and B_μ, associated with the $\mathrm{SU}(2)_L$ and $\mathrm{U}(1)_Y$ symmetry groups, respectively:

$$D_\mu = \partial_\mu - ig\frac{\vec{\tau}}{2}.\vec{W}_\mu - ig'\frac{Y}{2}B_\mu \tag{2.8}$$

as well as gauge coupling constants g and g' for $\mathrm{SU}(2)_L$ and $\mathrm{U}(1)_Y$, respectively, $\vec{\tau}$ as a vector of $\mathrm{SU}(2)_L$ generator matrices, and the weak hypercharge quantum number Y. Four kinetic energy terms are added to the Lagrangian for the four gauge fields, at which point the physical gauge boson fields can be written as linear combinations of the $\vec{W}$ and B fields:

$$\begin{aligned} W_\mu^\pm &= (W_\mu^1 \mp iW_\mu^2)/\sqrt{2} \\ Z_\mu &= W_\mu^3 \cos\theta_W - B_\mu \sin\theta_W \\ A_\mu &= W_\mu^3 \sin\theta_W + B_\mu \cos\theta_W \end{aligned} \tag{2.9}$$

where θ_W is known as the weak mixing angle, or the Weinberg angle, which relates the coupling constants g and g' in the following way:

$$\sin\theta_W = \frac{g'}{\sqrt{g^2+g'^2}} \quad ; \quad \cos\theta_W = \frac{g}{\sqrt{g^2+g'^2}} \tag{2.10}$$

and the weak mixing angle is a free parameter of the Standard Model and $\sin^2\theta_W$ has been measured to $\sin^2\theta_W = 0.22336$ [7]. Moreover, the weak mixing angle relates the masses of the heavy gauge bosons, and the coupling constants g and g' to the more familiar electromagnetic charge as:

$$\cos\theta_W = \frac{m_W}{m_Z} \tag{2.11}$$

$$e = g'\cos\theta_W = g\sin\theta_W \tag{2.12}$$

The mass terms for $\mathrm{W}^\pm$ and Z do not automatically come out of the $\mathrm{SU}(2)_L \otimes \mathrm{U}(1)_Y$ theory, though adding mass terms for the $\mathrm{W}^\pm$ and Z bosons would violate local gauge

invariance. However, in order for the weak mediators to act at short distances and couple weakly to fermions, the bosons need mass. Introducing mass terms and constructing the four gauge bosons as they appear in 2.9 is accomplished through the Higgs mechanism, whereby scalar fields are added to the Lagrangian that cause a spontaneous symmetry breaking, producing mass terms for the weak force while maintaining local gauge invariance. Two complex scalar fields forming an $SU(2)_L$ doublet, ϕ, are added to the theory, which introduces a potential term. The gauge invariant potential term is given by:

$$V(\phi^\dagger, \phi) = m^2\phi^\dagger\phi + \lambda(\phi^\dagger\phi)^2 \tag{2.13}$$

where m^2 and λ are real constants. If we assume the Nambu-Goldstone case that the physical vacuum is not unique, $m^2 < 0$ and $\lambda > 0$ and the potential will have two minima, $\pm\sqrt{\frac{-\mu^2}{2\lambda}} = \pm\frac{v}{\sqrt{2}}$. Choosing one of these points as the actual physical vacuum, or the vacuum expectation value (VEV), breaks the $SU(2)_L \otimes U(1)_Y$ symmetry of the Lagrangian. Since particle excitations are calculated as fluctuations about the vacuum state, the scalar doublet is redefined in terms of the VEV and excitations. Following the Goldstone theorem, each spontaneously broken symmetry of the scalar doublet due to the existence of the VEV corresponds to a massless field in the doublet. The resulting three massless fields, called Goldstone bosons, are absorbed into the theory as the longitudinal components of the $W^\pm$ and Z gauge bosons, generating mass terms for the weakly interacting bosons and fermions and a relationship between the $W^\pm$ and Z masses. The remaining real scalar field is the Higgs boson.

2.2 Beyond the Standard Model

A large range of Beyond the Standard Model (BSM) theories exist, which try to explain the open questions and issues of the Standard Model. In the analysis part of this thesis, a search with $\gamma+$ missing transverse momentum (p_{T}^{miss}) final states, which is a signature of new physics, is performed. The theories discussed in this section, are theories that predict such a signature.

2.2.1 Dark Matter

2.2.1.1 Observational Evidence

Several astronomical observations support the widely accepted conclusion that dark matter makes up $\sim 25\%$ of the mass-energy content in the universe [14]. Observations have firmly established that galaxies are primarily composed of dark matter. The strongest arguments come from studies of the rotational curves of spiral galaxies. Spiral galaxies are characterized by a central bulge and a disk of stars rotating together around an axis. A 'rotational curve' relates the disk velocity of a galaxy, calculated from observations of the redshifts of emission lines from the stars and clouds in the galaxy, in terms of the radius of the galaxy. The speed of arm $v(r)$ at a radius r from the centre of the galaxy is shown in Figure 2.2. This is the rotational curve of a galaxy. The brightness of a disk decreases exponentially with its radius and, if the mass profile matched the intensity profile, the velocities of the material in the galaxy should also decrease along the radius. However, Vera Rubin et al. showed in the late 1960s that the rotational curves remained flat between 1 and 2 optical radii from the center, corresponding to a distance of 10-20 kpc [15]. The mass of the galaxy could be calculated from the rotation curve by relating the gravitational and centripetal accelerations in terms of the observed rotation curve

$v(r)$ and the mass $M(r)$ contained in a sphere of radius r:

$$\frac{v^2(r)}{r} = G\frac{M(r)}{r^2} \tag{2.14}$$

The constant rotational curves lead to a mass distribution directly proportional to r, which then requires a significant dark-matter component to balance the exponentially falling luminous mass distribution in the galaxies. A study of rotation curves for a larger sample of galaxies by Persic, Salucci, and Stel [16] demonstrated the same flatness of the rotational curves, indicating a dark matter mass distribution present in the galaxies. An example rotational curve for the spiral galaxy NGC6503 is shown in Figure 2.2

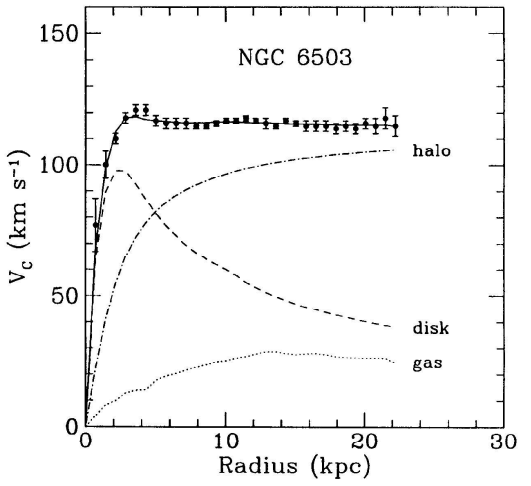

Figure 2.2: Rotational velocity as function of radius from the galactic center, for the NGC 6503 galaxy. The dashed, dotted and dot-dashed lines represent the expected contributions from the luminous disk, the gas content of the galaxy and the dark matter halo respectively. The full line is the combination of these three, which matches the observed data very well [17].

Dark matter can be also studied by its gravitational effects on galaxy clusters. The virial theorem, which relates the kinetic and gravitational potential energies, can be applied to a cluster of galaxies to find a relationship between the mass, radius, and velocity dispersion of the cluster. The calculated masses can then be combined with

measurements of the optical luminosity of the galaxies in the cluster to calculate the mass-to-light ratios. Fritz Zwicky applied this approach in 1933 to measurements of the Coma cluster of galaxies [18], and Girardi et al. did the same in 2000 to a sample of about 100 clusters using multiple surveys [19,20]; both studies indicated that there was several hundreds of times more matter present than what was observable via electromagnetic radiation.

Measurements of weak gravitational lensing have also been used to study dark matter in galaxy clusters. In weak lensing, the light from background galaxies is gravitationally deflected; the ellipticity of background galaxies warp to line up tangent to circles around mass concentrations and their magnitudes are slightly modified. These changes relate linearly to the gravitational potential of the lensing cluster and can be used to map the matter density of the lensing clusters. The most famous example of evidence of dark matter from gravitational lensing comes from the Bullet Cluster. The Bullet Cluster was formed from the collision of a large cluster with a smaller one and is named for a bullet-shaped cloud of gas observed in the X-ray spectrum which contains the majority of the baryonic component. Gravitational lensing maps show that while the X-ray emitting material is mostly located in the central bullet-shaped area of the cluster, the majority of the gravitationally interacting has moved further apart, past the collision vertex of the two clusters. This separation can be explained by postulating that the DM 'passed through' baryonic matter without any significant interactions [21].

2.2.1.2 Experimental Searches for Dark Matter

There are three types of dark matter searches: direct, indirect, and Collider. Direct searches for a DM candidate χ, look for evidence of elastic χ-nucleon scattering in detectors that are usually placed deep underground to reduce background interactions. Indirect searches watch the cosmos for photons or neutrinos produced in $\chi\bar{\chi}$

annihilations. Collider searches take place at colliders like the LHC, where dark matter $\chi\bar{\chi}$ pairs may be produced in high energy collisions. As it was mentioned earlier, studies of the $\gamma + p_{\mathrm{T}}^{miss}$ channel would be sensitive to new physics like dark matter production at the LHC. The DM could be produced in the reaction $q\bar{q} \to \chi\bar{\chi}\gamma$, where the photon is radiated by one of the incoming quarks, which would look like an excess of $Z(\nu\bar{\nu})\gamma$ or $\gamma + p_{\mathrm{T}}^{miss}$ events.

The results of the analysis described in this thesis are interpreted in terms of recent theoretical work [22–26] that suggests that DM-and-SM particle interactions involve heavy ($\geq$ few TeV) mediating particles. The interactions can be described for a range of phenomenologically distinct cases in the framework of an effective field theory (EFT) with the following operators:

$$\mathcal{O}_V = \frac{(\bar{\chi}\gamma_\mu\chi)(\bar{q}\gamma^\mu q)}{\Lambda^2} \qquad \text{vector, s-channel} \tag{2.15}$$

$$\mathcal{O}_A = \frac{(\bar{\chi}\gamma_\mu\gamma_5\chi)(\bar{q}\gamma^\mu\gamma_5 q)}{\Lambda^2} \qquad \text{axial vector, s-channel} \tag{2.16}$$

$$\mathcal{O}_t = \frac{(\bar{\chi}P_R q)(\bar{q}P_L\chi)}{\Lambda^2} + (L \leftrightarrow R) \qquad \text{scalar, t-channel} \tag{2.17}$$

$$\mathcal{O}_g = \alpha_s\frac{(\bar{\chi}\chi)(G^a_{\mu\nu}G^{a\mu\nu})}{\Lambda^3} \qquad \text{scalar, s-channel} \tag{2.18}$$

where χ is the dark matter field, q is a Standard Model quark field, $G^a_{\mu\nu}$ is the gluon field strength tensor, and $P_{R(L)} = (1 \pm \gamma_5)/2$. The contact interaction scale Λ (measures the strength of the interaction) is given by $M/\sqrt{g_\chi g_q}$, where M is the mass of the mediator, g_χ is its coupling to dark matter and g_q is its coupling to Standard Model quarks. These effective operators are built with the assumption that χ is a Dirac fermion, but if χ was a Majorana fermion the vector operators would disappear but the theory would otherwise remain the same.

Most direct detection searches and collider searches alike bank on the idea that dark matter must couple to quarks and gluons. The gluon operator predicted by these studies is not expected to generate monophoton events with any measurable

significance, but χ-nucleon scattering is modeled through the t-channel with an operator similar to equation 2.17, but in terms of nucleons instead of quarks. Collider searches at colliders, rely on dark matter pair-production, modeled in this case through the s-channel operators shown in equation 2.15 and 2.16. In order to exchange the quark operators for nucleon operators, the SM and DM fields in the coupling terms must be written separately. This is already the case for $\mathcal{O}_V$, $\mathcal{O}_A$ and $\mathcal{O}_t$ can be converted through a Fierz transformation [23] to a sum of other operators:

$$\frac{1}{\Lambda^2}(\bar{\chi}P_R q)(\bar{q}P_L\chi) + (L \leftrightarrow R) = \frac{1}{\Lambda^2}(\mathcal{O}_V - \mathcal{O}_A) \tag{2.19}$$

effectively connecting the t-channel χ-nucleon scattering to the s-channel pair-production mechanisms. Thus, we can express the results of collider search and direct detection studies in terms of vector operators, which induce spin-independent (SI) scattering, and axial-vector operators which induce spin-dependent (SD) scattering, in a clearly comparable way. If χ is a Dirac fermion, both SI and SD interactions will contribute to $\chi\bar{\chi}$ production at colliders, while the SI interaction will dominate over the SD contribution in direct detection experiments, making this comparison additionally helpful. At the nucleon level, the coupling terms $\mathcal{O}_V$ and $\mathcal{O}_A$ look the same except the quark fields q are replaced by nucleon field terms N and translational coefficients.

DM collider searches have some advantages over direct and indirect searches. Unlike direct and indirect searches, collider studies dont have to take into account any astrophysical uncertainties regarding the abundance and velocity distribution of DM. Another strength is that if DM couples through a vector to second- and third-generation quarks, it will be seen from at a collider experiment; this phenomenon would never be seen through direct or indirect detection. However, colliders are at a disadvantage for cases with a light mediator. The cross section for DM production

with a photon or jet can be approximated by

$$\sigma(pp \to \bar{\chi}\chi + X) \sim \frac{g_q^2 g_\chi^2}{(q^2 - M^2)^2 + \Gamma^2/4} E^2 \tag{2.20}$$

where E is the center-of-mass energy of the parton, M is the mass of the mediator, q is the four-momentum flowing through the mediator, and Γ is the mediator width. The cross section for direct detection phenomena is approximately

$$\sigma(\chi N \to \chi N) \sim \frac{g_q^2 g_\chi^2}{M^4} \mu_{\chi N}^2 \tag{2.21}$$

with the reduced mass $\mu_{\chi N}$ of the dark matter and the target nucleus.

For the collider experiments, the limit that colliders can set on the coupling constants, $g_q^2 g_\chi^2$, become independent of the mass when $M^2 \ll q^2$; this means that for smaller M values, the limits on the coupling constants become stronger in direct detection studies while they get weaker in collider studies. The details of each case depend largely on the applied model and the relationship between the mediator mass and the χ-nucleon mass but, in general, for light mediators with mass $M \lesssim 100$ GeV, the limitations that collider studies can place on direct detection cross sections are weaker than what is possible in models with greater mediator masses.

The EFT describes the case when production of DM takes place through a contact interaction and the mediator of the interaction between SM and DM particles are very heavy; if this is not the case, then models that explicitly include these mediators are needed. A set of DM simplified models as proposed by the CMS-ATLAS Dark matter forum [26] is considered for extracting the limits in the analysis described in the chapter 5. In this simplified model it is assumed that a DM particle χ of mass m_χ is a Dirac fermion and the production of DM takes place via the exchange of a spin-1 mediator of mass M_{med} in the s-channel, illustrated in Figure 2.3. In this case, the interaction is described by four parameters: the DM mass m_{DM}, the

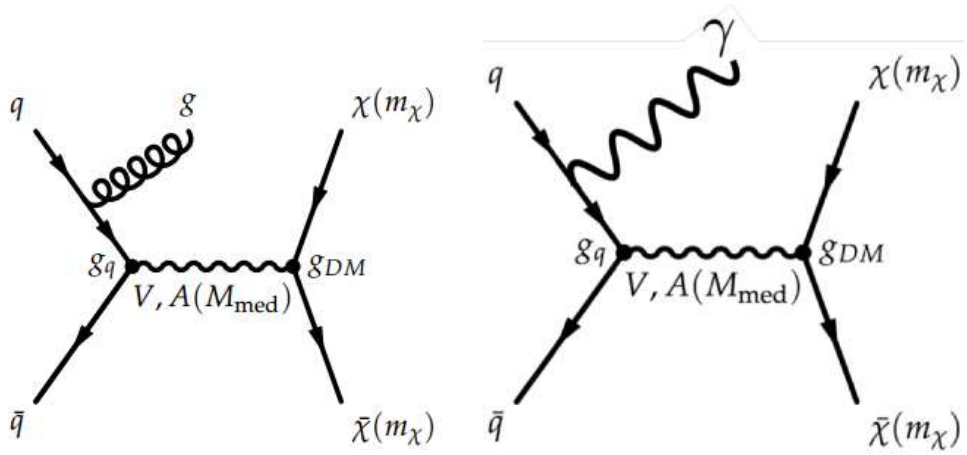

cc

Figure 2.3: Feynman diagrams showing the pair production of Dark Matter particles in association with a gluon (left diagram) or a photon (right diagram) from the initial state via a vector or axial-vector mediator. The cross section and kinematics depend upon the mediator and Dark Matter masses, and the mediator couplings to Dark Matter and quarks respectively: $(M_{med}, m_\chi, g_\chi, g_q)$. [26]

mediator mass M_{med}, the universal mediator coupling to quarks g_q and the mediator coupling to DM g_{DM}. In the limit of large M_{med}, the simplified model converge to a universal set of operators in an effective field theory [22, 24, 25].

In the framework of this theory, the results of a simple counting experiment at the LHC can be used to set limits on a variety of DM couplings that translate into constraints on the $\chi\bar{\chi}$ annihilation cross section as well as the χ-nucleon cross section measured in direct detection experiments. The search for a DM candidate is well motivated by several studies indicating a large amount of non-baryonic matter in the universe that interacts gravitationally, and the monophoton channel provides a clean signature for searching of physics beyond the Standard Model. As for the monojet channel, similarly composed of events with a single high-energy jet, the predicted cross section is higher than the monophoton channel, but the monophoton channel uncertainties are smaller and the expected contributions from different subprocesses are slightly different.

2.2.1.3 Overview of the Current Status of Dark Matter Searches

Direct detection of Dark Matter particles have been reported over the last decade. The DAMA/LIBRA experiment use NaI(Tl) crystal scintillator detectors, and have been collecting data over 14 annual cycles. They reported a signal with 9.3σ significance [27] corresponding to the annual modulation expected from Weakly Interacting Massive Particles (WIMPs), a form of Dark Matter. The derived signal depends on the analysed target atom (Na or I), and the signal regions (solid red) are shown in Figure 2.4. The CoGeNT experiment uses germanium detectors, and with 3.4 years of gathered data reports an annual modulation of the signal with a significance of 2.2σ [28]. The signal best fit corresponds to a 7-11 GeV WIMP. An independent analyses using the same data but with different background models do not however find a significant signal [29]. The CDMS-II experiment use germanium and silicon detectors. The silicon detector finds three events above the expected background [30]. The WIMP+background hypothesis is favored over the background-only hypothesis with a probability of 0.19%. The signal highest likelihood corresponds to a WIMP with mass 8.6 GeV. The CRESST-II experiment in 2012, using a calcium tungstate scintillator finds an excess of events corresponding to signal best-fit for WIMP mass of 11.6 GeV or 25.3 GeV with significance of 4.2σ and 4.7σ respectively [31]. However, new results derived by the same collaboration using an upgraded detector with the same target element and improved background conditions could not reproduce this excess. Also the results from other experiments like XENON100 [33], LUX [34], SuperCDMS [35] and PandaX [36] completely exclude the parameter space of the signal hints described above. Below a WIMP mass of 6 GeV the best limits on this cross section are set by the CDMSlite experiment, which uses cryogenic germanium detectors. This experiment excludes the parameter space for the spin-independent scattering cross section for WIMP masses between 1.6 and 5.5 GeV [37]. Figure 2.4 compiles the current limits of direct detection ex-

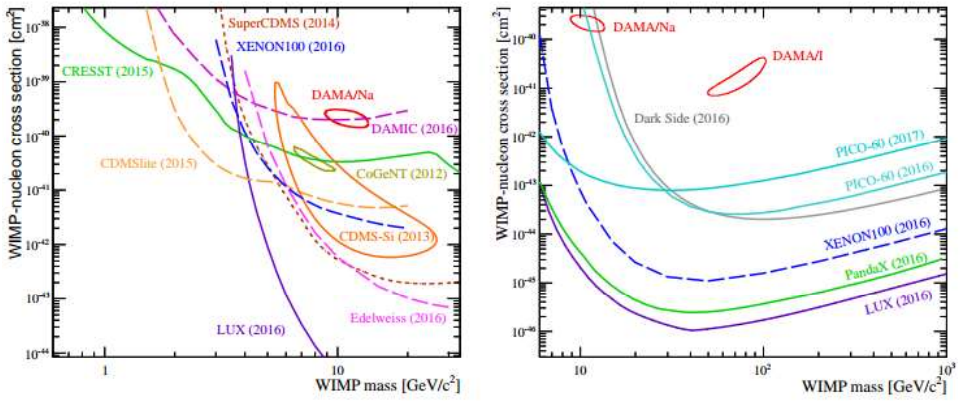

Figure 2.4: Overview of the signal indications and the current limits from direct detection experiments for spin-independent WIMP-nucleon cross section for low WIMP masses (left) and high WIMP masses (right) [32]

periments and the WIMP parameters reported by the experiments claiming signal observations.

For the spin-dependent case the best limits from a direct detection experiment on the scattering cross section for low-mass WIMPs are set by the PICO experiment. PICO operates two bubble chambers, one consisting of 52 kg of C3F8 [38, 39] and one consisting of 36.8 kg of CF3I [40]. PICO sets the most stringent constraint on the limit for the spin-dependent WIMP-proton cross section at $3.4\times10^{-41}\text{cm}^2$ for 30 GeV WIMPs [38]. PandaX sets the strongest limit for spin-dependent WIMP-neutron cross section at $4.1 \times 10^{-41}\text{cm}^2$ for 40 GeV WIMPs [41]. Also the limits on these cross sections are set by neutrino observatories, above 100 GeV the best limits are set by the IceCube [42] experiment, and below 100 GeV by the Super-Kamiokande [43] experiment. These are neutrino telescopes, and analyze the annihilation signal from WIMPs that have been captured inside the sun. Equilibrium between the capture and annihilation rates in the sun is assumed, and under this assumption, the rate of annihilation will depend on WIMP scattering off protons in the sun. This makes it possible to set limits on the spin-dependent interaction cross section. In particular, the sensitivity to spin-dependent interactions in this type of experiment is typically stronger than WIMP-nucleus recoil experiments. These limits are illustrated along

with the limits from PICO in Figure 2.5. Collider search results with the Run I CMS

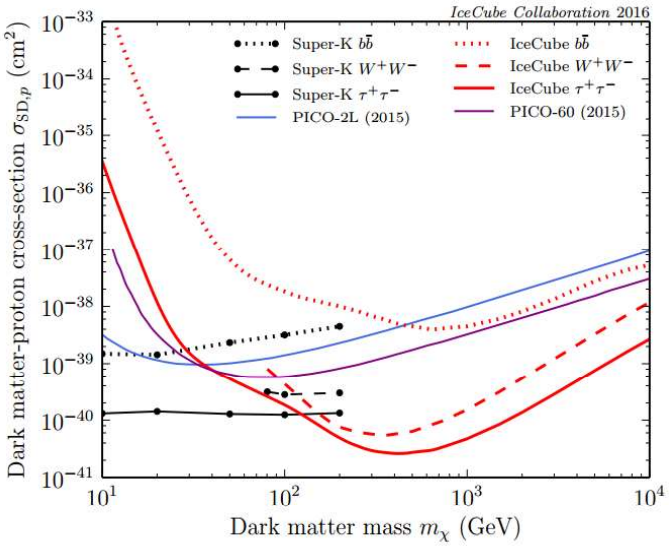

Figure 2.5: Overview of the current limits on the spin-dependent WIMP-nucleon cross section from recent experiments [42].

data for monophoton [44], monolepton [45] and monojet [46] channel are shown in Figure 2.6 on top of some direct and indirect detection results.

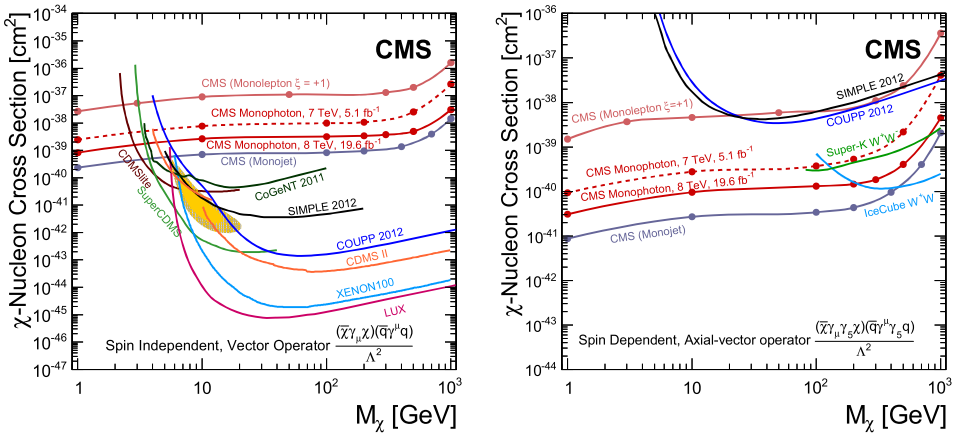

Figure 2.6: Overview of the 90% CL upper limits on the χ-nucleon cross section for spin-independent(left) and spin-dependent(right) couplings from various experiments [44].

2.2.2 Extra Spatial Dimensions

The goal of introducing extra spatial dimensions to unify the gravitational force with other interactions is older than the SM. In 1921 Theodor Kaluza [47] proposed a 5-dimensional spacetime in which the two known forces at the time, gravity and electromagnetism, were unified. The main assumption apart from assuming the fifth dimension itself, is the assumption that the first derivative of all physical quantities with respect to the fifth dimension must be zero,

$$\frac{\partial f(x)}{\partial x_5} = 0 \tag{2.22}$$

imposed in order to explain why the fifth dimension was not visible. This argument was refined by Oscar Klein [48,49], who interpreted it to mean that the fifth dimension is compactified on a cylindrical space, with dimension $\sim 10^{-30}$ cm. Compactification means that the fifth dimension is closed and periodic, so that $x_5 = x_5 + 2\pi R$, where R is the radius of the fifth dimension. The independence with respect to the fifth coordinate (2.22) is known as the cylindrical condition, and explains why the full 5-dimensional space is not visible to the underlying 4-dimensional subspace. In Kleins version of Kaluzas original theory, the standard 4-dimensional metric tensor is rewritten in five dimensions as:

$$\tilde{g}_{AB} = \begin{pmatrix} g_{\mu\nu} + A_\mu A_\nu & A_\mu \\ A_\nu & 1 \end{pmatrix} \tag{2.23}$$

where $g_{\mu\nu}$ is the standard 4-dimensional metric tensor, and A_μ is the electromagnetic 4-potential. Here the standard is to use greek letters for 4-dimensional objects and latin letters for higher dimensions. It can be shown that the geodesic equations of this metric tensor reproduce the Lorentz force, and Kaluza and Klein identified the component of velocity along the fifth axis with electric charge.

The theories of compactified extra dimensions were implemented into string theories in the later half of 20th century, for example the 11-dimensional M-theory [50]. String theories generally try to unify all forces, including gravity, by replacing the point-like particles of ordinary particle physics with 1-dimensional strings, or in more general formulations with p-dimensional branes. These fundamental strings, through their different vibrational states, give rise to all the observed particles and forces. String theories only make predictions for observable phenomena in energies far beyond the reach of any current experiment.

Theories with extra dimensions yielding measurable effects on the TeV-scale have been proposed, inspired by concepts developed in string theory. One of these is the theory proposed by Arkani-Hamed, Dimopolous and Dvali [51], which is covered in more detail below.

2.2.2.1 Large Extra Dimensions in the ADD Scenario

In the ADD model [51] n compact extra dimensions are added to the 3+1 spacetime dimensions. Gravity is allowed to propagate in these extra dimensions, sometimes denoted as the bulk, while the SM particles are only allowed to propagate in the standard 3+1-dimensions, denoted as the brane. This leads to gravity appearing to be weak over long distances, but on very short distances it is as strong as the other interactions. This theory is often referred to as a theory with Large Extra Dimensions, since for certain model parameters it may include compactified extra dimensions with radii up to μm-scale.

Following the example of Ref. [51] we assume n extra spatial dimensions of radius R. We denote the Planck scale of such a (4+n)-dimensional theory M_D. Two bodies with masses m_1 and m_2, positioned at a distance $r \ll R$ from each other will

experience a gravitational potential (using Gauss law):

$$V(r) \sim \frac{m_1 m_2}{M_D^{n+2}} \frac{1}{r^{n+1}} \tag{2.24}$$

If the test masses are instead put at a distance $r \gg R$, their gravitational flux lines can no longer propagate into the extra dimensions, and the potential becomes

$$V(r) \sim \frac{m_1 m_2}{M_D^{n+2} r^n} \frac{1}{r} \tag{2.25}$$

and the standard $1/r$-dependence is retrieved. This means the effective Planck scale $\bar{M_P} = M_P/8\pi$ observed at long distances is

$$\bar{M_P}^2 = M_D^{n+2} r^n \tag{2.26}$$

where the left hand side is now the standard effective Planck mass, and M_D^{n+2} is the fundamental Planck mass in 4 + n dimensions.

If gravity is to manifest itself at energy scales close to the electroweak scale m_{EW} we simply set the fundamental (4+n)-dimensional Planck scale to be $M_D \sim m_{EW}$. This yields for R

$$R = 10^{\frac{30}{n}-17}\text{cm} \times (\frac{1\text{TeV}}{m_{EW}})^{1+\frac{2}{n}} \tag{2.27}$$

The ADD model for gravity solves two fundamental problems of the SM. It provides an explanation for the apparent weakness of gravity. It also sets the fundamental Planck scale close to the electroweak scale leading to the elimination of the fine-tuning problem, since the cut-off scale providing the magnitude of the corrections to the Higgs mass, is now on the same order of magnitude as the electroweak scale (and thus the same order of magnitude as the Higgs mass itself).

2.2.2.2 Other Models with Extra Dimension

Another extra-dimension model is the Randall-Sundrum (RS) theory in which a warped fifth dimension is added to the 3+1 space-time dimensions [52]. This theory introduces a special non-factorizable metric tensor, where the 4-dimensional subspace of the 5-dimensional theory is x_5-dependent. The RS models predict two different branes, and whereas all other SM fields only reside on one, gravity lives on both. This dilutes the gravitational strength in the normal four dimensions much like the ADD model, while the fundamental scale of gravity is on the same order of magnitude as the weak scale. Furthermore there are models known as Universal Extra Dimensions (UED). Even if these specific theories of extra dimensions are not necessarily realized in Nature, they have the merit of being new ways of exploring possible reconciliation between gravity and the microscopic world.

2.2.2.3 ADD Collider Phenomenology

For $n = 1$, in order to obtain M_D at the TeV-scale, R must be of the order 10^{13} cm, yielding effects that would be noticeable at the scale of the solar system. This is excluded by observations. The case $n = 2, R \sim 10^{-2}$ cm, was exciting for new experiment like LHC, although recent results [53, 54] suggest that $n = 2$ could also be ruled out. For $n > 2$ however, the scale of the extra dimensions would be less than 10^{-7} cm, a region in which gravity has not been fully studied and also a region of interest for our study. An effective theory for the ADD scenario is outlined in Ref. [55], including the relevant inclusion of gravitons in the QED and QCD Lagrangians. This theory considers the interaction of the SM fields with a spin-2 graviton that can propagate in all $(4 + n)$ dimensions and mediates the gravitational interaction. The 4-dimensional projection of the massless graviton from the compactified extra dimensions gives rise to so called Kaluza-Klein tower of massive graviton modes. These massive graviton states appear as solutions to the free field

equations of any particle in compactified extra dimensions. We illustrate this below for the 5-dimensional Klein-Gordon equation for a massless spin-0 particle.

$$(\partial_A \partial^A \Phi(x_A) = (\partial_\mu \partial^\mu - \partial_5^2)\Phi(x_\mu, x_5) = 0 \tag{2.28}$$

Now we add the periodic boundary condition that $x_5 = x_5 + 2\pi R$, and Fourier expand the field to obtain

$$\Phi(x_\mu, x_5) = \sum_{k=-\infty}^{\infty} \phi_k(x_\mu) e^{\frac{ikx_5}{R}} \tag{2.29}$$

After this dimensional decomposition the equation of motion Eq. 2.30 yields for each of the fields ϕ_k:

$$\partial_\mu \partial^\mu \phi_k = \frac{k^2}{R^2}\phi_k \tag{2.30}$$

This is now an infinite *tower* of 4-dimensional fields with an extra mass term $m_k = \frac{k^2}{R^2}$, representing a discrete spectrum of mass modes. The same principle can be applied to any field, including the spin-2 graviton [56]. The difference in mass Δm between two mass modes m_k and m_{k+1} depends on the size of the extra dimensions. The full expression for the mass splittings in the ADD scenario is given by Ref. [55]:

$$\Delta m \sim \frac{1}{R} = M_D (\frac{M_D}{\bar{M}_P})^{\frac{2}{n}} \sim (\frac{M_D}{\text{TeV}})^{\frac{n+2}{2}} 10^{\frac{12n-31}{n}} \text{eV} \tag{2.31}$$

yielding for $M_D = 1$ TeV and $n = 2, 4$ or 6 a mass splitting of 0.3 meV, 20 keV and 7 MeV respectively.

The graviton modes couple to the energy-momentum tensor of the SM fields, and the interaction Lagrangian for a graviton field $G_{\mu\nu}^{(k)}$ is given by

$$\mathcal{L}_I = -\frac{1}{\bar{M}_P} G_{\mu\nu}^{(k)} T^{\mu\nu} \tag{2.32}$$

where $T^{\mu\nu}$ is the energy-momentum tensor of the SM fields.

The production of gravitons is suppressed by the fact that they only couple to the SM fields gravitationally. However, the large multiplicity of KK modes given by the small mass splitting in Eq. 2.31 makes the n-dimensional phasespace factor large enough to compensate for this.

The decay of the graviton is suppressed by a factor proportional to $\bar{M_P}^2/m_k^3$ where m_k is the mass of the graviton mode, and it is therefore stable on the time scales associated with detection in colliders. The gravitons will thus appear as a tower of massive, stable, non-interacting particles, and the means of searching for them is to look for missing momentum in events where a graviton is produced in association with a SM particle. Gravitons can directly be produced at the LHC via the reactions $gg \to qG, q\bar{q} \to gG, qg \to qG$ and $q\bar{q} \to \gamma G$, where G is a graviton. The first three processes will lead to a single high p_{T} jet and a large missing transverse momentum (p_{T}^{miss}) in the final state while the last process will give a single high p_{T} photon and p_{T}^{miss} in the final state. In this thesis, we are interested in the single high p_{T} photon and p_{T}^{miss} final state. The Feynman diagrams for the interaction $q\bar{q} \to \gamma G$ are shown in Figure 2.7. Since the contact interaction is the only one which is not propagator suppressed and increases with s, this will be the dominant contributor to direct graviton production at the LHC.

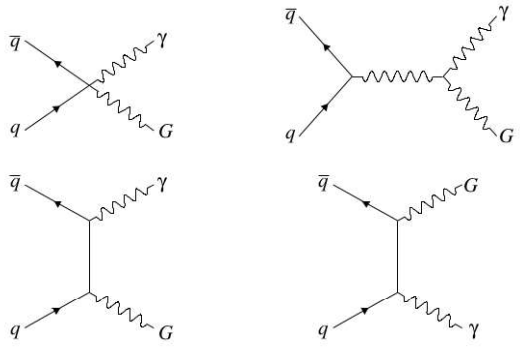

Figure 2.7: The production of gravitons at LHC through the process $q\bar{q} \to \gamma G$

2.2.2.4 Overview of the Status of Extra Dimensions Searches

To prove the existence of Large Extra Spatial Dimensions (as predicted in the ADD model), several experiments have been performed over the last decade. The best tabletop experiment limits on the small-distance behavior of gravity come from experiments with torsion pendulums, probing the Newtonian $1/r^2$ law to hold down to a distance of $\sim 55\mu$m [53]. Another direct detection experiment utilizes cryogenic micro-cantilevers capable of measuring attonewton forces, sets constraints on non-Newtonian forces at 10 microns [54].

Collider searches based on the ADD theory have been performed by searching for events with a single energetic jet or photon and large missing momentum in proton-antiproton collision events with the CDF experiment [57] and the D0 experiment [58] at the Tevatron, and in searches for events with photons and large missing momentum in electron-positron collision events with the LEP experiments [59] L3, OPAL, ALEPH and DELPHI. At the Large Hadron Collider with the multi-purpose experiments CMS and ATLAS, the searches for extra dimensions fall in three general categories: mono-X searches, searches for virtual graviton exchange and searches for black holes. In this section, only the mono-X search category will be discussed as my analysis fall in this category. The mono-X type searches look for signatures with a high energy jet or photon in association with missing momentum. The monophoton searches of CMS [44,60,61] and ATLAS [62,63] generally set weaker limits than the monojet searches, because of the higher production cross section associated with the strong interaction when compared to the electromagnetic. The strongest limits from monojet searches are the 8 TeV limits from the ATLAS experiment [64], which sets an upper limit on M_D at 3.06 TeV for $n = 6$ and 5.25 TeV for $n = 2$ (the limits for intermediate n are set between these two). The strongest CMS limits from the 8 TeV results [46] were between 2.99 TeV for $n = 6$ and 5.09 TeV for $n = 2$.

CHAPTER 3

Experimental Apparatus

3.1 The Large Hadron Collider

The Large Hadron Collider (LHC) [65] is the world's largest and most powerful particle accelerator. It is a two-ring-superconducting-hadron accelerator and collider installed in the existing 26.7 km tunnel that was constructed between 1984 and 1989 for the CERN Large Electron Positron (LEP) machine. The LHC tunnel has eight straight sections and eight arcs and lies between 45 m and 170 m below the earth surface near Geneva, Switzerland. Figure 3.1 shows the aerial view of LHC.

Figure 3.1: Aerial view of the LHC: The circles are drawn on the picture to show the LHC and the SPS rings. The two large rings correspond to the two LHC rings and the small ring corresponds to the SPS ring which is the main injector of the LHC. In reality all these rings are underground [66].

The aim of the LHC is to search for physics beyond the Standard Model using proton-proton collision at centre of mass energies up to 14 TeV. At its peak performance, the LHC is designed to hold 2808 proton bunches [65] and produce collisions every 25 ns with luminosity of $\mathrm{L} = 10^{34} cm^{-2} s^{-1}$ which corresponds to about a billion interactions per second, for the two experiments CMS and ATLAS, which are designed to collect data from high luminosity collisions. There are also two low luminosity experiments: LHCb and TOTEM. In addition to the proton beams, the LHC will also be operated with ion beams. The LHC has one dedicated ion experiment, ALICE. During the time that data were taken for the analysis presented in this thesis, the proton bunch collisions occurred every 25 ns with an energy of $\sqrt{s} = 13$ TeV.

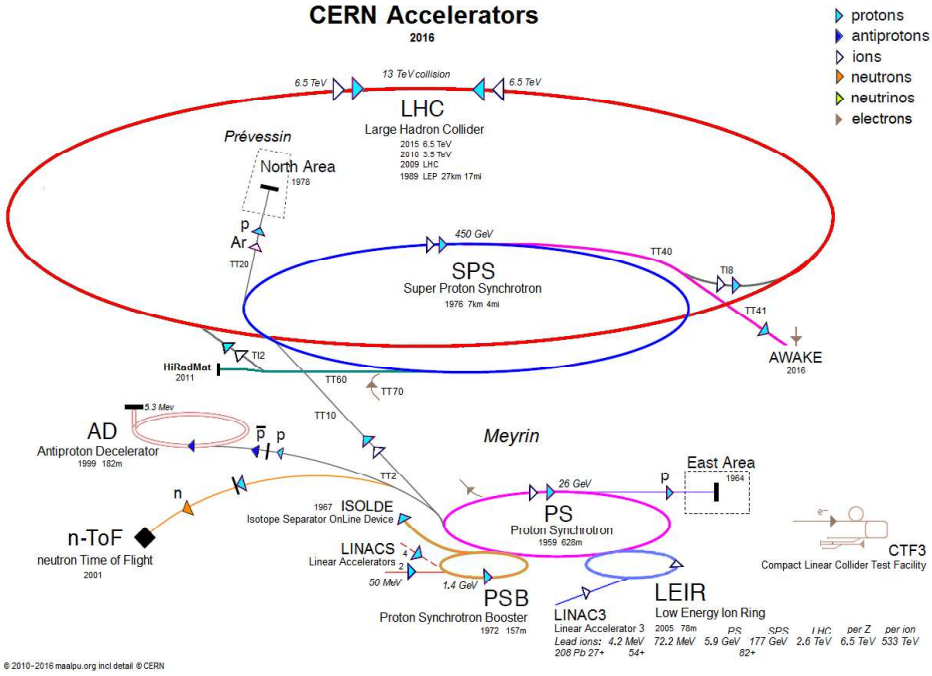

Figure 3.2: The schematic view of the CERN accelerator complex.

The LHC, at its peak performance, has 5×10^{14} protons circulating in each beam. Those protons are initially obtained from hydrogen gas. The gas is ionized with an electric field, separating the protons and the electrons. The protons then go through an acceleration sequence before they are injected into the LHC. The injection chain, shown in Figure 3.2, brings the protons through the linear accelerator (LINAC2),

Proton Synchrotron Booster (PSB), Proton Synchrotron (PS), and Super Proton Synchrotron (SPS) to accelerate them to energies compatible with the LHC design. Before passing to LINAC2, a multi-chamber resonance cavity, the particles are initially accelerated to 750 keV and focused into a segmented beam by a radio frequency quadrupole. The protons accelerate up to 50 MeV within microseconds moving through the LINAC2 on their way to the PSB. The Proton Synchrotron setup at CERN was the first major particle accelerator built at CERN, but now it is a part of the warm-up act for the LHC. The PSB accelerates the protons to 1.4 GeV in 530 ms, and within a microsecond they are injected into the Proton Synchrotron. The PS accelerates the protons to 25 GeV and organizes them into bunch packets with uniform spacing appropriate to the collision rate of the LHC run. At the design performance, 81 bunch packets are formed with a 25 ns, or 8 m, spacing between bunches. Lastly, the protons are accelerated to 450 GeV in 4.3 seconds and sent to the LHC. Once the proton beam is sent to the LHC, the individual proton bunches usually wait to be put in appropriate places along the beam line. Waiting for a proton bunch to be injected and then ramping up to high energy takes about 45 minutes and is the longest part of the injection chain.

3.2 The Compact Muon Solenoid Detector

The Compact Muon Solenoid (CMS) detector [67] is a multi-purpose apparatus located at one of the straight sections of the LHC about 100 meters below the ground near the French village of Cessy, between Lake Geneva and the Jura mountains. The following points are taken into account as the detector requirements for the CMS to meet the goals of the LHC physics programme [67].

- Good muon identification and momentum resolution over a wide range of momenta and angles, good di-muon mass resolution ($\approx 1\%$ at 100 GeV), and

the ability to determine exactly the charge of muons with $p < 1$ TeV;

- Good momentum resolution and reconstruction efficiency for charged particles in an inner tracking system. Efficient triggering and offline tagging of τs and b-jets, requiring pixel detectors close to the interaction region;

- Good electromagnetic energy resolution, good di-photon and di-electron mass resolution ($\approx 1\%$ at 100 GeV), wide geometric coverage, good π^0 rejection, and efficient photon and lepton isolation at high luminosities;

- Good missing-transverse-energy and di-jet mass resolution, requiring hadron calorimeters with a large hermetic geometric coverage and with fine lateral segmentation.

The design of the CMS, meets these requirements. The main distinguishing features of CMS are a high-field solenoid, a full-silicon-based inner tracking system, and a homogeneous scintillating-crystals-based electromagnetic calorimeter.

The coordinate system adopted by CMS has the origin centered at the nominal collision point inside the experiment, the y-axis pointing vertically upward, and the x-axis pointing radially inward toward the center of the LHC. Thus, the z-axis points along the beam direction toward the Jura mountains from LHC Point 5. The azimuthal angle ϕ is measured from the x-axis in the $x - y$ plane and the radial coordinate in this plane is denoted by r. The polar angle θ is measured with respect to the z-axis. Pseudorapidity is defined as $\eta = \ln \tan(\theta/2)$. Thus, the momentum and energy transverse to the beam direction, denoted by p_T and E_T , respectively, are computed from the x and y components. The imbalance of energy measured in the transverse plane is denoted by E_T^{miss} .

The CMS detector is 21.6 m long and has a diameter of 14.6 m. It has a total weight of 12500 ton. The components of the detector, listed in the order that the collision products encounter them, are: the tracker, the crystal electromagnetic calorimeter

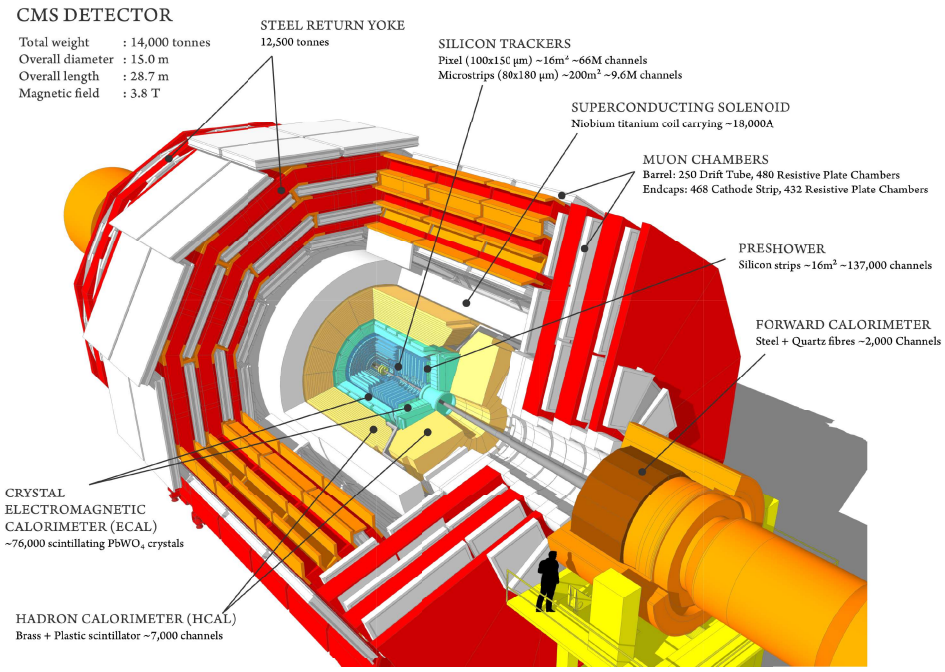

Figure 3.3: A schematic diagram of the CMS detector showing all the major components [68].

(ECAL), the hadron calorimeter (HCAL), a 3.8 T solenoid magnet, and a muon system composed of three different kinds of detectors. The illustration of the CMS detector in Figure 3.3 shows how the different components fit together.

3.2.1 Inner Tracking System

The inner tracking system of the CMS is designed to provide a precise and efficient measurement of the trajectories of charged particles emerging from the LHC collisions, as well as a precise reconstruction of secondary vertices. It surrounds the interaction point and has a length of 5.8 m and a diameter of 2.5 m. The CMS tracker is composed of a pixel detector with three barrel layers at radii between 4.4 cm and 10.2 cm and a silicon strip tracker with 10 barrel detection layers extending outwards to a radius of 1.1 m. Each system is completed by endcaps which consist of 2 disks for the pixel detector and 3 plus 9 disks for the strip tracker on either

side of the barrel, extending the acceptance of the tracker up to a pseudorapidity of $|\eta| < 2.5$. With about 200 m^2 of active silicon area, the CMS tracker is the largest silicon tracker built so far [69, 70].

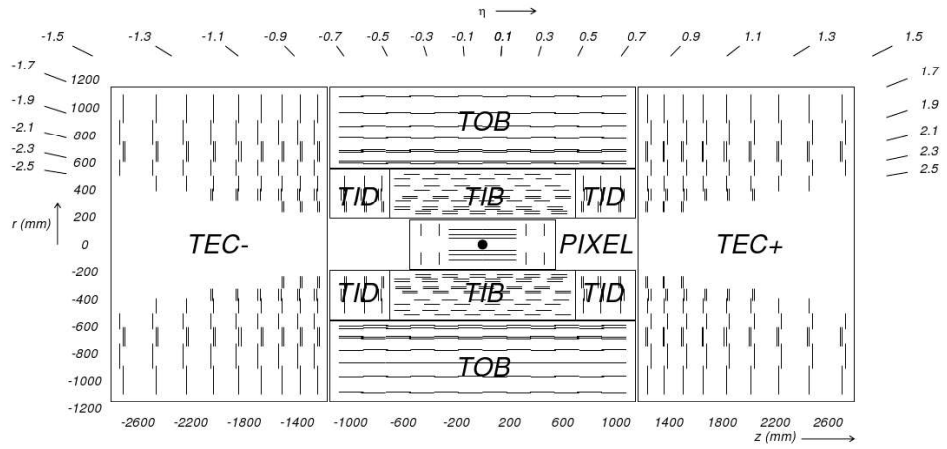

Figure 3.4: Schematic cross section through the CMS tracker. Each line represents a detector module. Double lines indicate back-to-back modules which deliver stereo hits [67].

A schematic drawing of the CMS tracker is shown in Figure 3.4. The CMS tracker is composed of two components: the pixel detector and the silicon strip tracker.

3.2.1.1 Pixel detector

The pixel detector is designed to be able to make high precision 3D measurements close to the interaction region. The pixel detector covers a pseudorapidity range $-2.5 < \eta < 2.5$, matching the acceptance of the strip tracker. It consists of three barrel layers (BPix) with two endcap disks (FPix). The 53 cm long BPix layers are located at mean radii of 4.4, 7.3 and 10.2 cm. The FPix disks extending from 6 to 15 cm in radius, are placed on either side at $|z| = 34.5$ and $|z| = 46.5$ cm. BPix (FPix) contains 48 million (18 million) pixels covering a total area of 0.78 (0.28) m^2. The pixel detector gives three high precision tracking points over almost the full $\eta-$range on each charged particle trajectory. With a pixel cell size of 100×150 μm^2, the pixel detector provides a spatial resolution in the range of $15 - 20$ μm.

3.2.1.2 Silicon strip tracker

Beyond the pixel detector, the radial region between 20 cm and 116 cm is occupied by the silicon strip tracker. It is composed of three different subsystems. The Tracker Inner Barrel and Disks (TIB/TID) extend in radius up-to 55 cm and are composed of 4 barrel layers, supplemented by 3 disks on either end. TIB/TID provides up to four $r-\phi$ measurements on a trajectory using 320 μm thick silicon micro-strip sensors with their strips parallel to the beam axis in the barrel and radial on the disks. The strip pitch is 80 μm on layers 1 and 2 and 120 μm on layers 3 and 4 in the TIB, leading to a single point resolution of 23 μm and 35 μm, respectively. In the TID the mean pitch varies between 100 μm and 141 μm.

The TIB/TID is surrounded by the Tracker Outer Barrel (TOB). It has an outer radius of 116 cm and consists of 6 barrel layers of 500 μm thick micro-strip sensors with strip pitches of 183 μm on the first 4 layers and 122 μm on layers 5 and 6. It provides another six $r-\phi$ measurements with single point resolution of 53 μm and 35 μm, respectively. The TOB extends in z between $\pm$118 cm.

Beyond this z range the Tracker EndCaps (TEC+ and TEC$-$ where the sign indicates the location along the z axis) cover the region 124 cm $< |z| <$ 282 cm and 22.5 cm $< r <$ 113.5 cm. Each TEC is composed of 9 disks, carrying up to 7 rings of silicon micro-strip detectors (320 μm thick on the inner 4 rings, 500 μm thick on rings 5-7) with radial strips of 97 μm to 184 μm average pitch. Altogether, the TEC can make up to 9 ϕ measurements on a passing charged particle.

In addition, the first two layers of TIB and TOB, the first two rings of TOB and rings 1, 2, and 5 of the TECs carry a second micro-strip detector module which is mounted back-to-back with a stereo angle of 100 mili radian in order to provide a measurement of the second co-ordinate (z in the barrel and r on the disks). The achieved single point resolution of this measurement is 230 μm and 530 μm in TIB

and TOB, respectively, and varies with pitch in TID and TEC. This tracker layout ensures at least 9 hits in the silicon strip tracker in the full range of $|\eta| < 2.4$ with at least 4 hits of them provide two-dimensional information for the track.The CMS silicon strip tracker has a total of 9.3 million strips and 198 m^2 of active silicon area.

3.2.2 Electromagnetic Calorimeter

The Electromagnetic Calorimeter (ECAL) [71] is designed to measure the energy of electrons and photons. It is a homogeneous calorimeter made of 61200 lead tungstate ($PbWO_4$) crystals mounted in the central barrel part while 7324 crystals sit on either side in the two endcaps. A preshower detector is placed in front of the endcap crystals. Avalanche photodiodes (APDs) are used as photo-detectors in the barrel and vacuum phototriodes (VPTs) in the endcaps. The characteristics [72] of the $PbWO_4$ crystals make them an appropriate choice for operation at the LHC. The high density (8.28 g/cm^3), short radiation length (0.89 cm) and small Molière radius (2.2 cm) result in a fine granularity and a compact calorimeter. The crystals are also fast, emitting 80% of the light from interactions within 25 ns, and are radiation hard. The crystals emit blue-green scintillation light with a broad maximum at 420-430 nm.

The barrel part of the ECAL (EB) covers the pseudorapidity range $|\eta| < 1.479$. The barrel granularity is 360-fold in ϕ and (2×85)-fold in η, resulting in a total of 61200 crystals. The crystals have a tapered shape and are aligned in a quasi-projective manner with respect to an axis about 3^0 off of the nominal interaction point, in order to avoid lining cracks up with particle trajectories. The crystal cross section corresponds to approximately 0.0174×0.0174 in $\eta - \phi$ space or 22×22 mm^2 at the front face of crystal, and 26×26 mm^2 at the rear face. The crystal length is 230 mm corresponding to 25.8 radiation lengths (X_0) .

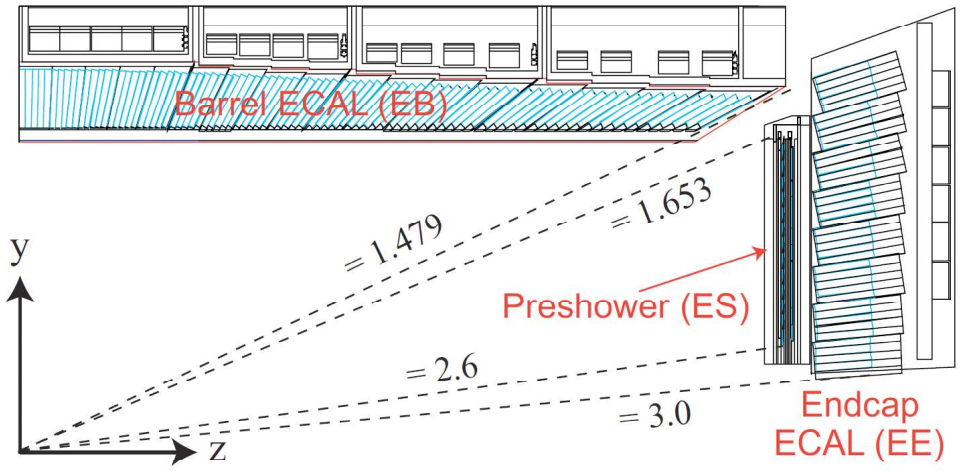

Figure 3.5: The η coverage of the ECAL [71].

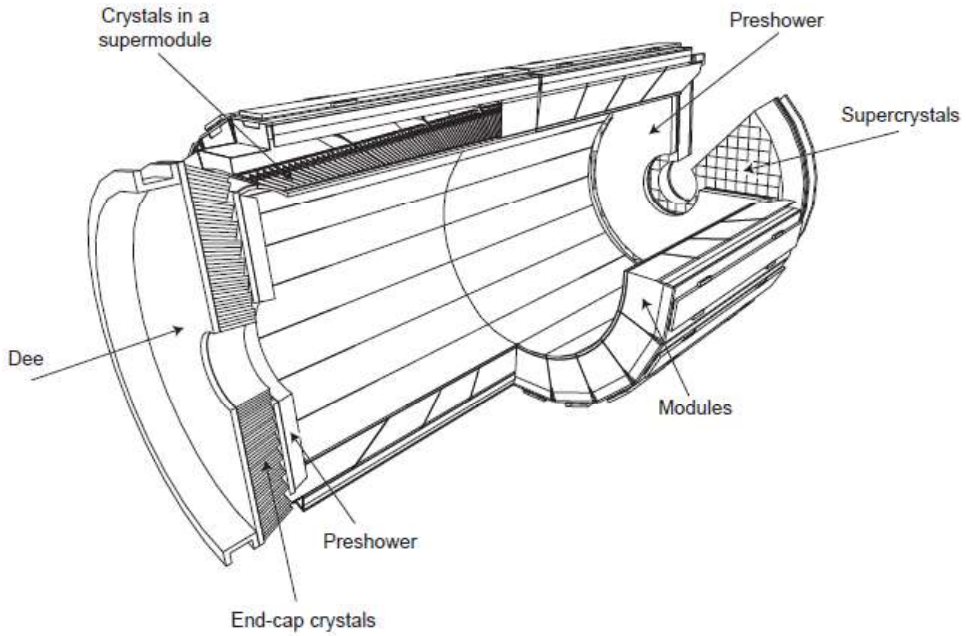

Figure 3.6: Layout of the CMS electromagnetic calorimeter showing the arrangement of crystal modules, supermodules and endcaps, with the preshower in front [67].

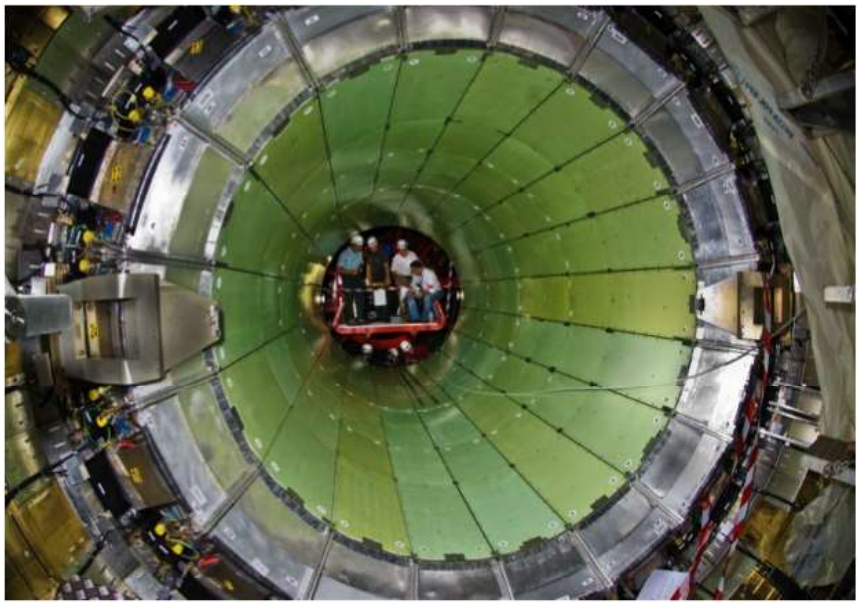

Figure 3.7: The barrel electromagnetic calorimeter positioned inside the hadron calorimeter [67].

Figure 3.8: An endcap Dee, fully equipped with supercrystals [67].

The endcaps (EE) cover the rapidity range $1.479 < |\eta| < 3.0$. The longitudinal distance between the interaction point and the endcap envelope is 315.4 cm, taking account of the estimated shift toward the interaction point by 1.6 cm when the 4-T magnetic field is switched on. The endcap consists of identically shaped crystals grouped in mechanical units of 5×5 crystals (supercrystals or SCs). Each endcap is divided into 2 halves, or Dees. Each Dee holds 3662 crystals. The crystals and SCs are arranged in a rectangular $x - y$ grid, with the crystals pointing at a focus 1300 mm beyond the interaction point, giving off-pointing angles ranging from 2 to 8 degrees. The crystals have a rear face cross section 30×30 mm^2, a front face cross section 28.62×28.62 mm^2 and a length of 220 mm (24.7 X_0). The layout of the calorimeter is shown in Figure 3.6. Figure 3.7 shows the barrel detector already mounted inside the hadron calorimeter, while Figure 3.8 shows a picture of a Dee.

The preshower detector covers the pseudorapidity range $1.653 < |\eta| < 2.6$ and sits in front of the EE for extra spatial precision on ECAL measurements, helping to distinguish between single high-energy photons and collimated photon pairs from π^0 decays. The Preshower is a sampling calorimeter with two layers: lead radiators initiate electromagnetic showers from incoming photons/electrons whilst silicon strip sensors placed after each radiator measure the deposited energy and the transverse shower profiles. The total thickness of the Preshower is 20 cm. The material thickness of the Preshower traversed at $\eta = 1.653$ before reaching the first sensor plane is $2X_0$, followed by a further $1X_0$ before reaching the second plane. Thus about 95% of single incident photons start showering before the second sensor plane.

The energy resolution of the ECAL was studied in the 2006 CERN test beam experiment [67] and can be expressed as a function of energy in terms of its individual components:

$$(\sigma/E)^2 = (2.8\%/\sqrt{E})^2 + (12\%/E)^2 + (0.30\%)^2, \tag{3.1}$$

where E is in GeV. The $1/\sqrt{E}$ term is related to stochastic fluctuations in EM

showers, the $1/E$ term is related to the electronics noise and the constant term includes calibration errors.

3.2.3 Hadron Calorimeter

The Hadronic Calorimeter (HCAL) [73] is a sampling calorimeter composed of alternating layers of brass or steel absorber and plastic scintillator. It is used to measure energies of hadronic jets and missing transverse energy due to neutrinos or other exotic sources. Hadrons pass through the dense absorber and interact with the nuclei, producing secondary particles which also interact with the absorber material and produce a cascade of particles, also known as a hadronic shower. The hadronic shower then pass through the scintillator and interact, causing the scintillator to fluoresce, and the signals collected in the different layers of scintillator are combined to measure the energy of the hadrons.

The HCAL is composed of alternating layers of brass absorber and Kuraray SCSN81 plastic scintillator [74]. The plastic scintillator is chosen for its long-term stability and moderate radiation hardness and the brass is chosen because it is dense, non-magnetic and structurally stable. The scintillator emits light in the blue-violet range which goes through wavelength-shifting fibers embedded in the scintillator to hybrid photodiodes (HPD), which convert the signals into electrical pulses. The HCAL consists of about 70000 scintillator tiles, which are sandwiched between brass absorber layers to form projective towers that measure hadronic showers energy.

The HCAL layout is shown in Figure 3.9. The HCAL has three major components: $|\eta| < 1.3$ is the barrel HCAL region (HB), the endcap HCAL component (HE) covers $1.3 < |\eta| < 3.0$, and the forward component (HF) extends to cover $3.0 < |\eta| < 5.2$. HB is divided into two identical half barrels on either side of the interaction point. Each half barrel consists of 18 identical azimuthal wedges, each of which

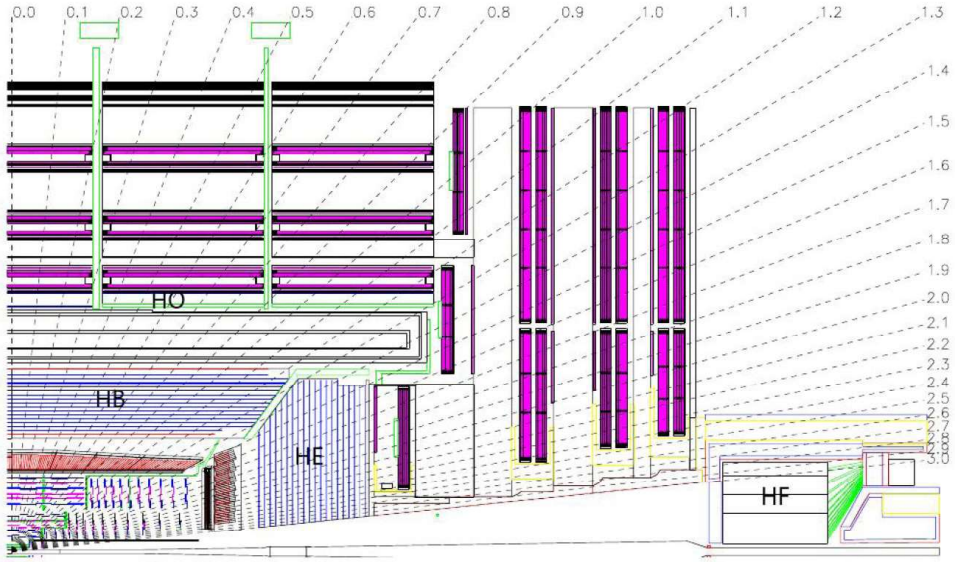

Figure 3.9: Longitudinal view of the CMS detector showing the locations of the hadron barrel (HB), endcap (HE), outer (HO) and forward (HF) calorimeters [67].

covers 20 degrees in ϕ. Each wedge is further divided into four azimuthal sectors giving a granularity of $\Delta\phi = 0.087$. Each azimuthal wedge is segmented into 16 partitions along the $z-$direction giving a granularity of $\Delta\eta = 0.087$. The total absorber thickness at $\eta = 0$ is 5.82 interaction lengths (λ_I). The effective thickness of HB increases as a function of $1/\sin\theta$, resulting in $10.6\lambda_I$ at $|\eta| = 1.3$. The presence of the ECAL crystal in front of HB adds an additional $1.1\lambda_I$. In the barrel region, the combined stopping power of EB plus HB does not provide sufficient containment for hadron showers. To ensure adequate sampling depth for $|\eta| < 1.3$, the hadron calorimeter is extended outside the solenoid with a tail catcher called the HO or outer hadron calorimeter. The HO utilizes the solenoid coil as an additional absorber equal to $1.4/\sin\theta$ interaction lengths and is used to identify late starting showers and to measure the shower energy deposited after HB. The total depth of the calorimeter system is thus extended to a minimum of $11.8\lambda_I$ except at the barrel-endcap boundary region.

HE is also a sampling calorimeter composed of 17 layers with 79 mm thick brass absorber plates with 3.7 mm thick scintillator plates (9 mm thick Bicron scintillator

for layer 0). The granularity in $\Delta\eta \times \Delta\phi$ is 0.087×0.087 up to $|\eta| < 1.6$ and 0.17×0.17 for $|\eta| > 1.6$. HE has one tower ($i\eta = 16$) overlapping with HB. HE has a minimum depth of about $10\lambda_I$.

The HF is 11 m away from the interaction point but very close to the beam axis and is designed with steel absorbers and quartz scintillating fibers, which were selected because of their radiation-hard properties that will survive the particle flux at high η, which will deposit nearly 8 times as much energy compared to activity in the barrel. In the forward region, signals are read out with photomultiplier tubes.

3.2.4 The Muon System

As the name implies, the CMS design places a lot of importance on the muon system. Many interesting predicted physics phenomena decay to muons, such as the Standard Model Higgs boson into ZZ or ZZ*, which in turn decay into 4 leptons, has been called "gold plated" for the case in which all the leptons are muons as muons have very clean signature and are less affected than electrons by radiative losses in the tracker material. This example, and others from SUSY models, emphasize the discovery potential of muon final states and the necessity for wide angular coverage for muon detection.

The muon system has 3 functions: identification of muons, momentum measurement, and triggering. Good muon momentum resolution and trigger capability are enabled by the high field solenoidal magnet and its flux-return yoke. Due to the shape of the solenoid magnet, the muon system is naturally driven to have a cylindrical, barrel section and 2 planar endcap regions. Because the muon system consists of about 25000 m^2 of detection planes, the muon chambers are chosen with the characteristics: inexpensive, reliable, and robust.

CMS uses 3 types of gaseous particle detectors for muon identification [75]: the drift

tube (DT) chambers, cathode strip chambers (CSC), and Resistive Plate Chambers (RPC), all shown in Figure 3.10. The muon detector elements cover the full pseudorapidity interval $|\eta| < 2.4$ with no acceptance gaps. It is capable of reconstructing muons in the kinematic range from 10 GeV $< p_{\mathrm{T}} <$ 1 TeV with $|\eta| < 2.4$ [76].

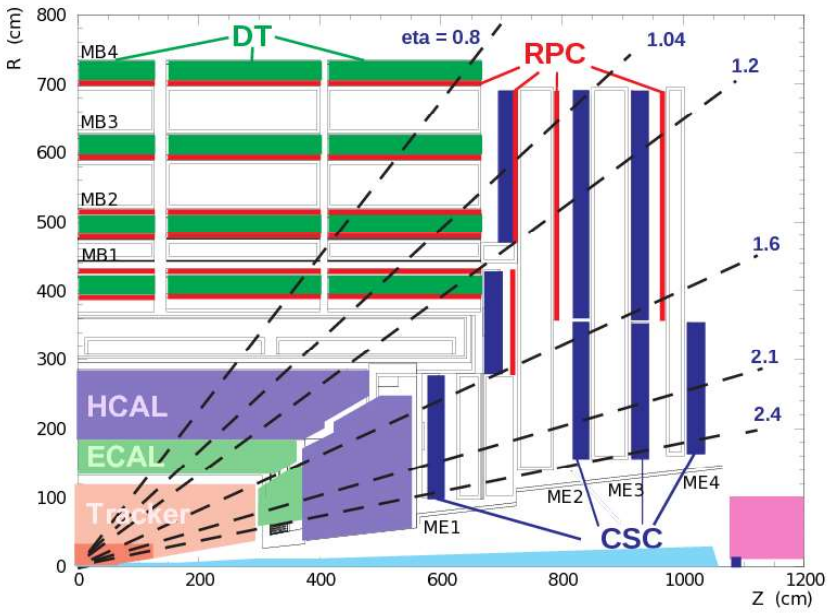

Figure 3.10: Layout of one quadrant of CMS. The four DT stations in the barrel (MB1-MB4, green), the four CSC stations in the endcap (ME1-ME4, blue), and the RPC stations (red) are shown [76].

3.2.4.1 Drift tube system

The barrel drift tube (DT) chambers cover the pseudorapidity region $|\eta| < 1.2$ and are organized into 4 stations forming concentric cylinders around the beam line: the 3 inner cylinders have 60 drift chambers each and the outer cylinder has 70. There are about 172000 sensitive wires. The wire length, around 2.4 m in the chambers measured in an $r - \phi$ projection, is constrained by the longitudinal segmentation of the iron barrel yoke. The transverse dimension of the drift cell, i.e., the maximum path and time of drift, is chosen to be 21 mm (corresponding to a drift time of 380 ns in a gas mixture of 85% Ar + 15% CO_2). With this design, a position resolution of

100 μm in $r - \phi$ is achieved.

3.2.4.2 Cathode strip chambers

The CSC's are used for measurement of muons in the endcaps, where the neutron flux is large and magnetic field is non-uniform. These are multi-wire proportional chambers comprised of 6 anode wire planes interleaved among 7 cathode panels. Wires run azimuthally and define radial coordinate of a track. Strips are milled on cathode panels and run lengthwise at constant $\Delta\phi$ width. The CSC's are radiation hard, provide a fast response time for trigger purposes, and are finely segmented which provide good spatial resolution. A muon in the pseudorapidity range $1.2 < |\eta| < 2.4$ crosses 3 or 4 CSC's. In the endcap-barrel overlap range, $0.9 < |\eta| < 1.2$, muons are detected by both the barrel drift tubes and endcap CSC's.

3.2.4.3 Resistive plate chambers

Resistive Plate Chambers (RPC) are gaseous parallel-plate detectors that combine adequate spatial resolution with a time resolution comparable to that of scintillators. An RPC is capable of tagging the time of an ionizing event in a much shorter time than the 25 ns between 2 consecutive LHC bunch crossings (BX). Therefore, a fast dedicated muon trigger device based on RPC's can identify unambiguously the relevant BX to which a muon track is associated even in the presence of the high rate and background expected at the LHC. Signals from such devices directly provide the time and position of a muon hit with the required accuracy.

The CMS RPC consists of 2 gaps, hereafter referred as up and down gaps, operated in avalanche mode with common pick-up read-out strips in between. The total induced signal is the sum of the 2 single-gap signals. This allows the single-gaps to operate at lower gas gain (lower high voltage) with an effective detector efficiency

higher than for a single-gap. In the endcaps, the RPCs are designed to cover $|\eta| < 1.6$ in three layers.

3.2.5 The Trigger System

When LHC is performing at its peak luminosity, the LHC produces 40 million collisions in the CMS detector every second. There is not enough time to process that much information, and even if there is, most of the collisions will produce scattering events and other low-energy interactions that are unlikely to reveal new physics.

We therefore need a "trigger system" [77, 78] that can select the potentially interesting events, such as those which will produce the Higgs particle, and reduce the rate to just a few hundred "events" per second, which can be read out and stored on computer disk for subsequent analysis. In order to maintain a high selection efficiency with the given time and computing constraints, the trigger selection process is split into two steps: The Level-1 (L1) trigger and the High Level Trigger (HLT).

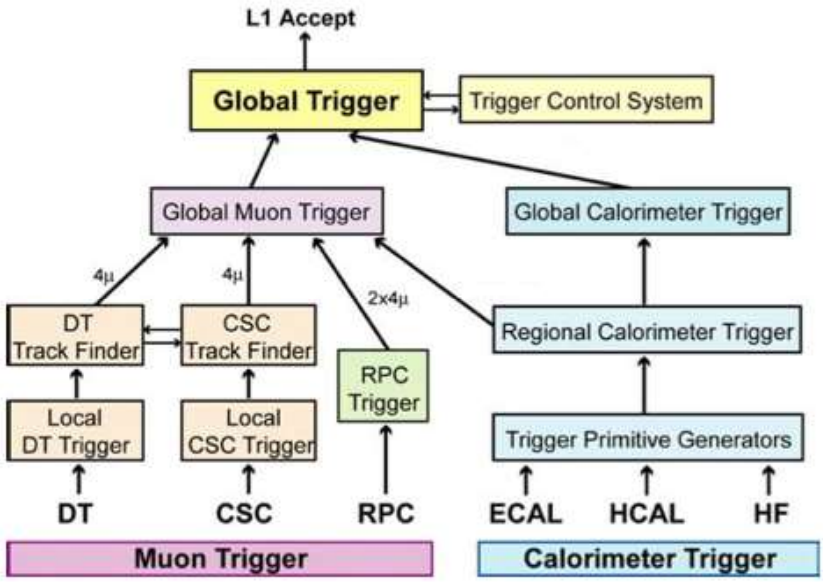

Figure 3.11: Architecture of the CMS Level 1 Trigger [67].

The L1 trigger is an intermediate step designed to reduce the rate of collisions saved

for further processing from 40 MHz to 100 kHz. Figure 3.11 shows the architecture of the CMS Level 1 Trigger. Digitized signals from the detectors are first processed into trigger primitives which contain information like position, direction, bunch crossing, and quality information. The trigger primitives are collected and built into larger objects to see if the event passes local, regional, and finally global selection thresholds while the rest of the event information is held in the pipeline. The selection thresholds, collectively referred to as the trigger menu, do not change unless the beam energy or instantaneous luminosity increases, in which case they are raised or prescaled. The L1 selection must be accomplished within $\sim$1 μs; the front-end electronics can store event information for 3 μs, corresponding to the information from 128 bunch crossings, and time is lost due to latency and processing. Based on the reduced intermediate rate event, the L1 trigger sends an event to the HLT once every 10 μs.

While L1 is controlled by mostly preprogrammed electronics, the HLT is a fully programmable software system run on commercial processors. The HLT, which is run by the Data Acquisition (DAQ) system, has access to all of the sub-detector information from each event and is able to build physics objects, like jets and photons, and execute complex calculations. The processing time for a single event is about 1 second, and the HLT reduces the data flow to 100 Hz, which is a level that can be read out and stored to disk.

CHAPTER 4

Event and Object Reconstruction

The reconstruction process, like the trigger system, progresses in steps. The first step in reconstruction is to convert the digitized signals from the sub-detectors into "hits" which include energy, timing, and global detector position information. Various algorithms are used to combine these hits into 4-vector information associated with more complex objects or particle candidates. In many cases, some of these first steps are accomplished by the trigger as a means of identifying collisions with events of interest and are later rerun offline during reconstruction.

The CMS experiment utilizes a Particle Flow (PF) algorithm [79] designed to uniquely identify all stable particles from each pp collision event by combining information from all CMS sub-detectors. The PF approach is possible in CMS due to the excellent position and energy resolution of the CMS silicon tracker and electromagnetic calorimeter. The track reconstruction algorithm makes use of an iterative pattern recognition algorithm designed to maintain high efficiency in the dense environment typical for jets, as well as a low probability of misreconstructed tracks. The tracking misreconstruction rate is less than a per cent even for the most difficult scenarios, such as low p_{T} ($\sim 100\mathrm{MeV}/c^2$) tracks originating far from the beam axis. For calorimeter deposits, a specific clustering algorithm is used which is opti-

mized to maintain high efficiency for low-energy particles and to effectively separate nearby deposits. A **linking** algorithm is then used to associate tracks with calorimetric deposits. The PF algorithm identifies muons by comparing silicon tracks to tracks reconstructed by the CMS muon system, and electrons are reconstructed and identified using tracking and calorimetric variables. The remaining particles are identified as charged hadrons, neutral hadrons, or photons by comparing the momentum of tracks with the calorimeter deposits. The final list of PF particles is used to apply more precise identification cuts, as input to a jet algorithm, or to compute missing energy. In this chapter, an overview of reconstruction of photon and missing transverse momentum (p_{T}^{miss}), which are most important for this analysis are discussed.

4.1 Photon

4.1.1 Photon Reconstruction

Photon candidates are reconstructed from clusters of energy deposited in the ECAL. Photons are expected to deposit most, if not all, of their energy in the crystals of the ECAL, and some spread is expected in the energy deposition since the material in front of the ECAL can result in early conversions and bremsstrahlung from electrons and positrons, and the strong magnet will cause these charged particles to deposit their energy in a broader region in ϕ. For this reason, the first step of photon reconstruction [80] is to group the crystals with energy depositions that appear to come from the same source object using a superclustering algorithm [81]. The Hybrid superclustering algorithm, which is used in the barrel region of the detector, first searches for a seed in the ECAL barrel with the largest energy deposit above a well defined threshold $E_{\mathrm{T,seed}}^{\mathrm{min}}$. A number of arrays of 5×5 crystals in the $\eta - \phi$ plane is added around the seed in a range of N_{steps} crystal if the energy exceeds the threshold

$E^{\text{min}}_{\text{array}}$. The arrays are then collected into clusters, whereby each cluster is required to have a seed array with an energy larger than $E^{\text{min}}_{\text{seed-array}}$. All clusters satisfying this requirement are stored in the final global supercluster (SC). The corresponding threshold values for the barrel region are summarized in Table 4.1. The superclusters in the ECAL endcap and preshower regions are reconstructed in a similar but less segmented manner, by the Multi-5×5 algorithm which adds together fixed 5×5 arrays of clustered crystals [81]. In both cases, once the supercluster has been formed, the supercluster energy is corrected for losses due to interactions with the material in front of the ECAL and the shower containment of the supercluster. A correction is applied to account for: the η dependence of the lateral energy leakage due to the 3° offset in the ECAL; energy lost through interactions with the material in front of the ECAL; and the variation in material encountered before the ECAL [80]. These corrections are developed using simulated samples and usually correspond to 1% of the supercluster energy.

Parameter	Value
$E^{\text{min}}_{\text{T,seed}}$	1 GeV
$E^{\text{min}}_{\text{seed-array}}$	0.35 GeV
$E^{\text{min}}_{\text{array}}$	0.1 GeV
N_{steps}	17 ($\approx$ 0.3 rad)

Table 4.1: Threshold values of parameters used in the hybrid superclustering algorithm in the barrel [81]

Photon objects are reconstructed by connecting superclusters to the primary vertex in an event, creating a way to calculate the momentum and trajectory of the photon. The energy assigned to the reconstructed photon is calculated in one of two ways, depending on the distribution of the energy in the photon object. The energy distribution is determined by the variable $R9$, which is defined as the ratio of energy deposited in the 3×3 cluster of crystals around the crystal seed to the energy deposited in the entire supercluster, $R9 = E_{3\times3}/E_{SC}$, and shown in Figure 4.1 for data and simulated events. If $R9 < 0.94$, the energy is spread broadly across the

shower which could indicate that the photon converted prior to reaching the ECAL and the photon object is assigned the energy of the supercluster. If $R9 > 0.94$, the energy in the supercluster is very collimated and indicative of an unconverted photon; the photon object is assigned the energy of the 5×5 crystal array surrounding the crystal seed. The position of the reconstructed photon is subsequently calculated as the log-energy-weighed average position of the crystals in the cluster used to determine the energy.

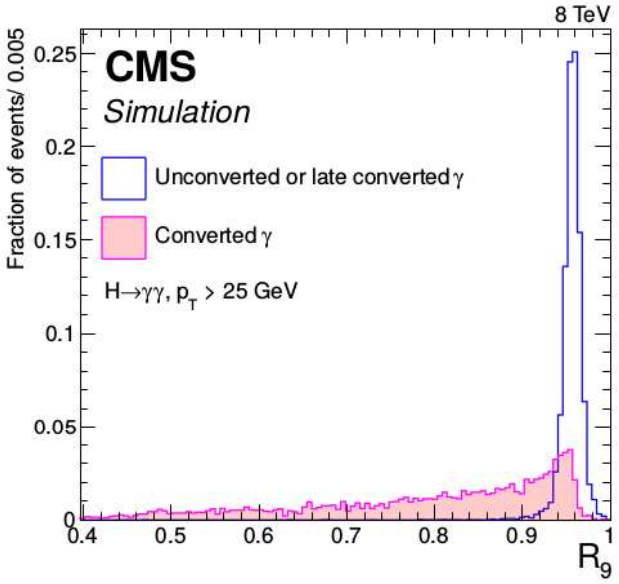

Figure 4.1: Distributions of the $R9$ variable for photons in the ECAL barrel that convert in the material of the tracker before a radius of 85 cm (solid filled pink histogram), and those that convert later, or do not convert at all before reaching the ECAL (outlined blue histogram) [80].

4.1.2 Photon Identification

During photon reconstruction, a number of variables relating to the photon candidate are defined that can be used to further distinguish photons from electrons, jets, and other objects that leave similar energy signals in the ECAL. The variables which are used for photon identification (Photon ID), are discussed below:

Shower shape ($\sigma_{i\eta i\eta}$): The electromagnetic shower distribution, commonly referred to as the shower shape, is determined by its width in $i\eta$-space using the variable $\sigma_{i\eta i\eta}$ which is calculated as follows:

$$\sigma^2_{i\eta i\eta} = \frac{\sum_{i=1}^{5\times5} w_i(\eta_i - \bar{\eta}_{5\times5})^2}{\sum_{i=1}^{5\times5} w_i}, \quad \text{where } w_i = max(0, 4.7 + \ln\frac{E_i}{E_{5\times5}}) \tag{4.1}$$

where the index i runs over all the crystals within the 5×5 electromagnetic cluster centered on the seed crystal; E_i and η_i are the energy and pseudorapidity of the i^{th} crystal within the 5×5 cluster; $E_{5\times5}$ is the energy of the entire 5×5 cluster and $\bar{\eta}_{5\times5}$ is the energy weighted mean η position of the 5×5 cluster. $\sigma_{i\eta i\eta}$ measures how broadly the energy is spread along η in the 5×5 crystal cluster around the crystal that seeds the supercluster. Since the trajectory in η of a photon is not affected by the magnetic field, its magnitude in η should be small, while for a π^0 it will tend to be larger [82].

Hadronic over electromagnetic energy ratio (H/E) the ratio of the energy deposited in the HCAL to the energy deposited in the ECAL within a cone of $\Delta R = 0.15$ around the ECAL supercluster, referred to as H/E, where $\Delta R = \sqrt{(\Delta\phi)^2 + (\Delta\eta)^2}$ is defined relative to the center of ECAL supercluster and the azimuthal angle ϕ is measured in the plane perpendicular to the beam axis. For photons this ratio should be low, while for jets, which carry both hadronic and electromagnetic energy, it will generally be higher.

Particle flow charged hadron isolation (I_{CH}): It is defined as the sum of p_{T} of all charged hadrons within a hollow cone of $0.02 < \Delta R < 0.3$ around the supercluster. As prompt photons are generally isolated, they should have a lower value of I_{CH}, while photons from fragmentation and decay processes will be generally accompanied by other charge particles, and hence a higher value of I_{CH}.

Particle flow neutral hadron isolation (I_{NH}): It is defined as the sum of p_{T} of all neutral hadrons within a cone of $\Delta R = 0.3$ around the supercluster. Like I_{CH}, it tends to have a lower value for prompt photons.

Particle flow photon isolation (I_{Ph}): It is defined as the sum of p_{T} of all photons within a cone of $\Delta R = 0.3$ excluding a strip in η of 0.015 about the supercluster. As with the other isolation variables, it's value is on average lower for isolated photons.

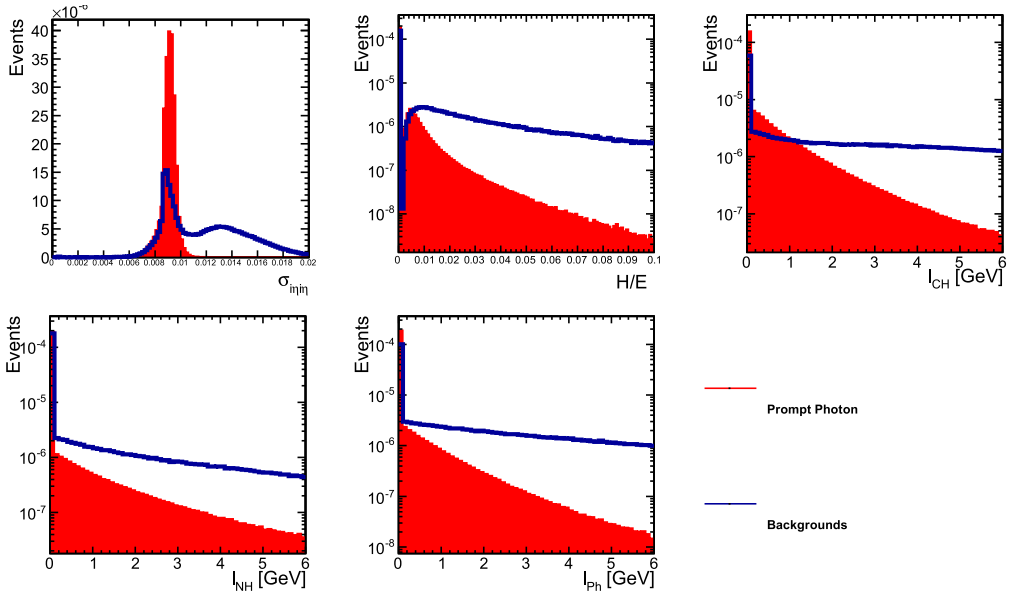

Figure 4.2: Distributions of variables which are used for photon identification. Red filled histogram shows the prompt photons distribution and blue histogram represents the backgrounds distribution.

The extra contribution coming from the overlapping proton-proton interactions (pileup) in the isolation region is estimated as $\rho \times EA$, where ρ is the median of the transverse energy density per unit area in the event [83] and EA is the effective area of the isolation region weighted by a factor that takes into account the dependence of the pileup transverse energy density on pseudorapidity (η). To reduce the dependence of the isolation variables on the number of pileup events, the extra contribution, calculated using ρ, is subtracted from the photon, charged hadron and

neutral hadron isolation sums. Figure 4.2 shows the distributions of $\sigma_{i\eta i\eta}$, H/E, and pileup corrected isolations (I_{CH}, I_{NH}, I_{Ph}) for prompt photons and backgrounds.

We consider three sets of selection criteria for the variables described above. The loose set of selections applies to analyses where the systematic uncertainty is dominant and backgrounds are rather low. This corresponds to relatively high signal efficiency (about 90%) and minimal impact to the systematics. The tight set of selections allows powerful background rejection without compromising dramatically the signal efficiency (about 70%). This selection is suitable for analyses with limited statistics and high background rates. The medium set of selections are in between loose and tight, corresponds to signal efficiency about 80% which is a good starting point for generic measurements .

The choice of prompt photon identification criteria is made with the optimized cut values of the variables. The optimized cuts for these variables are obtained by maximizing the significance ratio $S/\sqrt{S+B}$ in Monte Carlo simulation. A summary of the photon identification requirements for barrel region, are shown for three different working points in Table 4.2. Figures 4.3,4.4 and 4.5 show the signal and background efficiency of Photon ID for three different working points as a function of p_{T}, pileup and η respectively.

Working points(WP)	Loose	Medium	Tight
$\sigma_{i\eta i\eta}$	0.0102	0.0102	0.0100
H/E	0.5	0.5	0.5
I_{CH} [GeV]	3.32	1.37 GeV	0.76
I_{NH} [GeV]	$1.92 + 0.014 \times p_{\mathrm{T}}^{\gamma} + 0.000019 \times p_{\mathrm{T}}^{\gamma\,2}$	$1.06 + 0.014 \times p_{\mathrm{T}}^{\gamma} + 0.000019 \times p_{\mathrm{T}}^{\gamma\,2}$	$0.97 + 0.014 \times p_{\mathrm{T}}^{\gamma} + 0.000019 \times p_{\mathrm{T}}^{\gamma\,2}$
I_{Ph} [GeV]	$0.81 + 0.0053 \times p_{\mathrm{T}}^{\gamma}$	$0.28 + 0.0053 \times p_{\mathrm{T}}^{\gamma}$	$0.08 + 0.0053 \times p_{\mathrm{T}}^{\gamma}$

Table 4.2: Photon identification requirements for barrel for three working points [84]

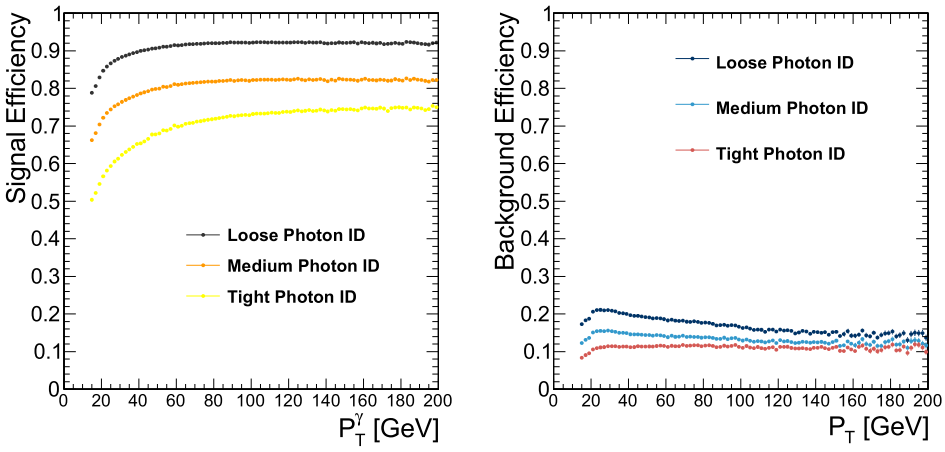

Figure 4.3: Signal efficiency (left) and background efficiency (right) of Photon ID for different working points as a function of p_{T} in the barrel region.

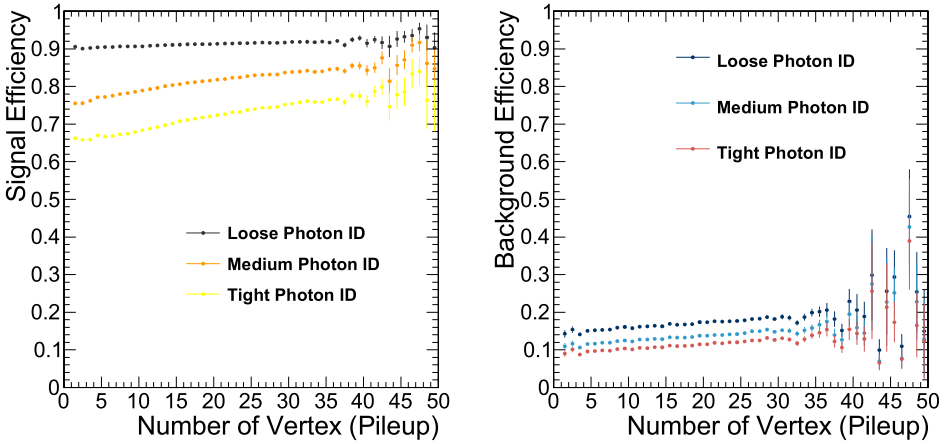

Figure 4.4: Signal efficiency (left) and background efficiency (right) of Photon ID for different working points as a function of number of vertices (pileup) in the barrel region.

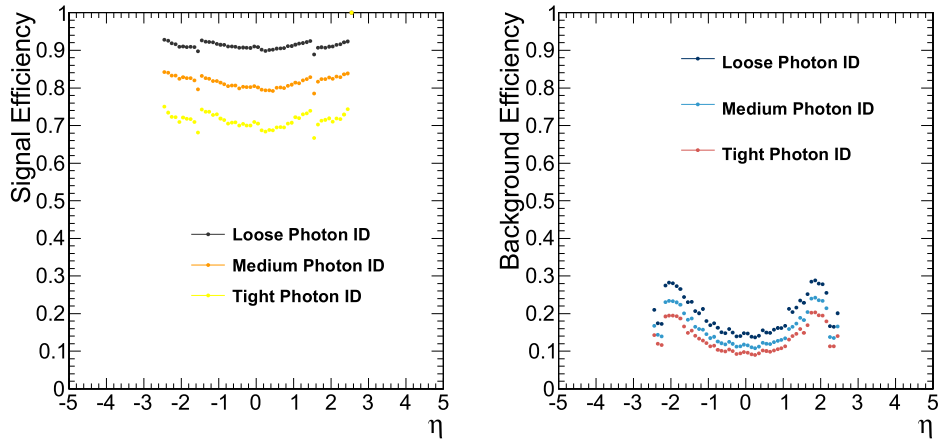

Figure 4.5: Signal efficiency (left) and background efficiency (right) of Photon ID for different working points as a function of η.

4.2 Missing Transverse Momentum

The p_{T}^{miss} in an event is calculated as the modulus of the vector component that balances the $\vec{p}_{\mathrm{T}}$ sum of all of the other components in the event ($\sum \vec{p}_{\mathrm{T}}$), it has a magnitude and a direction component. While the general definition is the same, there are multiple ways to reconstruct p_{T}^{miss} , and for this analysis the particle-flow MET algorithm [79, 85] is used, where MET and p_{T}^{miss} both stand for the same quantity: missing transverse momentum. The PF algorithm reconstructs all the particles in the event, and assigns the p_{T}^{miss} vector to be the negative of the vector sum over all particle-flow particles of their transverse momentum [79]. While the p_{T}^{miss} is reconstructed with fairly good accuracy [85], it is not possible to reconstruct the missing longitudinal energy because of the inherent uncertainty in the net longitudinal energy of the two quarks within the proton bunches that produce the event of interest.

The event $\sum \vec{p}_{\mathrm{T}}$ reconstruction, which leads directly to the PF p_{T}^{miss} assignment, is tested with samples of MinBias and QCD multijet events. These events are expected to be momentum-balanced in the plane transverse to the beam axis and have minimal

p_{T}^{miss}, if any. Reconstructing events that should already be balance in $\sum \vec{p}_{\mathrm{T}}$ allows for the fine-tuning of calorimeter noise cleaning, which removes anomalous signals due to electronics in the ECAL and HCAL, and indicates how well p_{T}^{miss} is reconstructed. When run on simulated events, the PF algorithm correctly reconstructs 80% of the true $\sum \vec{p}_{\mathrm{T}}$ [85].

Due to a wide variety of effects including the nonlinear response of the calorimeters, inefficiencies, and minimum energy thresholds of the various CMS sub-detectors, the magnitude of the p_{T}^{miss} can be underestimated or overestimated. Therefore, several corrections are applied to the p_{T}^{miss} measurement. The most important correction to the p_{T}^{miss} is the so called Type-I corrections. This correction is applied on the p_{T}^{miss} to adjust the energies of the jets in the event that have p_{T} above some threshold. Furthermore, special filters have been developed in order to filter events with not reliable p_{T}^{miss}. Multiple effects can lead to an unreliable measurement of p_{T}^{miss} and the corresponding filters are discussed below:

- CSC beam halo filter: rejects events with a secondary particle shower produced due to collisions of the beam with residual gas inside the LHC vacuum chamber.
- HBHE noise filter: removes events with noise in the hybrid photo-diodes (HPDs), used to convert the scintillator light into an electrical output and the readout boxes (RBXs) which contain them.
- ECAL dead cell trigger primitive (TP) filter: rejects events where the transverse energies of TP's at the masked crystal cells exceed 63.75 GeV
- HCAL laser filter: rejects events when firing of the HCAL laser overlaps with an LHC bunch crossing.
- Tracking failure filter: rejects events where standard or large calorimeter deposits contrast with a lack of reconstructed tracks.

- Bad EE Supercrystal filter: removes events from two 55 crystals that give anomalously high energy.

- Tracking POG filters: rejects events where no tracks are reconstructed due to aborting of the reconstruction algorithm because of CPU time limitations.

CHAPTER 5

Search for physics beyond standard model with 2016 data

The final states of particle collisions with a high-energy photon (γ) and large missing transverse momentum (p_{T}^{miss}) is an effective probe into new physics phenomena, such as production of gravitons under models with large extra dimensions discussed in section 2.2.2 or of dark matter particles discussed in section 2.2.1. This chapter describes a search for new physics in events with a monophoton signature, i.e., one high p_{T} photon and large p_{T}^{miss}, using pp collision data at $\sqrt{s} = 13$TeV collected by the CMS experiment in 2016.

Once the collision information gathered by CMS is recorded and reconstructed, several steps are taken to whittle the dataset down to a sample only containing events with a high p_{T} photon and p_{T}^{miss}. The data samples in CMS are organized in sets of events that meet a particular trigger selection criteria, thus providing the first level of event selection. The next step in the analysis is to select events that contain an energy deposition indicative of a well-defined photon with large transverse momentum.

In the standard model (SM), the only process that results in a genuine signature of

single photon and large p_{T}^{miss} is the $Z + \gamma$ production, where the Z boson decays into a neutrino(ν) and an antineutrino($\bar{\nu}$). The rate of $Z + \gamma$ production can be precisely calculable under the SM, and therefore a deviation of the observation from the prediction in this signature is a robust indication of the physics beyond the standard model. In reality, multiple other collision and non-collision processes mimic the signature and thus constitute additional background of the search. The analysis employs a series of event selections that is aimed at reducing the contributions from such non - $Z + \gamma$ backgrounds. Number of residual background events is then estimated by data-driven techniques and Monte Carlo (MC) simulations.

5.1 Datasets

5.1.1 Data samples

The data sample used in this analysis corresponds to an integrated luminosity of 12.9 fb^{-1}recorded with the CMS detector at center-of-mass energy of 13 TeV in the year 2016. A full list of the data sets used can be found in Table 5.1.

Data Samples
/SinglePhoton/Run2016*-PromptReco-v2/(MINI)AOD
/SingleElectron/Run2016*-PromptReco-v2/(MINI)AOD
/SingleMuon/Run2016*-PromptReco-v2/(MINI)AOD
/JetHT/Run2015*-PromptReco-v2/(MINI)AOD

Table 5.1: List of data sets used in this analysis.

Candidate events are selected out of the SinglePhoton data set, while the remaining three data sets are used for various control regions study and efficiency measurements.

5.1.2 Monte Carlo samples

Monte Carlo (MC) event generators are used to simulate signal and background samples in order to optimize the event selection, evaluate efficiencies and systematic uncertainties, and compute expected yields. A detailed list of the simulated samples used for signal and background processes is shown in Tab. 5.2.

For the SM backgrounds, the primary hard interaction is simulated using the MADGRAPH5 aMC@NLO version 2.2.2 [86] or PYTHIA8.212 [87] generators employing the NNPDF3.0 [88] leading-order (LO) parton distribution function(PDF) set at the strong coupling value $\alpha_S = 0.130$. Parton showering and hadronization are provided in PYTHIA8.212 through the underlying-event tune CUETP8M1 [89]. Multiple minimum-bias events are overlaid on the primary interaction to model the distribution of pileup in data. Generated particles are processed through the full GEANT4-based simulation of the CMS detector [90].

Process	Sample Name
Dark Matter	DarkMatter_MonoPhoton_*_13TeV-madgraph/[Spring16]-v*/RAWAODSIM
$Z(\to \nu\nu) + \gamma$	ZNuNuGJets_MonoPhoton_PtG-130_TuneCUETP8M1_13TeV-madgraph/[Spring16]-v1/RAWAODSIM
$Z(\to \ell\ell) + \gamma$	ZLLGJets_MonoPhoton_PtG-130_TuneCUETP8M1_13TeV-madgraph/[Spring16]-v1/AODSIM
$W(\to \ell\nu) + \gamma$	WGJets_MonoPhoton_PtG-130_TuneCUETP8M1_13TeV-madgraph/[Spring16]-v1/AODSIM
$W(\to e\nu)$	WToENu_M-100_TuneCUETP8M1_13TeV-pythia8/[Spring16]-v2/AODSIM
$W(\to \mu\nu)$	WToMuNu_M-100_TuneCUETP8M1_13TeV-pythia8/[Spring16]-v1/AODSIM
$W(\to \tau\nu)$	WToTauNu_M-100_TuneCUETP8M1_13TeV-pythia8-tauola/[Spring16]-v2/AODSIM
γ + jets	GJets_HT-_TuneCUETP8M1_13TeV-madgraphMLM-pythia8/[Spring16]-v*/AODSIM
$t\bar{t} + \gamma$	TTGJets_TuneCUETP8M1_13TeV-amcatnloFXFX-madspin-pythia8/[Spring16]-v1/AODSIM
QCD	QCD_Pt_EMEnriched_TuneCUETP8M1_13TeV_pythia8/[Spring16]-v/AODSIM

Table 5.2: List of the simulated samples used for signal and background processes.

For the DM signal hypothesis, MC simulation samples are produced requiring $p_{\mathrm{T}}^{\gamma} > 130$ GeV and $|\eta^{\gamma}| < 2.5$. A large number of DM simplified model samples are generated, varying the masses of the mediator and DM particles. Similarly, electroweak-DM effective interaction samples are generated with a range of dark matter masses. For the ADD hypothesis, events are generated using PYTHIA8.212, requiring $p_{\mathrm{T}}^{\gamma} > 130$ GeV, with no restriction on the photon pseudorapidity. Samples are prepared in a grid of number of extra dimensions and MD. The efficiency of the full event

selection on these signal models ranges between 0.12 and 0.27 for the DM simplified models, 0.42 and 0.45 for electroweak DM production, and 0.22 and 0.28 for the ADD model, depending on the parameters of the models.

The background processes listed in 5.2 could mimic the $\gamma + MET$ final state in the following ways:

- $Z(\rightarrow \nu\nu) + \gamma$ is the irreducible background as it has the same final state.
- $W(\rightarrow \ell\nu) + \gamma$ in which the charged lepton is lost or misreconstructed.
- Inclusive $W(\rightarrow \ell\nu)$ production where the lepton fakes a photon.
- $Z(\rightarrow \ell\ell) + \gamma$ in which both leptons are lost or misreconstructed.
- $t\bar{t} + \gamma$ where $t\bar{t}$ undergoes a (semi)leptonic decay, and the charged lepton is lost or misreconstructed.
- Other $\gamma + X$ events in which the $p_{\mathrm{T}}^{miss}$is mismeasured.

5.2 Triggers

The first major event selection relies on the L1 and HLT triggers. The kinematic measurements used for the triggers are less precise than their offline counterparts, so analyses usually employ triggers with lower thresholds and looser criteria than their offline counterparts to significantly reduce the sample of possible events. Triggers with lower thresholds have higher frequencies, but the physical limitations of the detector constrain the rate at which can be recorded. To solve this problem, the lower threshold triggers are prescaled so that only a fraction of the events that pass are actually kept. In this analysis, the signal sample is reduced from the entire set of Photon data sets to only include events that have passed a single-photon trigger HLT_Photon165_HE10 which requires at least one photon candidate with $p_{\mathrm{T}} > 165$

GeV and the photon candidate must have H/E (described in section 4.1.2) less than 0.1. The relative trigger efficiency of the HLT_Photon165_HE10 single-photon trigger is shown in Figure 5.1. To measure the efficiency, we select events passing prescaled triggers with lower p_{T} thresholds (75, 90, and 120 GeV respectively). We apply medium photon identification requirements (discussed in section 4.1.2) on the events firing the low thresholds triggers, and compute the rate at which such events have also fired the main analysis trigger. One can see that the trigger become fully efficient ($> 98\%$) above 175 GeV.

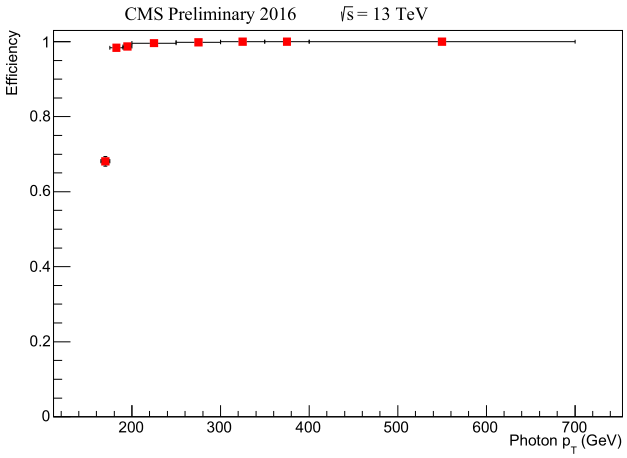

Figure 5.1: Relative trigger efficiency for the single-photon trigger HLT_Photon165_HE10 as a function of offline photon candidate transverse momentum.

5.3 Event Selection

Events for this analysis should have one high p_{T} photon in the final state. To select such events in data, we require the events to pass the trigger discussed above. The events are required to have at least one good primary vertex (PV) fullfilling the following criteria:

1. it has a position along the beam line ($z-$axis) within ± 24 cm of the nominal

CMS detector center;

2. the distance in the transverse plane from the nominal beam line within 2 cm; and

3. NDOF > 4, where NDOF is the number of degrees of freedom and is calculated by the number and compatibility of nearby tracks [91].

The majority of the requirements focus on the photon candidate. After selecting a good vertex, we require at least one photon object with $p_{\mathrm{T}}^{\gamma} > 175$ GeV in the fiducial region of the ECAL barrel ($|\eta| < 1.44$). The choice of using only the barrel photons is based on two considerations. The first is that the signal events tend to produce more central photons than forward ones, as demonstrated in Figure 5.2. The second point is that, as described in detail in Sec. 5.4.5, the default method of estimating the beam halo background breaks down for endcap photons.

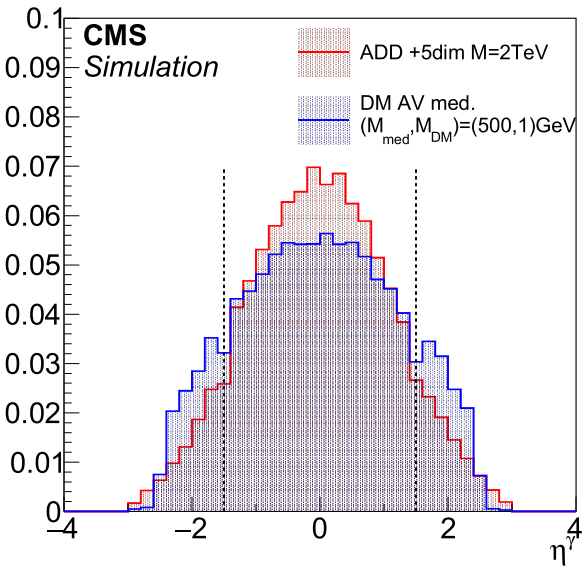

Figure 5.2: η distributions of photons from two signal model points [92].

Two of the background sources to single-photon event selection are the misidentification of jets and electrons as photons. A jet can be misidentified as a photon when

a neutral particle such as π^0 (or η, ρ) within the jet carries a significant fraction of the p_{T} and the photons from its subsequent decay are collimated such that they appear as a single photon in ECAL. Electrons may be misreconstructed as photons due to inefficiency in the track reconstruction. To minimize these contributions, we require the photon should fulfil the medium photon identification criteria (medium photon ID) discussed in section 4.1.2.

The PF-based charged isolation of the photon is computed using the primary vertex (PV), because the high-E_{T} photon we consider is assumed to emerge from the hard scattering at the PV. The PV is the vertex with the highest $\sum p_T^2$. The actual rate that the photon comes from the PV depends on the pileup activity in the event. For a $\gamma + p_{\mathrm{T}}^{miss}$ final state in a high pileup environment, a significant fraction of the event may have the photon not originating from the PV, because it is often the case that the hard-scattering vertex has little charged track activity. Misassignment of the photon vertex leads to an artificially smaller value of isolation. Thus, an additional PF-based charged isolation is computed in the same manner and with same cone size, but with respect to all vertices in the event. The largest of such isolation sums namely PFWorst Charged Hadron Isolation (I_{WCH}), ensures that the photon object in an event is isolated from charged hadron activity even in the event that the candidate is matched to the wrong primary vertex. Naively, one can simply replace I_{CH} with I_{WCH} in the event selection.

Photons can be mimicked by muons in the beam halo or in cosmic rays that can induce bremsstrahlung and produce showers in the ECAL, but these contributions are reduced using the seed crystal time and MIP total energy information. The way is to compare the timing of the seed crystal, defined as the crystal with the highest energy deposition within the supercluster, to the timing of the event to make sure the deposition is consistent with a collision. The event is kept if the seed crystal of the photon supercluster is deposited within $\pm$3ns of the time expected for particles

from a collision. MIP total energy is computed by summing up additional ECAL energy deposits consistent with potential paths of the beam halo minimum-ionizing particle (MIP) that penetrates the ECAL and the MIP total energy is required to be less than 4.9GeV for a photon candidate. Both types of informations are also reduced by rejecting events if a CosmicMuon is reconstructed in the muon detectors, which is defined a muon that is reconstructed from individual muon system segments that align to project back to the collision point. These non-projective muons could be from the beam halo or cosmic rays. Beam halo is discussed in some detail in section 5.4.5.

Requirements are also placed on the spatial, deposition time, and energy distribution within a supercluster defining a photon candidate. Collision event data from CMS are subject to spurious high-energy signals from single crystals embedded within EM showers in the ECAL, but these signals can be identified by their spike-like energy distribution within the shower, and by their spike-like energy and spatial distributions when they appear outside of a real EM shower. This instrumental background contribution is reduced in several ways. The shower shape of the photon candidate must fulfill minimum spatial requirements $\sigma_{i\eta i\eta} > 0.001$ and $\sigma_{i\phi i\phi} > 0.001$, where $\sigma_{i\phi i\phi}$ is calculated in $i\phi$-space in a manner similar to $\sigma_{i\eta i\eta}$ as discussed in section 4.1.2. A limit is also placed on the variation between deposition times within a cluster: the largest intracluster time difference (LICTD) between crystals with more than 1 GeV of deposited energy must be within ±5ns. To further reduce the number of events with electrons misidentified as photons, the photon candidate is required not to have an associate pixel seed.

The missing transverse momentum present in the event is computed as the negative sum of the transverse momentum of all particle flow candidates in the event, and is computed using a particle-flow algorithm [79]. Events are required to have $p_{\mathrm{T}}^{miss} >$ 170GeV. Because the photon candidate is expected to be recoiling against the

missing new physics particle in the signal events, p_{T}^{miss} and photon are required to be separated by more than 2 radians in the azimuthal angle. p_{T}^{miss} threshold of 170GeV is derived using an ADD signal model point by maximizing the ratio of the signal yield to the square root of the expected background.

To reduce the SM backgrounds arising from the leptonic decays of W($l\nu$) and Z(ll) bosons, a lepton veto is applied. Events are rejected if they have at least one electron or muon fulfilling loose cut based identification requirement [93, 94]. Events with electrons or muons with $p_{\mathrm{T}} > 10$GeV that are farther away from the candidate photon by $\Delta R > 0.5$ are vetoed to minimize the contribution from W($l\nu$) + γ and Z(ll) + γ process.

Also a limit is placed on the amount of hadronic activity surrounding the photon candidate. This minimizes the contribution from W+jet, γ+jet, and other events which can include a high energy photon candidate and missing energy along with jet activity. An event is vetoed if it contains a jet with $p_{\mathrm{T}} > 20$GeV and $|\eta| < 5.0$ that is located $\Delta R > 0.4$ away from the photon candidate.

An event is rejected if the azimuthal opening angle between the p_{T}^{miss} and the closest jet ($min\Delta\phi(pt_T^{jet}, p_{\mathrm{T}}^{miss})$) is less than 0.5 radians. Only up to four leading jets are considered in $min\Delta\phi(pt_T^{jet}, p_{\mathrm{T}}^{miss})$. This requirement is highly efficient in reducing the γ + jets background.

5.4 Background estimation

5.4.1 Overview

As mentioned earlier in this chapter, there are multiple distinct sources of SM background to this analysis. The most significant of them is the so-called irreducible background, which is the production of a Z boson in association with a high-energy

photon ($Z(\nu\bar{\nu}) + \gamma$) where the Z boson decays into a neutrino-antineutrino pair. The second largest background comes from events with $W(l\nu) + \gamma$ (where $l = e, \mu$) final states, where W boson decays leptonically. A large fraction of such events are rejected by the electron and muon vetoes in the event selection. However, hadronic tau events and events where the leptons are out of the reconstruction acceptance will remain, and the vetoes themselves have imperfect efficiencies. These two background sources are estimated using MC simulations.

We also consider $Z \to \ell\ell + \gamma$, $t\bar{t} + \gamma$, and $W \to \mu\nu$ with a strong collinear radiation from the muon. These processes, collectively denoted as minor SM backgrounds, can contribute in the signal region if the leptons go out of acceptance or are not captured by the veto. The effective rate of such processes are much smaller than $Z + \gamma$ and $W + \gamma$. MC simulations are also used to predict their contribution.

Less significant but non-negligible background arise from events where the candidate photon object is a misidentified electron or electromagnetic shower caused by hadrons. Such misidentifications are rare, but the processes with final states that are prone to misidentification have high cross sections. The background events from electron misidentification are mostly W boson production ($W \to e\nu$), whereas those from hadron misidentification can be due to multiple sources such as $Z(\to \nu\nu)+$jets and QCD multijet with grossly mismeasured jet energy. Since object misidentification rates depend on subtle details of the detector, MC simulation cannot be expected to model it reliably. Therefore, data-driven techniques are employed to estimate the contributions from these background events.

Jet energy mismeasurement can also make $\gamma+$jets events appear to have large p_{T}^{miss}. However, p_{T}^{miss} typically aligns with one of the jets in such cases, and therefore the requirement that p_{T}^{miss} be separated from jets in the event reduces this background highly effectively. The residual of this background is estimated from MC.

Finally, large (real and spurious) energy deposits in ECAL from non-collision pro-

cesses can mimic $\gamma+p_{\mathrm{T}}^{miss}$ events and therefore need to be controlled. Known sources of such background include bremsstrahlung of beam halo or cosmic ray muons and noise in the ECAL photodetectors and electronics. Data-driven estimations based on the pulse time of the seed ECAL hit and the azimuthal angle distribution of the showers are employed to estimate the contributions from these non-collision background events.

5.4.2 $Z\gamma$ and $W\gamma$

$Z + \gamma$ and $W + \gamma$ background contributions are modeled and estimated using MC simulations. Samples generated at leading order (LO) in QCD by MADGRAPH 5 with up to two additional partons and a generator-level requirement of $p_{\mathrm{T}}^{\gamma} > 130\mathrm{GeV}$ are employed.

Subprocess	$A \times \epsilon$ (%)
$W \to e\nu + \gamma$	0.105
$\lvert\eta^{e}\rvert < 2.5$	0.083
$\lvert\eta^{e}\rvert > 2.5$	0.022
$W \to \mu\nu + \gamma$	0.121
$\lvert\eta^{\mu}\rvert < 2.5$	0.048
$\lvert\eta^{\mu}\rvert > 2.5$	0.073
$W \to \tau\nu + \gamma$	0.291

Table 5.3: The breakdown of simulated $W + \gamma$ events in the signal region. Events are categorized in the W decay mode. Events with $e\nu$ and $\mu\nu$ final states are further divided into those where the lepton was roughly within acceptance ($|\eta| < 2.5$) but failed the lepton veto, and those where the lepton was out of acceptance ($|\eta| > 2.5$). For each W decay mode, the fraction out of total generated ($A \times \epsilon$) is shown.

Table 5.3 gives the breakdown of the multiple ways the $W + \gamma$ process can become a background. Event counts are obtained using the parton-level information. From this breakdown, one can see that events where the W boson decays to a τ and a neutrino constitutes half of the $W + \gamma$ background. Also evident is the difference in the composition of electron and muon events. Identification efficiency is lower for

electrons than for muons, which contribute to the large in-acceptance background from the electron channel. On the other hand, the fraction of events where the lepton is out of acceptance should be nearly identical between the electron and muon channels. However, a large fraction of electrons that are out of tracker acceptance are still captured by the calorimeters, leading to lower p_{T}^{miss} and thus smaller background contribution.

To correct the overall normalization, the samples are scaled to the corresponding next-to-next-to leading order (NNLO) cross sections calculated by Grazzini et al. [95] for $p_{\mathrm{T}}^{\gamma} > 175\mathrm{GeV}$ and $|\eta^{\gamma}| < 1.4442$. For the $Z + \gamma$ sample, the differential cross section $d\sigma/dp_{\mathrm{T}}^{\gamma}$ was made available, which enables the correction also of the slight discrepancy in the p_{T}^{γ} spectrum between the LO and the higher order calculations. The cross section values are summarized in Tab. 5.4.

p_{T}^{γ}range (GeV)	σ (fb)	NNLO / LO
$Z + \gamma$		
[175, 190]	14.4	1.39
[190, 250]	29.7	1.35
[250, 400]	17.5	1.30
[400, 700]	3.7	1.23
[700, inf]	0.3	1.23
$W + \gamma$		
[175, inf]	243.9	1.34

Table 5.4: Cross sections used to normalize the $Z + \gamma$ and $W + \gamma$ samples.

Additionally, to account for rate suppression due to higher-order electroweak effects at high vector boson p_{T}, correction factors taken from Refs. [96] and [97] (Figure 5.3) are applied to these samples as a function of photon p_{T}.

Different sources of systematic uncertainty are considered for estimating $Z + \gamma$ and $W + \gamma$ events and the systematic uncertainties are discussed in section 5.5.

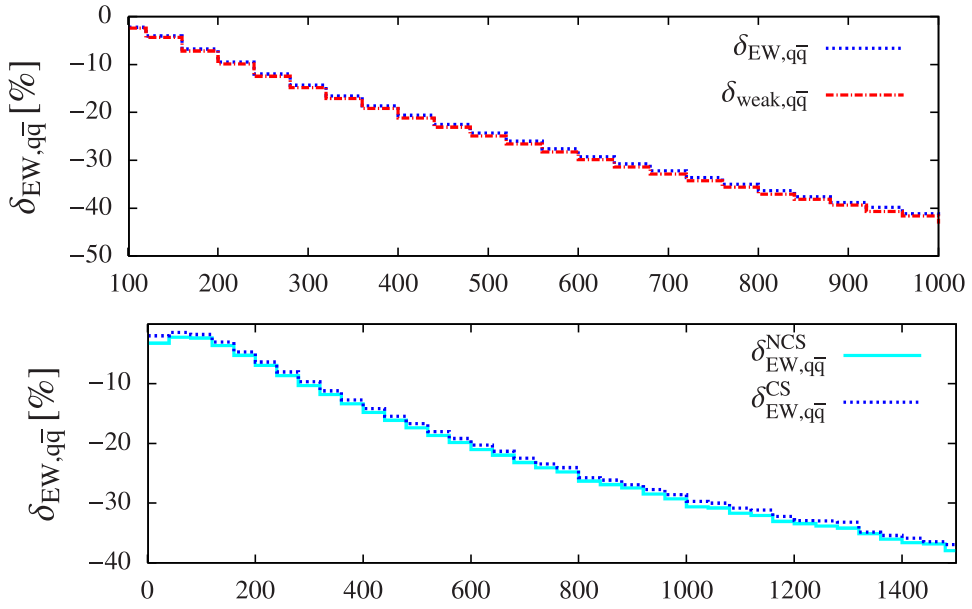

Figure 5.3: Electroweak NLO cross section corrections as a function of photon p_T for $Z + \gamma$ (top) and $W + \gamma$ (bottom) processes. Reprinted from Refs. [96] and [97].

5.4.3 Electron misidentification

An important background consists of $W \to e\nu$ events in which the electron is misidentified as a photon. The misidentification occurs because of inefficiency in seeding electron tracks. A seeding efficiency of $\epsilon_e^{pixel} = 0.977 \pm 0.002$ for electrons with $p_T > 160$ GeV is measured in data using a tag-and-probe technique in $Z \to ee$ events, and is verified with MC simulation. Misidentified electron events are modeled by a proxy sample of electron events, defined in data by requiring an ECAL cluster with a pixel seed. The proxy events must otherwise pass the same criteria used to select signal candidate events. The number of electron proxy events is then scaled by $R_e = (1 - \epsilon_e^{pixel})/\epsilon_e^{pixel}$ to estimate the contribution of events from electron misidentification. The dominant uncertainty in this estimate is the statistical uncertainty in the measurement of ϵ_e^{pixel}.

The factor R_e is estimated using "tag-and-probe" (TP) method by exploiting the Z boson decay into an e^+e^- pair. In this TP method, a high-quality electron object

(tag) is identified from a single-electron data sample, and the accompanying electron is selected from the pool of elecromagnetic objects (probes) in the event. The probes must pass the medium photon identification criteria. The area of the peak in the mass distribution of the tag-probe system around the Z boson mass is then measured once applying the pixel-seed veto requirement on the probe ($Z \to e\gamma$ sample) and once inverting the veto ($Z \to ee$ sample). Denoting the two areas $N^{e\gamma}$ and N^{ee}, respectively, the ratio $N^{e\gamma}/N^{ee}$ is equal to R_e up to minor systematic corrections.

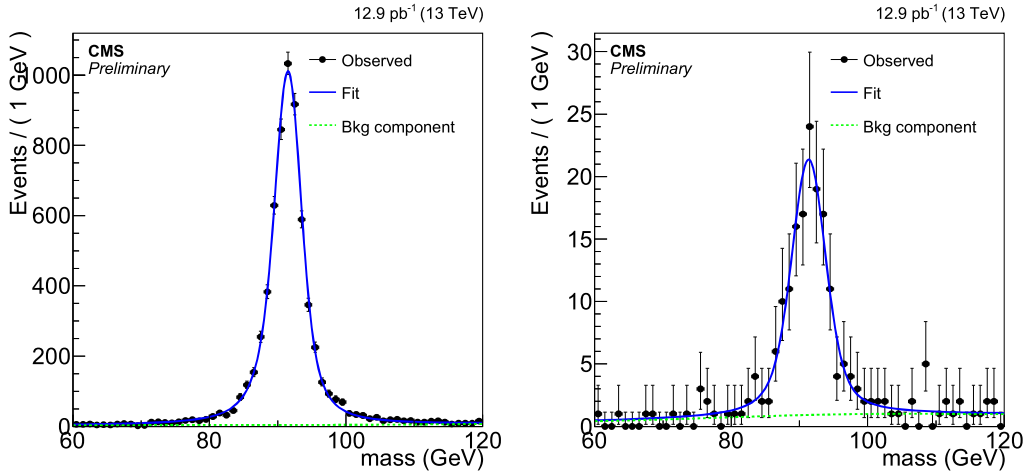

Figure 5.4: Fits to the mass distributions for ee (left) and $e\gamma$ (right) selections. The blue solid line represents the full fit model, and the green dashed line its background component.

The TP mass distributions are fitted to extract $N^{e\gamma}$ and N^{ee}. The fit model is composed of two templates, where one template describes a pure $Z \to ee$ (signal) line shape and the other describes the background contributions. The backgrounds to the ee fit include W + jets, diboson, and $t\bar{t}$ productions, which are all negligible and estimated to contribute less than 1%. The backgrounds to the $e\gamma$ fit on the other hand mainly consist of processes with actual electron and photon in the final state, such as $W\gamma$ and $Z \to ee$ with a hard radiation off one of the electrons. Minor contributions from processes that do not involve true electrons, such as diphoton production with a strongly asymmetric conversion on one of the photons and

misidentification of a QCD jet as an electron, are predicted to be negligible from MC studies. Breit-Wigner function convoluted with Crystal Ball function is used for fitting signal distribution and RooCMSShape (a product of error function and exponential function) is used to fit background distribution. The fits for the $Z \to ee$ and $Z \to e\gamma$ cases can be seen in Figure 5.4. For calculating N^{ee} and $N^{e\gamma}$, the integral value of mass window between 81GeV and 101GeV is considered and we obtain $R_e = 0.0239 \pm 0.0016(\text{stat.}) \pm 0.0012(\text{syst.})$ for probe $p_{\text{T}} > 160$ GeV. This result is then translated to yield an estimated contribution of 52.7 ± 4.2 events from electron misidentification.

5.4.4 Hadron misidentification

Any analysis involving photons in final state is always subject to fake photons from QCD multi-jet events. Specifically, these fakes occur when one of the high p_{T} jets fragments into an isolated π^0or η which is sufficiently collimated to appear as a single electromagnetic shower in the ECAL detector.

The fraction of hadronic activity from QCD which will pass the photon isolation selection requirements is small but the QCD production is large, so the overall production rate for fake photons coming from QCD is potentially large. This background is difficult to simulate using Monte Carlo (MC) techniques due to the cross section and fragmentation uncertainties as well as the large statistics requirement. We therefore use a data-driven approach. We select a sample of fake photons using a selection that is similar to that used for candidate events and apply the fake ratio to provide a normalized estimate of the jet faking photon background. An advantage of such a data driven technique is that the (mis)modelling of effects such as pileup and fragmentation in simulation enters into the calculation only via the photon signal template where the effects are expected to be minimal.

For a realistic estimation of the fake ratio we use the shower shape properties of photons in the ECAL from data. A data control sample of $p_{\mathrm{T}}^{miss} < 30$ GeVwhich is well separated from the signal region and is dominated by QCD multi-jet events is employed. The fake ratio is the ratio of the number of events estimated as coming from QCD jets but passing the photon selection criteria used in candidate selection compared to the number of events containing a jet that can give rise to a fake photon object. The numerator in this ratio is calculated as the number of events that contain a photon which satisfies the medium photon ID criteria. The denominator is the number of events conatining a photon which fails the loose photon ID criteria, but passes a very loose selection. Both the numerator and denominator have in addition to the $p_{\mathrm{T}}^{miss} < 30$ requirement, selections to mitigate the effects of noncollision backgrounds and beam halo effects. The selections for the numerator and denominator are summarized in Tables 5.5 and 5.6 respectively.

Numerator Selections

photon ID	I_{NH}	$< 1.06 + 0.014 p_T^\gamma + 0.000019 (p_T^\gamma)^2$ [GeV]
	I_{Ph}	$< 0.28 + 0.0053 p_T^\gamma$ [GeV]
	I_{CH}	< 1.37 [GeV]
	H/E	< 0.05
	hasPixelSeed	False
QCD	p_{T}^{miss}	< 30 [GeV]
noncoll	$\sigma^\gamma_{i\eta i\eta}$	> 0.001
	$\sigma^\gamma_{i\phi i\phi}$	> 0.001
	$\mathrm{MIP}^{E_{tot}}$	< 4.9 [GeV]
	$\lvert t^\gamma_{\mathrm{seed}} \rvert$	< 3 [ns]

Table 5.5: Requirements for events passing the numerator selections. Events must pass the medium photon ID criteria.

The control sample where we measure the fake ratio has a considerable fraction of true isolated photons from inclusive QCD direct photon production processes. This contribution is estimated and the numerator of the raw fake ratio is scaled to reflect only the QCD component. We use the $\sigma_{i\eta i\eta}$templates from $\gamma + jet$ Monte Carlo to determine the fraction of true photons using the templates fitting facility

Denominator Selections

photon ID	Fail One	I_{NH}	$< 1.92 + 0.014 p_T^\gamma + 0.000019 (p_T^\gamma)^2$ [GeV]
		I_{Ph}	$< 0.81 + 0.0053 p_T^\gamma$ [GeV]
		I_{CH}	< 3.32 [GeV]
	Pass All	I_{NH}	$< \text{Min}(0.2 p_T^\gamma, 5 \times [1.92 + 0.014 p_T^\gamma + 0.000019 (p_T^\gamma)^2])$ [GeV]
		I_{Ph}	$< \text{Min}(0.2 p_T^\gamma, 5 \times [0.81 + 0.0053 p_T^\gamma])$ [GeV]
		I_{CH}	$< \text{Min}(0.2 p_T^\gamma, 5 \times 3.32)$ [GeV]
		H/E	< 0.05
		hasPixelSeed	False
QCD		p_{T}^{miss}	< 30 [GeV]
noncoll		$\sigma^\gamma_{i\eta i\eta}$	> 0.001
		$\sigma^\gamma_{i\phi i\phi}$	> 0.001
		$\text{MIP}^{E_{tot}}$	< 4.9 [GeV]
		$\lvert t^\gamma_{\text{seed}} \rvert$	< 3 [ns]

Table 5.6: Requirements for events passing the denominator selections. Events must fail at least one of the loose photon ID requirements but pass a very loose photon ID selection. The bounds for the very loose selection are 5 times those for the loose selection.

in ROOT [98]. The QCD templates are taken from data by choosing events within a side-band of charged hadron isolation (I_{CH}) defined as (7) GeV$< I_{CH} <$ (13) GeV. This side band is chosen such that the signal contamination in the backgorund template is small ($\sim$ 10%), with the upper bound set to maintain approximately one quarter of the data sample.

Figures 5.5 and 5.6 show the results of the templates fitting in various p_T bins. The estimated fractions are calculated within $\sigma_{i\eta i\eta} < 0.0102$ to match the photon candidate selection criteria used in this analysis. Figure 5.7 shows the final corrected fake ratio used in estimating the QCD background from data. The QCD estimate is made by selecting events which are identical in character to our candidate event sample but replacing the photon identification selection with the criteria from the denominator sample and applying the fake ratio as a function of p_T. This fake ratio is used to normalize a very small sample of events, which is representative of the small number of data QCD events which will share our candidate signal topology. The fake ratio is parametrized in the following form as a function of p_T^γ:

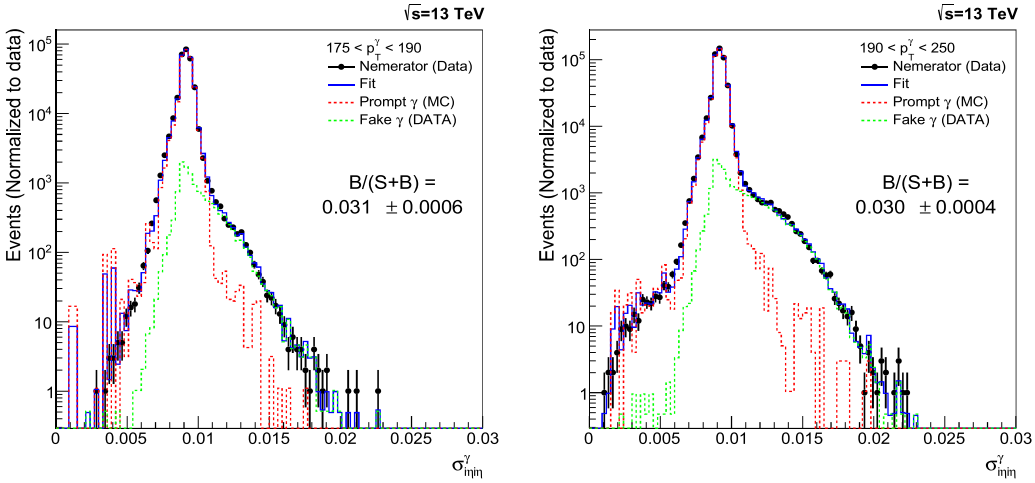

(a) p_{T}Bin 175-190 **(b)** p_{T}Bin 190-250

Figure 5.5: Template ($\sigma_{i\eta i\eta}$) distributions and fits to QCD and true photon components in p_{T}bins 175-190 GeV and 195-250 GeV.

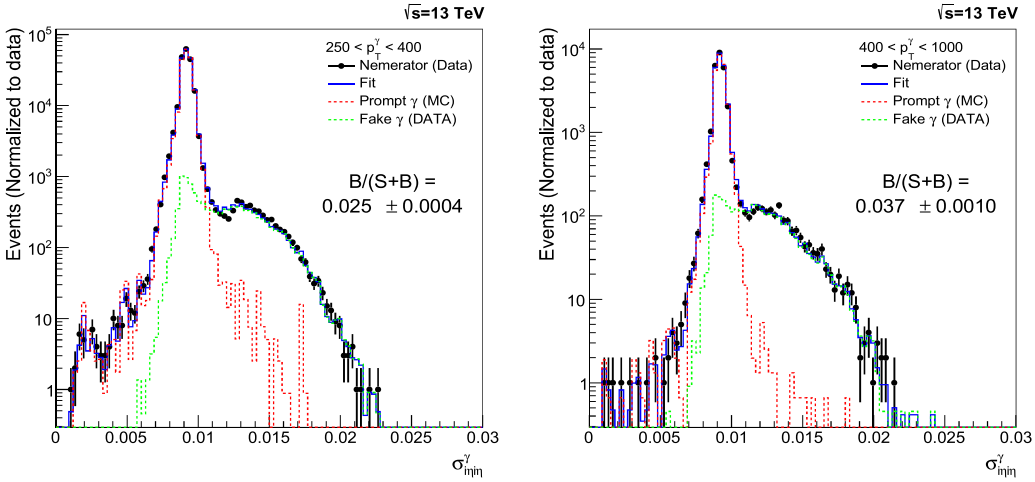

(a) p_T Bin 250-400 **(b)** p_T Bin 400-1000

Figure 5.6: Template ($\sigma_{i\eta i\eta}$) distributions and fits to QCD and true photon components in p_T bins 250-400 GeV and 400-1000 GeV.

$$f_{p_T^\gamma} = 0.028 + 0.0000002 \times p_T^\gamma \tag{5.1}$$

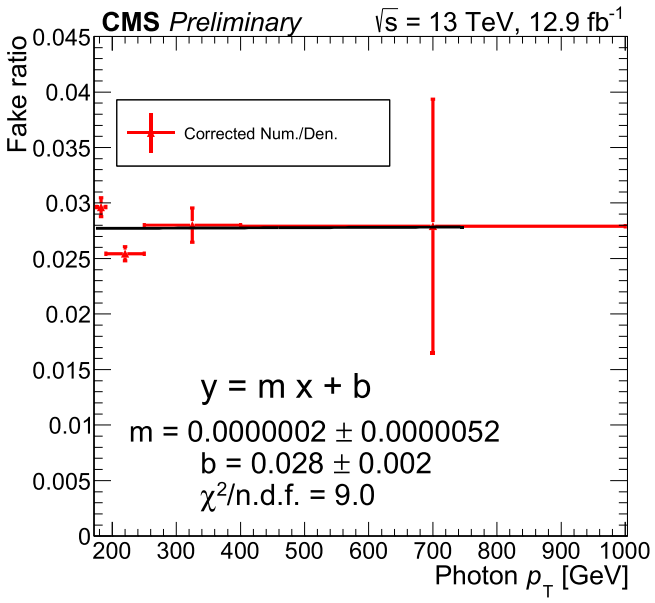

Figure 5.7: The corrected QCD fake rate as a function of p_T^γ.

The error on the estimated number is calculated by taking the largest of the uncertainties arising from the following sources:

- The uncertainty due to different choices of sideband region. We choose two cases where the upper boundary of side is varied by 2 GeV on either side of the nominal threshold used.
- Changing the definition of denominator by requiring only charged hadron OR neutral hadron isolation to fail.
- Varying the MET selection for control region by ±15 GeV.
- The bins size of shower shape templates. This is done by changing the bins size by 0.5 and 2.0 times the nominal bin width.
- The fake rate calculation is performed using a variation of one standard deviation from the fit.

The statistical uncertainty and side-band selection variation gives the maximum change in the fake ratio. Figure 5.8 summarizes the effect of these systematics on fake ratio. As a conservative approach, a total systematic uncertainty of 35% is used over the whole p_T range for fake ratio estimation and combined with statistical uncertainty. The estimated total number of events for jet misidentification background in the signal region is 5.85 ± 1.7 events.

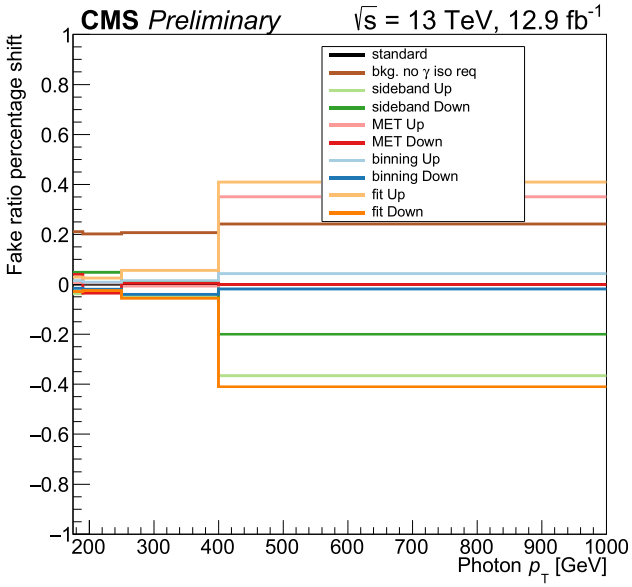

Figure 5.8: Change in fake ratio as a function of p_T^{γ} due to different sources.

5.4.5 Non-collision background

Non-collision background arise from multiple sources, with the only commonality being that they appear as an isolated high-p_{T} photon, often with very little activity in the event because coincidence with hard scatterings is rare, and consequently a large p_{T}^{miss} pointing away from the photon candidate. The known sources are:

- Beam halo

  Bremsstrahlung by the beam halo muon around the ECAL volume will generate an actual physical EM shower in the ECAL crystals. Large energy deposit

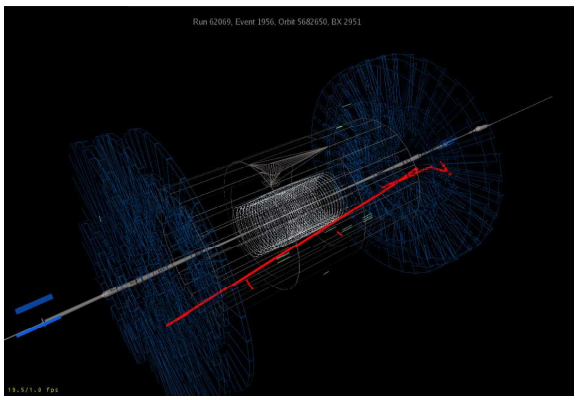

Figure 5.9: Halo muon from beam 2, travelling anticlockwise, detected passing through CMS.

is expected to be rare, but it is indicated that there the rate of beam halo penetration during the 2016 run was substantial. Figure 5.9 shows a beam halo event in the CMS detector. Characteristic feature of the shower caused by the halo particles include coincident hits in the barrel muon system and a "trail" of low-energy clusters in ECAL along the particle trajectory. The CSC beam halo filter described in Sec. 4.2 exploits the former, while the MIP total energy variable of the photon object captures the latter.

- Spikes

  Since 2010 it is known that the ECAL barrel avalanche photodiode (APD) can sporadically undergo a large discharge that correspond to up to several TeV of energy deposit. Figure 5.11 shows a spike event in the CMS detector. Unless the spike coincides with pileup or other form of genuine energy deposit in the crystal around the spiking APD, the resulting cluster will consist of a single crystal. Therefore the variable $S = (1 - E4/E1)$ (the "swiss cross" variable) can be used to efficiently reject such spurious clusters. Here, $E1$ is the energy of the seed crystal of the cluster, and $E4$ is the sum of energy of the four nearest neighbors of the seed. Typically, S is required to be less than 0.95.

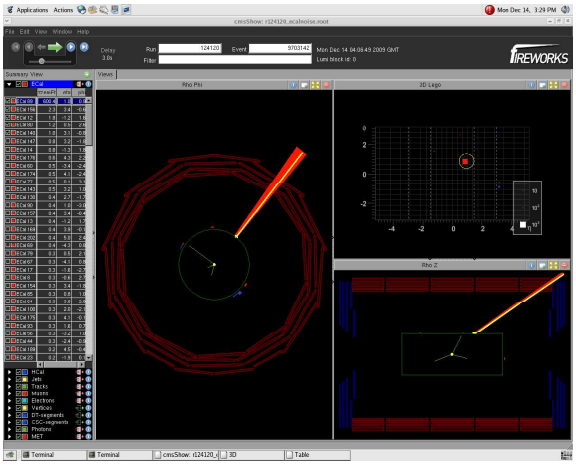

Figure 5.10: Anomalous signals in ECAL barrel lead to spike event in the CMS detector.

- Local noise

  Noise in the ECAL photodiodes or the electronics can also result in spurious clusters. Such clusters have similar characteristics as the spike signal, but are geographically localised to specific crystals. ECAL detector performance group (DPG) is regularly searching for noisy channels, and if found masking them from reconstruction. However there are fringe cases where the noise rate is not enough to be detected by the DPG but is sufficient to appear in the analysis candidate samples. No such case is observed in the 2016 data set so far.

The most significant local noise sources are eliminated by requiring $S < 0.95$ on the candidate photons. For the remaining two sources, it was observed in Run 1 that the clusters caused by beam halo and spikes have distinctive distributions of the seed crystal timing. Therefore, the first step in estimating the contribution of the non-collision background is to look at the full timing distribution of the candidate photons. Because the default supercluster reconstruction algorithm discards ECAL hits with $|t| > 3\,\text{ns}$, a full re-reconstruction of the 2016 data is performed removing this constraint.

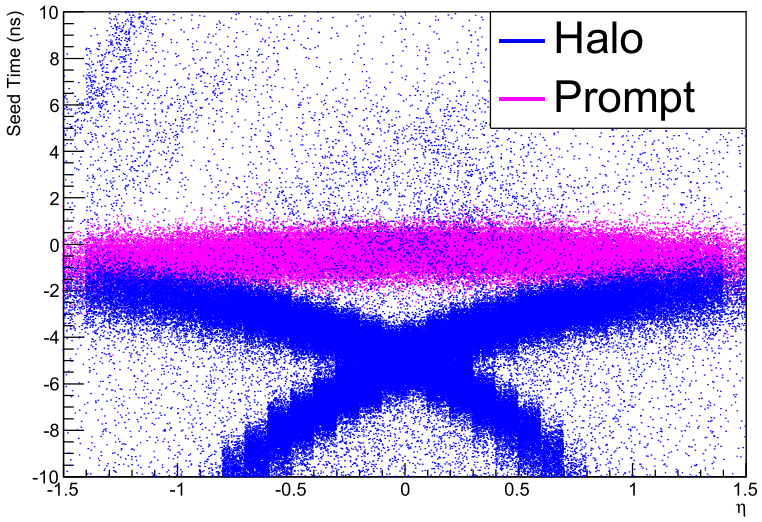

Figure 5.11: Super cluster η vs. seed-time. Prompt events arrive at the ECAL barrel at $t = 0$. Halo events primarily arrive out-of-time with respect to prompt events. The blue region show the expected arrival time for halo particles due to the path length difference to reach ECAL.

Figure 5.12 shows the timing distribution of barrel photon objects with $p_{\mathrm{T}} > 175$GeV and $\sigma_{i\eta i\eta} < 0.0102$ in events with $p_{\mathrm{T}}^{miss} > 170$GeV. This distribution, which obviously consists of at least two distinct populations, is fit with three templates: halo, and spikes, and prompt. The halo template is formed by photons with MIP total energy > 4.9GeV. The spike template comes from photons where one of the shower shape variables ($\sigma_{i\eta i\eta}$ or $\sigma_{i\phi i\phi}$) have nonphysically small values, i.e. , < 0.001. The prompt template, which represents the timing distribution of EM objects emerging from the pp collisions, is made using the candidate sample in which the photon candidates are required to have a pixel seed match. Such sample is dominated by $W \to e\nu$ events. The three templates and the candidate distribution are shown in Figure 5.13.

An alternative method like seed time template fitting, ϕ template fitting is used to estimate beam halo. Energy clusters in the ECAL due to beam halo muons are observed to concentrate around $\phi \sim 0$ and π, while all other processes (collision-

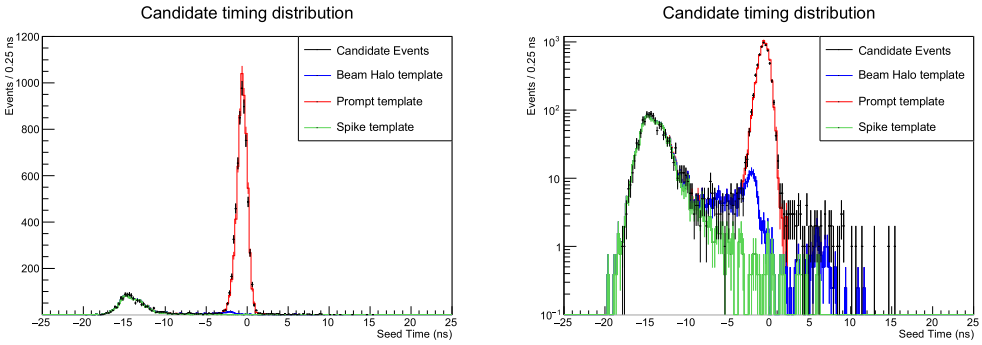

Figure 5.12: Timing distribution of candidate-like photons in events with $p_{\mathrm{T}}^{miss} >$ 170GeV obtained by full re-reconstruction of 2016 data in linear (left) and log (right) scale. The three templates used in the fit are in Figure 5.13.

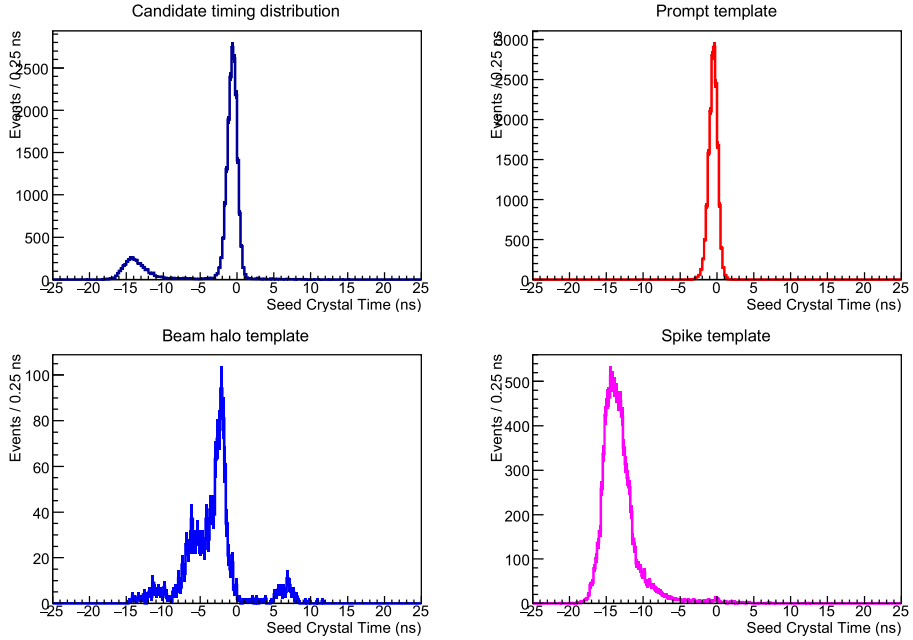

Figure 5.13: Timing distribution templates for candidate, prompt, halo, and spike candidates.

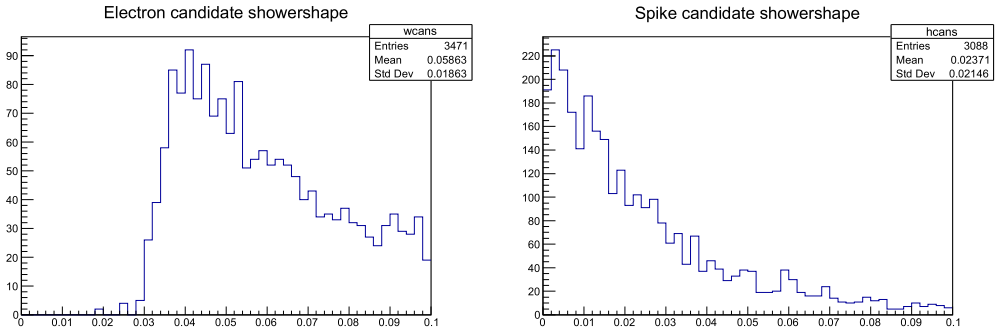

Figure 5.14: Eta-wing distribution for prompt(left) and spike(right) candidates.

related processes and ECAL spikes) produce photon candidates that are uniformly distributed in ϕ. The result of the seed time fit used as the central value of the estimate and the ϕ fit is used for calculating the systematic uncertainty. The two results yeild an estimate of beam halo 5.3 ± 6.5 events, where the dominant uncertainty is statistical. The three-component (beam halo, spike, prompt) fit of the seed crystal time distribution in the 3 ns time window yields an estimate of 8.53 $\pm$ 2.04(stat.) spike events for $12.9 fb^{-1}$dataset.

For spikes estimate, we did another cross check using matrix method. First we need to define a variable which can distinguish between spikes and prompt events. We define "eta-wing" as ratio of highest energy neighbour in η to the seed to that of the energy of seed crystal. Naively, it is expected that spikes would have low to no energy, where as real showers should always have some sharing. Figure 5.14 shows the distribution of eta-wing for the real showers selected using $Z \rightarrow ee$ candidates and spikes selected using the timing $t < -12.5ns$ cut.

The number of candidates in-time is given by $N_{\rm can}$, which is equal to the sum of the number of spike candidates, $N_{\rm s}$, and the number of Z candidates, $N_{\rm Z}$. The number of such candidates passing the eta-wing selection obeys the same relation, giving

$$N_{\rm can} = N_{\rm s} + N_{\rm Z}, \quad N_{\rm can}^{\rm wing} = N_{\rm s}^{\rm wing} + N_{\rm Z}^{\rm wing} = \epsilon_{\rm s} N_{\rm s} + \epsilon_{\rm Z} N_{\rm Z} \tag{5.2}$$

where the superscript "wing" indicates passing the eta-wing selection and ϵ is the efficiency for either sample to pass. For eta-wing > 0.015, these efficiencies are measured to be $\epsilon_{\rm s} = 55.7\%$ and $\epsilon_{\rm Z} = 100\%$. Combining the two equations to eliminate $N_{\rm Z}$ and solving for ns yields the estimate for the number of spikes as:

$$N_{\rm s} = \frac{\epsilon_{\rm Z} N_{\rm can} - N_{\rm can}^{\rm wing}}{\epsilon_{\rm Z} - \epsilon_{\rm s}} \ . \tag{5.3}$$

Of the 1903 events passing the candidate selection, 1901 also pass the eta-wing selection, giving the central value for the estimate as 4.5 ± 3.4 events.

Since the two separate estimates for spikes (using timing template fit and matrix method) are consistent within their uncertainties, we add the uncertainties from the 2 methods in quadrature and thus results in 8.53 ± 6.7 events as backgrounds from spikes. To assess the systematic uncertainty in the method, the alternative spike templates are formed where the shower shape variables ($\sigma_{i\eta i\eta}$ or $\sigma_{i\phi i\phi}$) varied from < 0.001 to < 0.002 in steps of 0.0001. Also, we used "eta-wing" < 0.015 to get alternative spike template and then varied the eta-wing from 0.010 to 0.017 in steps of 0.001. The largest deviation by the alternative estimates from the nominal, which is 20% relative to the nominal value, is then assigned as the systematic uncertainty of the method.

5.5 Acceptance and Systematics

The cross section measurement is based on the formula:

$$\sigma \times Br = \frac{N_{data} - N_{BG}}{A \times \epsilon \times L}, \tag{5.4}$$

where N_{data} is the observed number of events and N_{BG} is the number of estimated

background events. A is the geometrical and kinematic acceptance of the selection criteria, ϵ is the selection efficiency within the acceptance, and L is the integrated luminosity. Br is the branching ratio, which in this case is 100%. The product of $A \times \epsilon_{MC}$ is estimated from the Monte Carlo simulation. The values for $A \times \epsilon_{MC}$ are summarized in Table 5.7,5.8,5.9 and 5.10 for ADD and dark matter model respectively. Error indicates the statistical uncertainty on the estimation due to the limited size of the MC sample.

$A \times \epsilon_{MC}$	n=3	n=4	n=5	n=6	n=8
M_D=1TeV	0.218 ± 0.002	0.225 ± 0.002	0.240 ± 0.002	0.253 ± 0.002	0.269 ± 0.002
M_D=2TeV	0.265 ± 0.002	0.267 ± 0.002	0.271 ± 0.002	0.270 ± 0.002	0.276 ± 0.002
M_D=3TeV	0.270 ±0.005	0.277 ± 0.002	0.283 ± 0.002	0.280 ± 0.002	0.283 ± 0.002

Table 5.7: $A \times \epsilon_{MC}$ for ADD as a function of M_D and n.

$A \times \epsilon_{MC}$	m_{DM}=1 GeV	m_{DM}=10 GeV	m_{DM}=50 GeV	m_{DM}=150 GeV	m_{DM}=500 GeV
M_{med}=10 GeV	0.124 ± 0.001			0.190 ± 0.002	0.247 ± 0.002
M_{med}=15 GeV		0.136 ± 0.002			
M_{med}=20 GeV	0.123 ± 0.001				
M_{med}=50 GeV	0.128 ± 0.002	0.127 ± 0.001	0.155 ± 0.002		
M_{med}=95 GeV			0.142 ± 0.002		
M_{med}=100 GeV		0.135 ± 0.002			
M_{med}=200 GeV	0.149 ± 0.002		0.150 ± 0.002	0.184 ± 0.002	
M_{med}=295 GeV				0.170 ± 0.002	
M_{med}=300 GeV	0.162 ± 0.002		0.166 ± 0.002		
M_{med}=500 GeV	0.195 ± 0.002				0.247 ± 0.002
M_{med}=1000 GeV	0.234 ± 0.002			0.234 ± 0.002	
M_{med}=1995 GeV					
M_{med}=2000 GeV	0.269 ± 0.002				0.265 ± 0.002
M_{med}=10000 GeV			0.252 ± 0.002	0.254 ± 0.002	0.266 ± 0.002

Table 5.8: $A \times \epsilon_{MC}$ for Vector Dark Matter as a function of m_{DM} and M_{med}.

Dark matter signal samples produced with fast simulation slightly overestimates the event yield compared to full simulation. An overall scale factor of 0.95 is applied to the predicted event yield in these samples, with an uncertainty on the scale factor of 0.05. The photon energy scale, jet and p_{T}^{miss} energy scale and resolution, and pileup related contributions are considered as sources of systematic uncertainty in the acceptance calculation. The uncertainty on the photon energy scale is about 1.5% and p_{T}^{miss} energy scales, translates into $A \times \epsilon$ as 5%. Contributions from

$A \times \epsilon_{MC}$	m_{DM}=1 GeV	m_{DM}=10 GeV	m_{DM}=50 GeV	m_{DM}=150 GeV	m_{DM}=500 GeV
M_{med}=10 GeV	0.124 ± 0.001	0.139 ± 0.002		0.204 ± 0.002	0.262 ± 0.002
M_{med}=15 GeV		0.138 ± 0.002			
M_{med}=20 GeV	0.125 ± 0.001				
M_{med}=50 GeV	0.127 ± 0.001		0.162 ± 0.002		
M_{med}=95 GeV			0.152 ± 0.002		
M_{med}=100 GeV	0.132 ± 0.002	0.134 ± 0.002			
M_{med}=200 GeV			0.149 ± 0.002		
M_{med}=295 GeV				0.184 ± 0.002	
M_{med}=300 GeV	0.167 ± 0.002		0.164 ± 0.002		
M_{med}=500 GeV				0.194 ± 0.002	
M_{med}=995 GeV					0.248 ± 0.002
M_{med}=1000 GeV	0.236 ± 0.002				
M_{med}=1995 GeV					
M_{med}=2000 GeV	0.269 ± 0.002				0.270 ± 0.002
M_{med}=10000 GeV		0.253 ± 0.002			0.276 ± 0.002

Table 5.9: $A \times \epsilon_{MC}$ for Axial Vector Dark Matter as a function of m_{DM} and M_{med}.

$A \times \epsilon_{MC}$	Λ=3000 GeV
Mx=1 GeV	0.416 ± 0.002
Mx=10 GeV	0.419 ± 0.002
Mx=50 GeV	0.418 ± 0.002
Mx=100 GeV	0.422 ± 0.002
Mx=200 GeV	0.423 ± 0.002
Mx=400 GeV	0.435 ± 0.002
Mx=800 GeV	0.448 ± 0.002

Table 5.10: $A \times \epsilon_{MC}$ for Electroweak Scalar Dark Matter as a function of Mx for Λ=3000 GeV.

the jet energy scale, jet resolution and unclustered energy scale uncertainties are accounted for in the uncertainty on the p_{T}^{miss}. The uncertainty on the integrated luminosity is 6.2%. A summary of the systematic uncertainties on $A \times \epsilon$ for different signal samples and irreducible background is shown in Table: 5.11 and the systematic uncertainties for backgrounds are shown in Table: 5.12.

5.6 Results

After applying our full selection criteria, we observe 400 events in $12.95 fb^{-1}$of data which is in agreement with the total expected SM background of 386 ± 36 events. The estimated number of events and the associated uncertainty for each background process are given in Table 5.13. Distributions of p_{T}^{γ} and p_{T}^{miss} for the selected can-

Sample	Jet energy Scale [%]	Photon energy scale [%]	Unclustered energy scale [%]
ADD M_D=1 d=4	+0.67,-0.64	+1.86,-3.12	+0.12,-0.10
ADD M_D=3 d=3	+0.36,-0.56	+1.16,-0.24	+0.16,-0.12
V m_χ=150 m_V=1000	+0.08,-0.15	+2.31,-1.96	+0.09,-0.09
V m_χ=50 m_V=10000	+0.15,-0.10	+1.90,-1.87	+0.01,-0.01
AV m_χ=150 m_V=10	+0.10,-0.16	+2.60,-2.70	+0.07,-1.7
AV m_χ=1000 m_V=1000	+0.10,-0.11	+1.50,-1.40	+0.01,-0.10
EWK m_χ=1	+0.022,-0.022	+0.21,-0.21	+0.023,-0.023
EWK m_χ=800	+0.005,-0.002	+0.06,-0.06	+0.004,-0.013
$Z(\rightarrow \nu\nu)\gamma$	+1.11,-1.33	+1.31,-4.60	+0.46,-0.48
$W\gamma$	+1.52,-1.73	+1.72,-5.95	+0.23,-0.10

Table 5.11: Percentage systematic uncertainties in $A \times \epsilon_{MC}$ for various signal samples.

Sources	$Z(\nu\bar{\nu}) + \gamma$	Wγ	Jets faking γ	Electron faking γ	jet+γ	Other bkgs
Luminosity	6.2%	6.2%	-	-	6.2%	6.2%
PDF and Scale	5%	9%	-	-	-	-
EWK corrections	11%	7%	-	-	-	-
Jets faking γ	-	-	35%	-	-	-
Elecron faking γ	-	-	-	10%	-	-
jet+γ	-	-	-	-	54%	-
Jet, p_{T}^{miss}, γ energy scale	3%	4.%	-	-	3%	3%
Scale Factors	6%	6%	-	-	6%	6%

Table 5.12: Summary of systematic unceratinties for different background sources.

didate events are shown in Figure 5.15 together with their respective estimated background distributions.

Process	Estimate
$Z(\rightarrow \nu\bar{\nu}) + \gamma$	215.4 ± 32.3
$W(\rightarrow \ell\nu) + \gamma$	57.2 ± 8.0
$W \rightarrow e\nu$	52.7 ± 4.2
jet $\rightarrow \gamma$ fakes	5.9± 1.7
Spikes	8.5± 6.7
Beam halo	5.3 ± 6.5
$\gamma + jet$	10.1±5.7
ZZ	1.3± 0.7
ttγ	8.2 ± 0.6
$W\mu\nu$	8.5 ± 3.0
$W\tau\nu$	5.2 ± 2.3
WZ	3.5± 1.7
$Z(\ell\ell)\gamma$	2.9± 0.2
$WW\gamma$	0.7± 0.1
Total background	385.4 ± 35.6
Data	400

Table 5.13: Summary of estimated backgrounds and observed total number of candidates for 12.95 fb^{-1} of 2016 data.

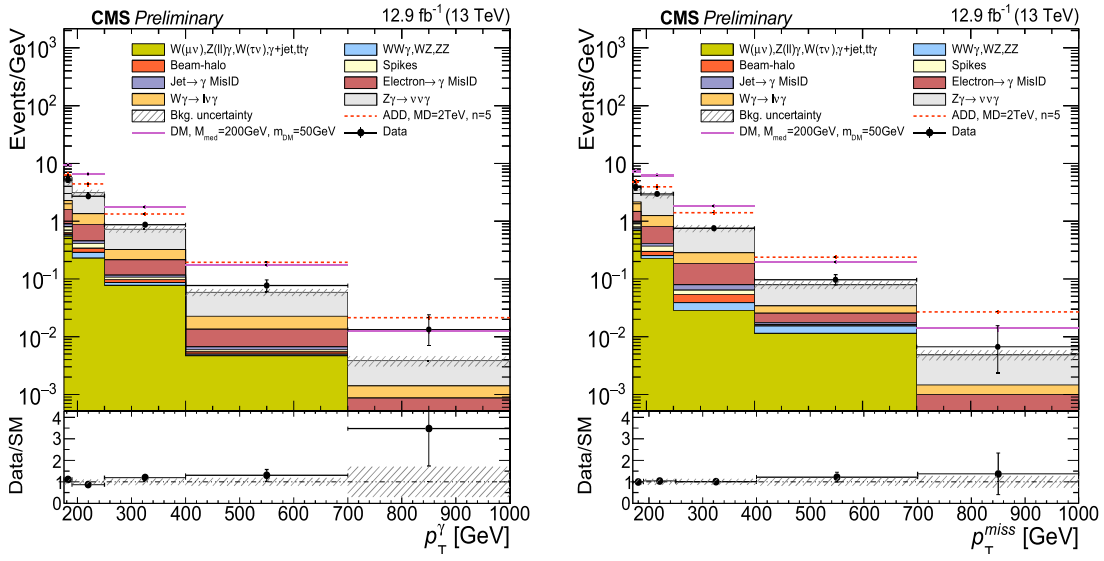

(a) photon p_{T} **(b)** particle flow p_{T}^{miss}

Figure 5.15: The p_{T}^{γ} and p_{T}^{miss} distributions for the candidate sample, compared with estimated contributions from SM backgrounds. The background uncertainties include statistical and systematic components. The last bin includes the overflow. The lower panel shows the ratio of data and SM background predictions, where the hatched band shows the systematic uncertainty

5.7 Interpretation

No excess of data with respect to the SM prediction is observed and limits are set on the DM and ADD models. For each signal model, a 95% confidence level (CL) cross section upper bound is obtained utilizing the asymptotic CLs prescription [99–101]. In this method, a Poisson likelihood for the observed number of events is maximized under different signal strength hypotheses, taking the systematic uncertainties as nuisance parameters that modify the signal and background predictions. Each nuisance parameter is assigned a log-normal probability distribution, using the systematic uncertainty value as the width. The best fit background predictions differ from the original by at most 4%. Confidence intervals are drawn by comparing these maximum likelihood values to those computed from background-only and signal-plus-background pseudo-data.

5.7.1 Limits on simplified dark matter models

As discussed in section 2.2.1.2, in simplified DM models Dirac DM particles couple to a vector or axial-vector mediator, which in turn couples to the SM quarks. Model points are identified by a set of four parameters: the DM mass m_{DM}, the mediator mass M_{med}, the universal mediator coupling to quarks g_q and the mediator coupling to DM particles g_{DM}. In this analysis, we fix the values of g_q and g_{DM} to 0.25 and 1.0, respectively, and scan the $M_{med} - m_{DM}$ plane [102].

Figure 5.16 shows the 95% confidence level (CL) upper limits with respect to the corresponding theoretical cross section ($\mu_{95} = \sigma_{95\%}/\sigma_{Theory}$) for the Vector and the Axial-vector mediator. The solid black and red curve shows the observed and expected exclusion for $\mu_{95} = 1$ in the $M_{med} - m_{DM}$ plane. Experimental uncertainties are included on the signal model during the computation of the expected upper limit. The uncertainty in the theoretical cross section is translated to the uncertainty in the observed exclusion contour. Considering the simplified DM models, mediator masses of up to 700 GeV are excluded for small m_{DM} values.

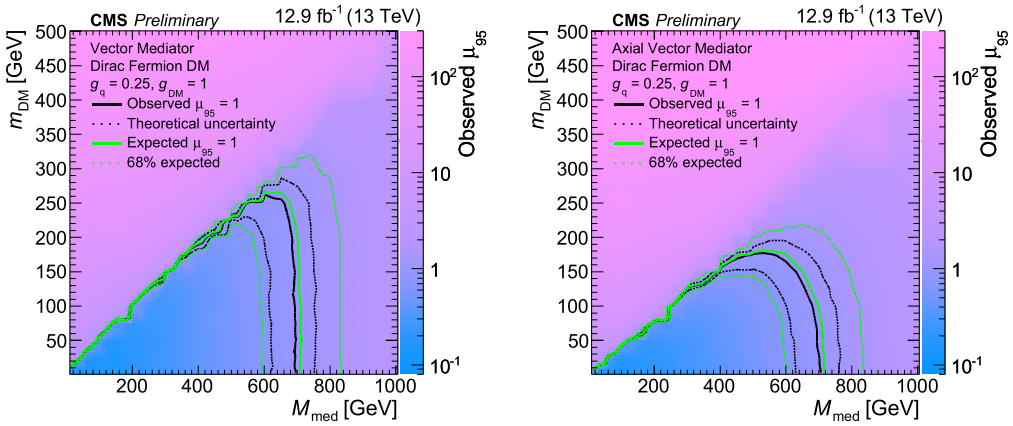

Figure 5.16: The ratio of 95% CL cross section upper limits to theoretical cross section (μ_{95}) for DM simplified models in the $M_{med} - m_{DM}$ plane for vector (left) and axialvector(right) mediator, assuming g_q =0.25 and g_χ =1. Expected and observed exclusion contours ($\mu_{95} = 1$) are overlaid, where mass points below the contours are excluded.

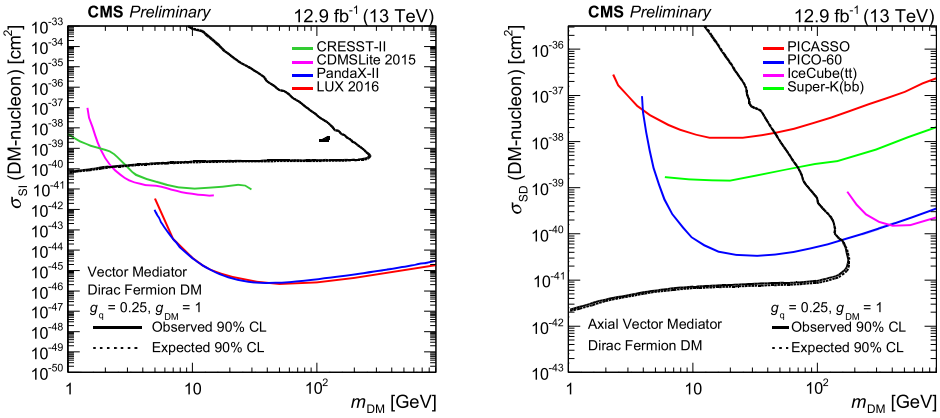

Figure 5.17: The 90% CL exclusion limits on the χ-nucleon spin-independent (left) and spin-dependent (right) scattering cross sections involving a vector and axial-vector operator respectively in a simplified model of dark matter production as a function of the m_{DM}. Simplified model DM parameters of $g_q = 0.25$ and $g_{DM} = 1$ are assumed. The region to the upper left of the contour is excluded. The median expected 90% CL curve overlaps the observed 90% CL curve. Also corresponding exclusion contours from the recent results by CDMSlite [37], LUX [104], PandaX [105], CRESST [106], PICO-60 [38], IceCube [42], PICASSO [108] and SuperKamiokande [107] are shown.

The exclusion contours are also translated into the $\sigma_{SI/SD} - m_{DM}$ plane, where $\sigma_{SI/SD}$ are the spin-independent/dependent DM-nucleon scaterring cross sections. The translation and presentation of the result follows the prescription given in Ref. [102]. We use 90% CL to do a direct comparison with the limits from the direct detection experiments. Figure 5.17 shows the comparison of the limits at 90% CL. When compared to the direct detection experiments, the limits obtained from this search provide stronger constraints on dark matter mass below 2 GeV for vector mediator and that of below 200 GeV for axial-vector mediator.

5.7.2 Limits on electroweak dark matter models

For DM effective field theory (EFT) model with a contact interaction of type $\gamma\gamma\chi\overline{\chi}$ [103], the interaction is described by four parameters: the coupling to photons, parametrized in terms of coupling strengths k_1 and k_2; the DM mass m_{DM}; and the

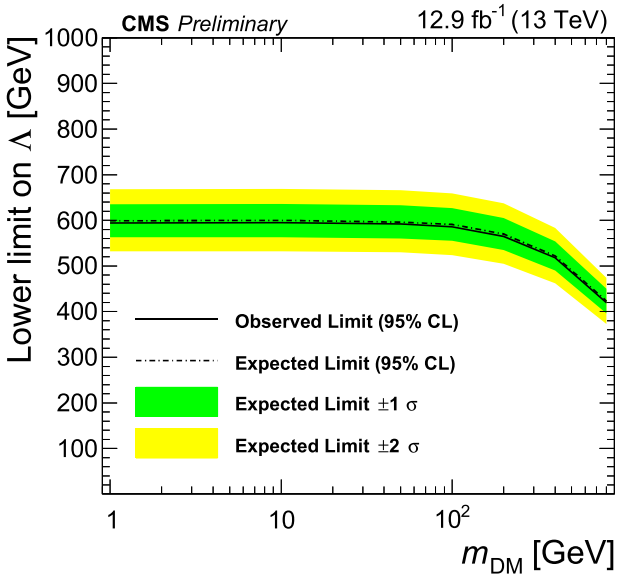

Figure 5.18: The 95% CL observed and expected lower limits on Λ as a function of dark matter mass m_{DM}, for a dimension-7 operator EFT model.

suppression scale Λ. Since the interaction cross section is directly proportional to Λ^{-6}, cross section upper limits are translated into lower limits on Λ. The expected and observed lower limits on Λ as a function of m_{DM} are shown in Figure 5.18. Values of Λ up to 600 GeV are excluded at 95% CL.

5.7.3 Limits on ADD Model

Figure 5.19 shows the observed upper limit and the theoretically calculated ADD graviton production cross section for $n = 3$ extra dimensions, as a function of M_D. Lower limits on M_D for various values of n extra dimensions are summarized in Table 5.14, and are compared with CMS results at $\sqrt{s} = 8$ TeV [44] in Figure 5.20. The trends of the two results differ because the graviton production cross section can be increasing or decreasing in n depending on the values of $\sqrt{s}$ and M_D [55]. Values of M_D up to 2.49 TeV for $n = 6$ are excluded by the current analysis.

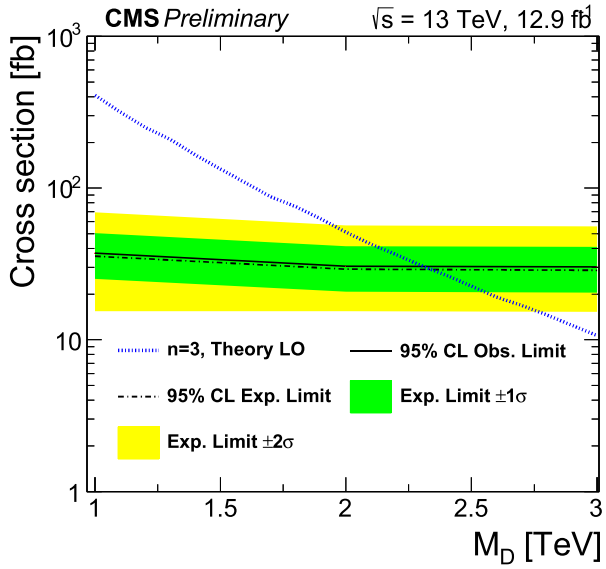

Figure 5.19: The 95% CL upper limits on the ADD graviton production cross sections as a function of M_D for $n = 3$.

n	Obs. Limit [TeV]	Exp. Limit, [TeV]
3	2.31	2.34
4	2.36	2.38
5	2.43	2.46
6	2.49	2.51

Table 5.14: The 95%CL observed and expected lower limits on M_D as a function of n.

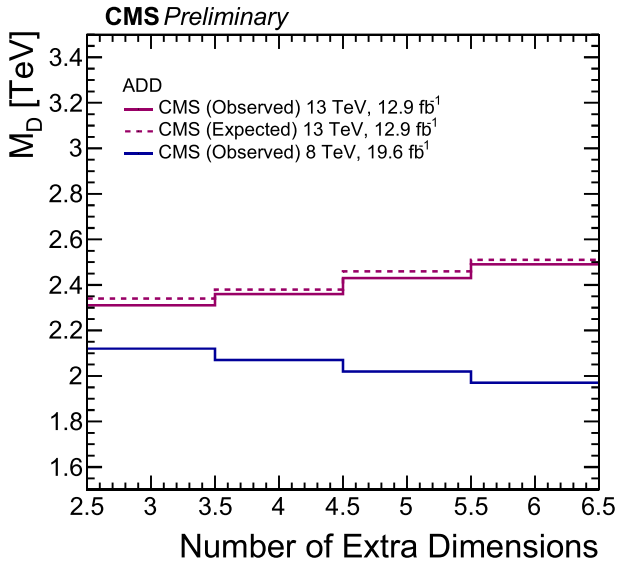

Figure 5.20: Lower limit on M_D as a function of the number of ADD extra dimensions, n.

5.8 Summary

Proton-proton collision events containing a high transverse momentum photon and large missing transverse momentum have been investigated to search for new phenomena, using the data set corresponding to $12.95 fb^{-1}$of integrated luminosity recorded at $\sqrt{s} = 13$ TeV at CERN LHC. No deviations from the standard model predictions are observed. For the simplified DM model considered, the search excludes mediator masses of up tp 700 GeV for low-mass dark matter. For DM EFT model, values of Λ up to 600 GeV are excluded. The most stringent limits to date are obtained on the effective Planck scale in the ADD model with large spatial extra dimensions. Values of the fundamental Planck scale up to $2.31 - 2.49$ TeV, depending on the number of extra dimensions, are excluded.

CHAPTER 6

Simulation Study of the Endcap Calorimeter for CMS Phase II Upgrade

In the High Luminosity LHC physics program, the accelerator will provide CMS an additional integrated luminosity of about 3000 fb^{-1} over 10 years of operation, starting from 2025 [110]. This will substantially enlarge the mass reach in the search for new particles and will also greatly extend the potential to study the properties of the Higgs boson discovered at the LHC in 2012. In this high luminosity environment (Luminosity $\approx 5 \times 10^{34}$ Hz/cm^2), the performance of various detector components (mostly in the high eta region) will suffer because of the increased hadron flux (10^{13} neutrons/cm^2) through them. Beyond 500 fb^{-1}, the performance of the calorimeter will be degraded to an extent which will be hard to recover. Thus it becomes necessary to replace the endcap calorimeter with the one which can survive in a high luminosity environment and can give stable resolution as a function of luminosity.

Two different options are considered by the CMS collaboration for the Phase II Detector Upgrade:

- Shashlik electromagnetic calorimeter + HE rebuild
- High Granularity Calorimeter (HGCAL)

In this chapter simulation study of energy resolution, position resolution and π^0-γ separation of the Shashlik electromagnetic calorimeter and test beam study of the High Granularity Calorimeter are discussed.

6.1 Shashlik Electromagnetic Calorimeter

Shashlik Electromagnetic Calorimeter is a sampling calorimeter with alternative layers of active (scintillator) and passive (absorber) material. For scintillator LYSO was the choice. LYSO (cerium doped lutetium yttrium silicate) is a radiation hard, high light yield (about 4 times of BGO), high stopping power (ρ = 7.4 g/cm^3 , X_0 = 1.14 cm and $R_{Moliere}$ = 2.07 cm) and fast response ($\tau \approx$ 40 ns) inorganic scintillator [111, 112].

For absorber, lead and tungsten are the two possible choices. For this study, the baseline option uses 4 mm thick lead layers interleaved with 2 mm thick LYSO. The alternative scenario considered uses 2.5 mm thick tungsten with 1.5 mm thick LYSO [113]. The scintillation light is read out using four wavelength shifting fibers going all the way through a Shashlik tower.

The following properties of the Shashlik calorimeter are studied:

1. The sampling resolution as a function of number of absorber/scintillator layers as well as total energy resolution;

2. Position resolution of the impact point of photons on the calorimeter;

3. π^0/γ separation using the information from the four fibers.

These are discussed in Sections 6.1.2, 6.1.3 and 6.1.4 respectively.

6.1.1 Simulation

A stand-alone detector setup consisting of alternative layers of absorbers (either 4 mm thick lead or 2.5 mm thick tungsten) and scintillators (2.0 mm or 1.5 mm thick LYSO) is defined in the framework of GEANT4 [90,114]. GEANT4 version 9.6.p02 is used with the physics list QGSP_FTFP_BERT. Light saturation effect is introduced through the use of Birk's law [115]:

$$w = \frac{k_0}{\left(1 + k_1 \cdot \left(\frac{dE}{dX}\right) + k_2 \cdot \left(\frac{dE}{dX}\right)^{-1}\right)}$$

with $k_0 = 0.883$, $k_1 = 6.50 \times 10^{-3}$ MeV^{-1}·g·cm^{-2} and $k_2 = -0.241$ MeV·g^{-1}·cm^2 as measured in [116]. The weight factor w is restricted in the range 0.1:1.0.

For studies of energy resolution, a single Shashlik tower, with no lateral segmentation and with each layer of transverse size 100×100 cm^2 is used. The gun particle is directed along the central axis of the tower. The transverse size of the tower is sufficient to avoid any lateral leakage of the shower. Monochromatic electrons of energy 50, 150 and 200 GeV and monochromatic photons of energy 50, 100, 150, 200, 300, 400 and 500 GeV are produced for sampling resolution study as a function of number of layers. To study total energy resolution, electrons of energies 10, 20, 30, 50, 70, 100, 150, 200, 250, 300, 500, 700 and 1000 GeV are generated with 28 layers of absorber and 29 layers of scintillators. Ten thousand events are generated for each sample. Also, LYSO is considered to be undamaged by radiation (*i.e.* its attenuation length is taken to be 100 cm in this scenario).

For π^0-γ separation studies, a detector setup with 28 layers of absorber and 29 layers of scintillators in a 11×11 matrix is defined. Transverse size of each tower in each layer is chosen to be 14×14 mm^2. Five fiber paths are defined of which the central fiber is for calibration and the other four fibers are at positions (±3.5 mm, ±3.5 mm)

with respect to the central axis. They are read out individually or to a combined output. The fibers are of diameter 1.6 mm and are inserted in holes of diameter 1.6 mm. The hit position is uniformly distributed in X and Y directions between -7 mm and $+7$ mm with respect to the centre of the central Shashlik tower. All the samples are generated using single particle gun with momentum along the Z direction. The gun is placed at a distance of 3.2 m from the calorimeter. For this study, photons and π^0's of energy 10, 20, 30, 50, 70, 100, 150 and 300 GeV are shot at the calorimeter.

Energy deposited at a given point in the scintillator plate is shared unequally by the four fibers. The closer a fiber is to the point of impact of the photon, the higher its probability of collecting light is. Also the probability distribution of scintillator light among the fibers depends on the transmission coefficient of the scintillator and hence on integrated luminosity. This is estimated in a separate study [117] using SLitrani [118, 119].

To validate the geometry, total energy deposit in the scintillator of the 11×11 matrix is looked at. As shown in Figure 6.1, the total energy deposit in the scintillator for π^0 and for γ are very similar as expected.

6.1.2 Energy Resolution

The energy resolution in the Shashlik detector depends on the following factors:

1. energy leakage;
2. sampling fluctuation;
3. photo statistics;
4. electronic noise;
5. other sources which include contributions from pile-up and inter-calibration.

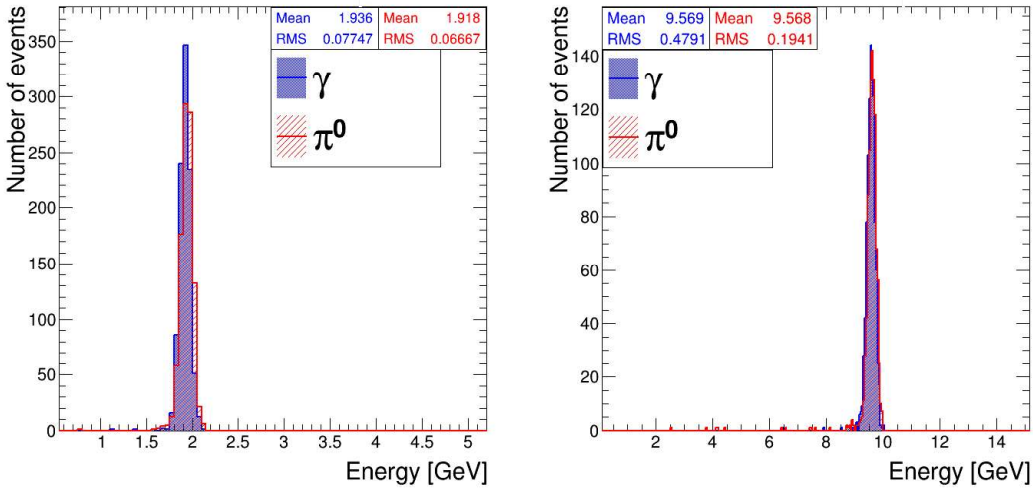

Figure 6.1: Total energy deposit in the scintillator of the 11 × 11 matrix for 10 GeV photons and π^0's on the left and 50 GeV photons and π^0's on the right. Blue shaded histogram is for photons and red hatched histogram is for π^0's.

The second term is specific for a sampling calorimeter while the other terms contribute also to any homogeneous calorimeter like the one used in the CMS experiment. Sampling resolution depends on the number of layers and the relative thickness between absorber and scintillator. A study is performed to obtain the optimum number of layers to achieve good sampling resolution.

6.1.2.1 Sampling Resolution

For a given thickness of the absorber and sensitive layer and a given energy of electron/photon gun the sampling fraction is defined as

$$F_s = \frac{E_S}{E_S + E_A} \tag{6.1}$$

where E_S and E_A are the energies deposited in the scintillator layer and the absorber layer. The deposited energies in the scintillator as well as in the absorber layers follow Gaussian distribution. Figure 6.2 shows distributions of sampling fractions

for 50 GeV and 100 GeV electrons in a configuration with 18 and 30 layers. The absorber in both the configurations is lead. Figure 6.3 shows similar distributions for 50 GeV and 100 GeV photons in a detector configuration with 18 and 30 layers. This configuration is with tungsten as absorber. Gaussian function provides good description of these distributions and the fits are used to estimate the sampling resolutions. One advantage of estimating the sampling resolution from F_S and not estimating from the distribution of E_S is that E_S contains also the contribution to resolution due to leakage. In case of sampling fraction, the term due to leakage appears in the numerator and the denominator and gets canceled.

Fits are performed for each energy point and for each configuration. The fitted mean ($\bar{E}$) and the fitted width (σ) of the Gaussian are used to estimate the energy resolution:

$$\textit{sampling-resolution} = \sigma/\bar{E}, \tag{6.2}$$

Figure 6.4 shows the sampling resolution for electrons and photons as a function of number of layers of absorber and scintillator. The following points are to be noted:

1. For same number of layers, sampling resolution becomes better as the energy increases.

2. As the number of layers increases, sampling resolution becomes better.

3. For number of layers larger than 28, the resolution becomes nearly flat. This corresponds to around 25 radiation lengths (X_0) in both the configurations (Pb-LYSO and W-LYSO), when longitudinal shower leakage is very small. Both configurations seem to give similar results within the statistics.

4. $25X_0$ corresponds to ~16.8 cm for Pb-LYSO and 11.8 cm in case of W-LYSO. If detector length is not an issue, then one can go with the less expensive configuration.

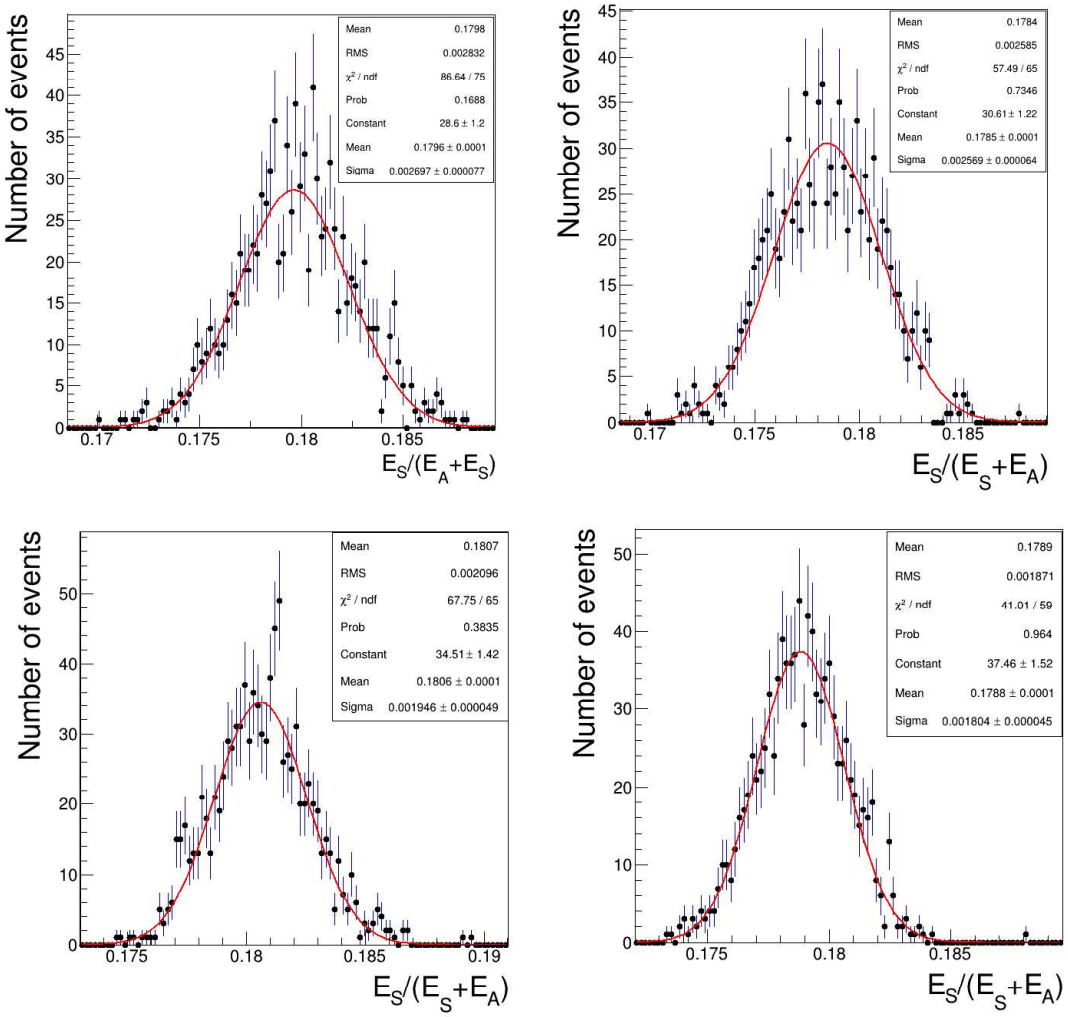

Figure 6.2: The top-left and bottom-left plots show the distributions of sampling fraction (F_S) for 18 layers and the top-right and bottom-right plots are for 30 layers. Top plots are for 50 GeV electrons and bottom plots are for 100 GeV electrons. These distributions are fitted to Gaussian distribution functions.

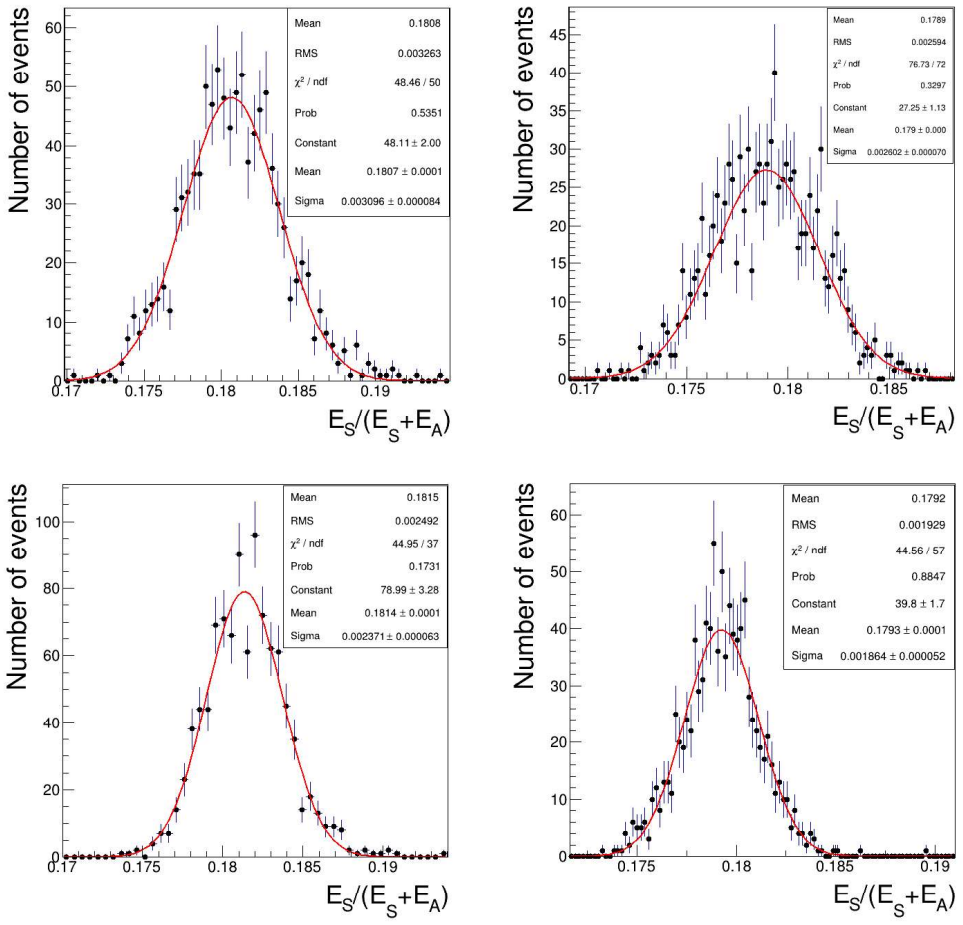

Figure 6.3: The top-left and bottom-left plots show the distributions of sampling fraction (F_S) for 18 layers and the top-right and bottom-right plots are for 30 layers. Top plots are for 50 GeV photons and bottom plots are for 100 GeV photons. These distributions are fitted to Gaussian distribution functions.

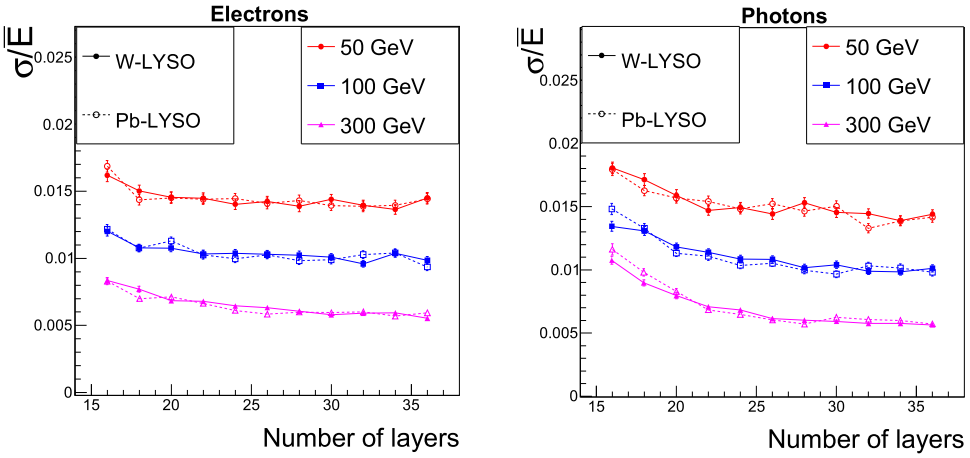

Figure 6.4: Plot on the left shows the sampling resolution of electrons of various energies for different number of layers of Pb-LYSO (dashed line with hollow triangle) and W-LYSO (solid line with solid circle). The plot on the right shows the same for photons.

6.1.2.2 Total Energy Resolution

Following are the terms contributing to the total energy resolution of the Shashlik detector:

Energy leakage: To estimate this term, distributions of E_A+E_S are plotted in Figure 6.5 for different electron beam energies. The $\sigma/\bar{E}$ of this distribution gives the energy resolution due to leakage, where σ is the measure of spread of the shower distribution and $\bar{E}$ is the mean of the shower distribution. It has low energy tail due to energy leakage because of limited length of the detector. Since the transverse size is 100 cm which is much larger than the Moliere radius (2.07 cm) of the LYSO, transverse energy leakage is negligible. The distributions of E_A+E_S are fitted with the Crystal Ball (CB) function (as given in equation 6.3) because of the presence of low energy tail arising from

shower leakage.

$$\begin{aligned} f(x;\alpha,n,\bar{E},\sigma) &= N \times exp\left(\frac{-(x-\bar{E})^2}{2\sigma^2}\right), \; for \; \frac{x-\bar{E}}{\sigma} > -\alpha \\ &= N \times A \times \left(B - \frac{x-\bar{E}}{\sigma}\right)^{-n}, \; for \; \frac{x-\bar{E}}{\sigma} < -\alpha \end{aligned} \quad (6.3)$$

where N is the normalization factor and α, n, $\bar{E}$, σ are parameters of the fit. A is given as:

$$A = \left(\frac{n}{|\alpha|}\right)^n \times exp\left(-\frac{|\alpha|^2}{2}\right) \quad (6.4)$$

and B is given as:

$$B = \frac{n}{|\alpha|} - |\alpha| \quad (6.5)$$

Figure 6.5 shows the CB fit to the distribution of E_A+E_S. The CB parametrization fits the distribution well. The fitted mean of the CB function is taken as $\bar{E}$. To estimate the σ_{68}, 68% interval around $\bar{E}$, is constructed using the parameters of the CB fit. The interval is formed in such a way that for each side of the mean, the area covered is 68% of the area of that side. σ_{68} is the half width of the interval as obtained by the above construction. The values of $\sigma_{68}/\bar{E}$ are then plotted as a function of energy. Fluctuations due to energy leakage are parametrized using Grindhammer-Peter's parametrization [120]:

$$\sigma_{leakage}(\ln(E/E_c)) = (s1 + s2 \times \ln(E/E_c))^{-1}, \quad (6.6)$$

where E_c is the critical energy and is dependent on the material of the detector. The above equation is expanded up to the third power in $\ln(E/E_c)$ and the resolution due to leakage is fitted with a function of type $p_0 + p_1 \times \ln E + p_2 \times (\ln E)^2 + p_3 \times (\ln E)^3$. Fitted values of p_0, p_1, p_2 and p_3 are shown in Table 6.1.

Sampling fluctuation: It is estimated for each energy point exactly the same

parameter	Fitted value
p_0	0.118 ± 0.010
p_1	-0.058 ± 0.007
p_2	$(9.8 \pm 1.6) \times 10^{-3}$
p_3	$(-5.3 \pm 1.2) \times 10^{-4}$

Table 6.1: Fitted values of the parameters when $\sigma_{68}/\bar{E}$ due to leakage is fitted with function $p_0 + p_1 \times \ln E + p_2 \times (\ln E)^2 + p_3 \times (\ln E)^3$.

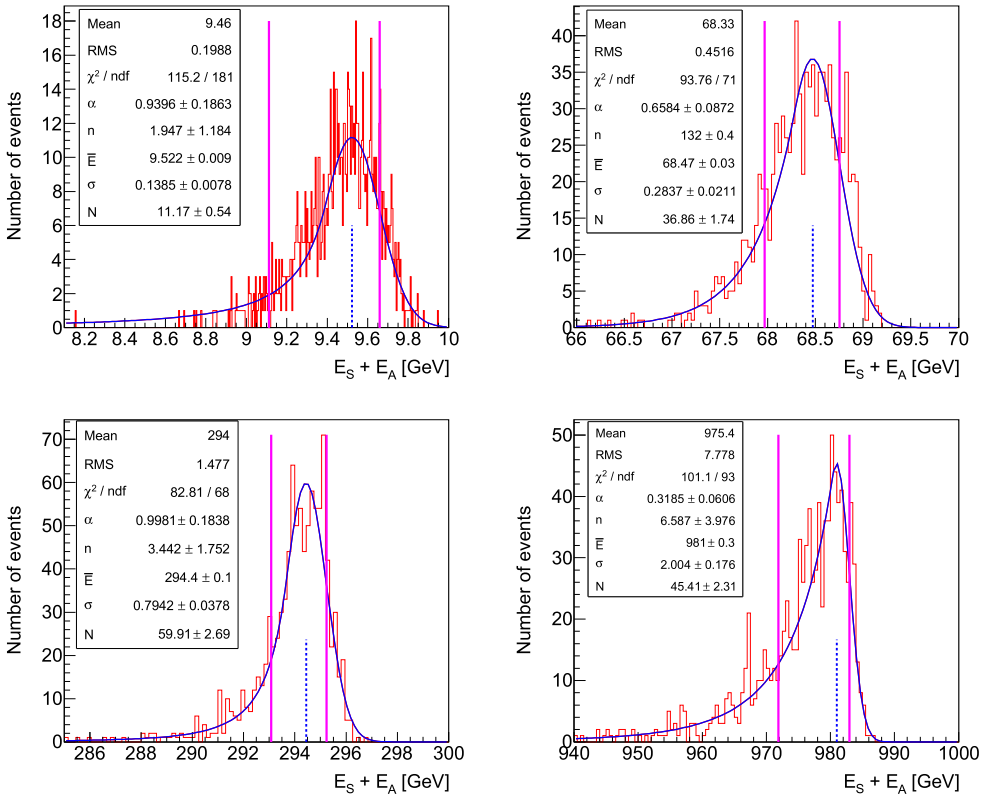

Figure 6.5: The distribution of E_S+E_A for 10 GeV electrons on the top-left; 70 GeV electrons on top-right; 300 GeV electrons on bottom-left and 1000 GeV electrons on bottom-right. The blue curves show the Crystal Ball fit to the distributions. The pink lines show the σ_{68} which is the 68% interval constructed as discussed in the text and the blue dotted lines show the fitted Crystal Ball mean.

way as described in the previous sub-section. This is done for a 28 layer configuration. The distribution of $\sigma/\bar{E}$ is plotted as a function of energy and fitted with a function of type $p_0/\sqrt{E}$. Fitted value of p_0 comes out to be 0.104 $\pm$ 0.001 .

Photo-statistics: To estimate the contribution due to photo-statistics, the energy collected in all the scintillator layers is converted to the number of photo-electrons (p.e.) in the photo-detector. The total number of p.e. from the scintillator is

$$N_{pe} = \Sigma E_i \ \times \ LE \ \times \ LY \tag{6.7}$$

where E_i is the energy deposit in i'th layer, LE is the light collection efficiency and LY is the light yield. The light yield is different for different materials [121]. The photo-statistics contribution can vary depending on the light yield of the material. Average light collection efficiency (LE) is taken to be 0.5% [122] for each layer. (Only a small fraction of scintillation photons is collected by the fibers which go through the holes of each layer and thus leads to such a low efficiency). The distribution of p.e. follows Poisson distribution and hence the fluctuation has a $\sqrt{LY}$ dependence. The distributions of $\sigma/\bar{E}$ in Figure 6.6 are fitted with a function of type $p_0/\sqrt{LY}$. The fit yields p_0 to be 0.1068 $\pm$ 0.0001 for 100 GeV electron beam energy. Figure 6.7 shows the distribution of $\sigma/\bar{E}$ as a function of incident energy for different values of LY. Fits of these distributions to functions of the type $p_0/\sqrt{E}$ yield p_0 to be 0.0171 $\pm$ 0.0001 for light yield value of 4000 p.e./MeV.

Electronic noise: Contribution of electronic noise in the photo-detectors to the energy resolution depends on the fluctuation in the number of photo electrons contributing to the noise. It varies depending on the read-out scheme. Figure 6.8 shows the noise distribution as a function of mean number of p.e. corresponding to electronic noise for different beam energies. Fits to the energy

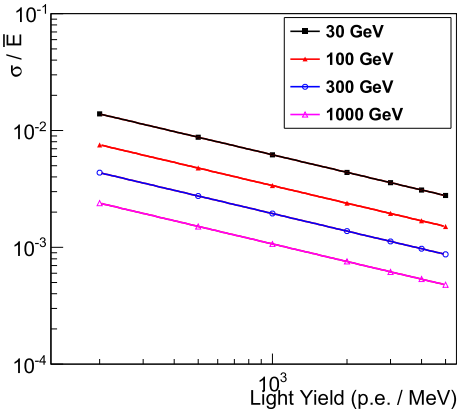

Figure 6.6: Photo-statistics contribution as a function of light yield (LY) for different beam energies

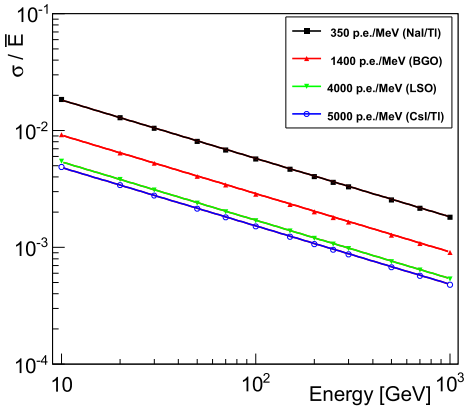

Figure 6.7: Photo-statistics contribution as a function of energy for different light yields.

resolution $\sigma/\bar{E}$ to a function of the type $p_0 \times p.e.$ yield a value of p_0 to be $(2.8 \pm 0.1) \times 10^{-6}$ for 100 GeV electron beam energy. Figure 6.9 shows the

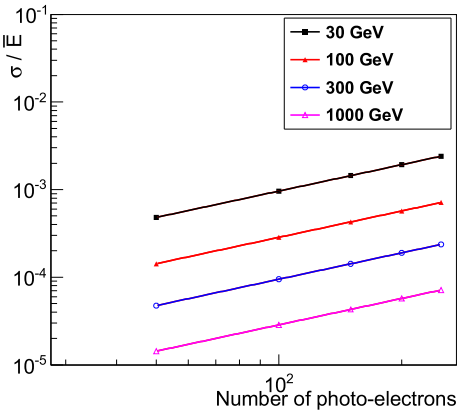

Figure 6.8: Noise contribution as a function of photo-electrons for different beam energies.

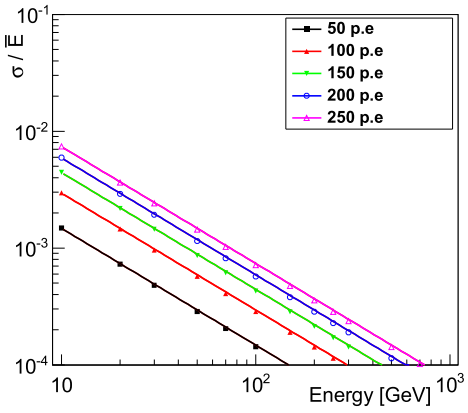

Figure 6.9: Noise contribution as a function of energy for different number of photo-electrons.

distributions of $\sigma/\bar{E}$ as a function of energy and are fitted with functions of the type p_0/E for different numbers of mean photo-electrons. Fitted value of p_0 comes out to be 0.0442 ± 0.0002 for 150 as mean number of photo-electrons.

Total energy resolution: Total energy resolution is the sum (in quadrature) of the above four terms. The distribution of $\sigma/\bar{E}$ is plotted as a function of beam

energy in Figure 6.10 for light yield value of 4000 p.e./MeV and mean noise of 150 p.e. The energy resolution is fitted with a function of the type

$$\sqrt{\left(p_0/\sqrt{E}\right)^2 + (p_1/E)^2 + (p_2 + p_3 \times \ln E + p_4 \times (\ln E)^2 + p_5 \times (\ln E)^3)^2}.$$

and the fitted parameters are shown in Table 6.2. Figure 6.10 also shows contributions of each of the term as given above. It can be seen that the parameters of the total fit are in agreement with the individual parameters obtained by fitting all the terms (*i.e.* leakage, sampling, statistics and noise) of the resolution individually. The parameter, p_0 has contribution from both the terms, sampling and statistics. But the major contribution comes from sampling and hence the fitted parameter p_0 is closer to the fitted value of the sampling term.

parameter	Fitted value
p_0	0.103 ± 0.006
p_1	0.087 ± 0.056
p_2	0.118 ± 0.002
p_3	-0.058 ± 0.001
p_4	$(9.8 \pm 0.1) \times 10^{-3}$
p_5	$(-5.3 \pm 0.1) \times 10^{-4}$

Table 6.2: Table showing fitted values of the parameters when $\sigma/\bar{E}$ of total energy resolution is fitted with function $\sqrt{\left(p_0/\sqrt{E}\right)^2 + (p_1/E)^2 + (p_2 + p_3 \times \ln E + p_4 \times (\ln E)^2 + p_5 \times (\ln E)^3)^2}$.

Finally, to check the effect of this detector resolution on the mass resolution of the Higgs boson, 10000 events are generated where the Higgs boson is produced via gluon gluon fusion, and decays to a photon pair. Higgs mass is taken to be 125 GeV. In order to mimic the effect of the Shashlik detector, energy of each photon was smeared with the parameters as given in Table 6.2 in the following way:

1. a resolution term, σ/E is calculated for each of the photons using the param-

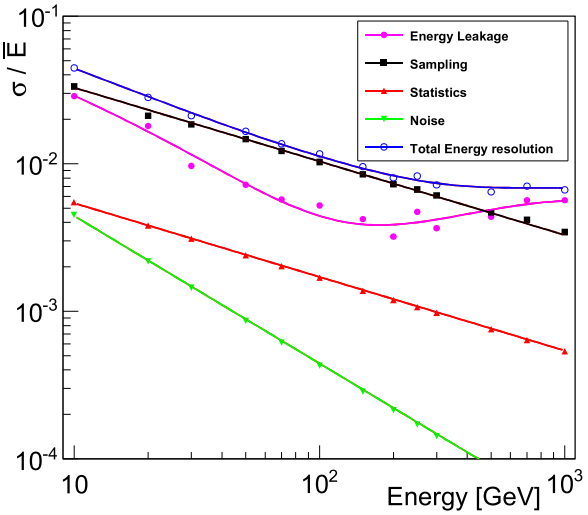

Figure 6.10: Contributions of each term to the total resolution. Points are the actual points as a function of energy and lines are the fitted functions.

eters of Table 6.2 and the expression given in there;

2. a Gaussian random number is generated with mean 1 and $\sigma_{gaus} = \sigma/\mathrm{E}$;

3. energy and momentum of each photon is multiplied with the above random number;

4. the di-photon mass is fitted with a Gaussian function. The σ from the fit is taken as the estimate of resolution of Higgs mass.

Figure 6.11 shows the Gaussian fit to Higgs mass, when both the photons are in the endcap electromagnetic calorimeter, obtained using the above procedure. The fitted σ is estimated to be 0.64 ± 0.02 GeV.

6.1.3 Position Resolution

When a particle hits the electromagnetic calorimeter, its deposited energy gets distributed in the hit tower as well as the towers around it. The hit position can be estimated from the weighted mean of the position of the towers in which energy has

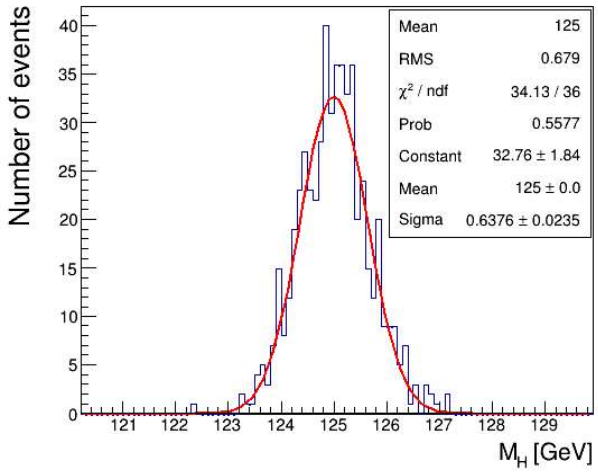

Figure 6.11: Resolution on Higgs mass with a Shashlik ECAL and with both the photons in the endcap electromagnetic calorimeter.

been deposited, where the weights are proportional to the energy deposited in the towers (so that higher the energy, more is the weight and hence more likely that the particle has hit that tower). This method of estimating the position is called the center of gravity (COG) method. The equations used to estimated coordinates in this way are given in Equation 6.8.

$$\begin{aligned} x_{meas} &= \Sigma x_i \times E_i/\Sigma E_i \\ y_{meas} &= \Sigma y_i \times E_i/\Sigma E_i \end{aligned} \tag{6.8}$$

Here, the sum is over the 3×3 array of towers, if a combined signal from the four fibers are read out for each tower, or it is over $3 \times 3 \times 4$ array of fibers, if individual fiber information is used. Figures 6.12 and 6.13 show the true impact point x_{true} and y_{true} as a function of the measured coordinates x_{meas} or y_{meas} for 50 GeV and 150 GeV photons. The resulting distributions show deviations from linearity and roughly follows an S-shape. This feature is observed for combined as well as individual fiber readouts.

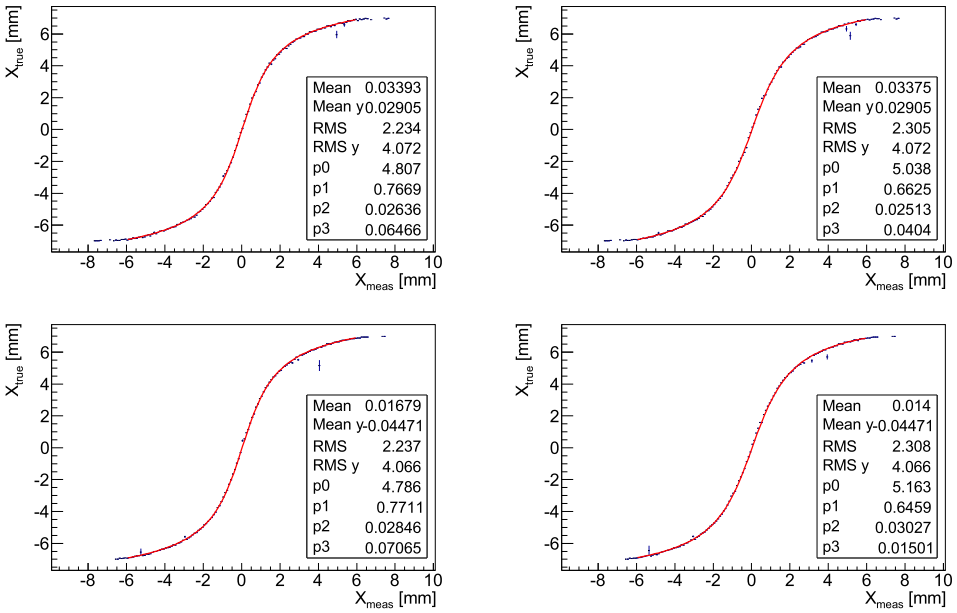

Figure 6.12: 2-D distribution of x_{true} versus x_{meas} for photons of energy 50 GeV (top plots) and 150 GeV (bottom plots) when linear weights are used to estimate the COG. The relation between x_{meas} and x_{true} is fitted with a S-shaped curve as parametrized in the Equation 6.10 and shown by the red curve in the figure. The left (right) figures refer to cases when combined (individual) fiber information is used.

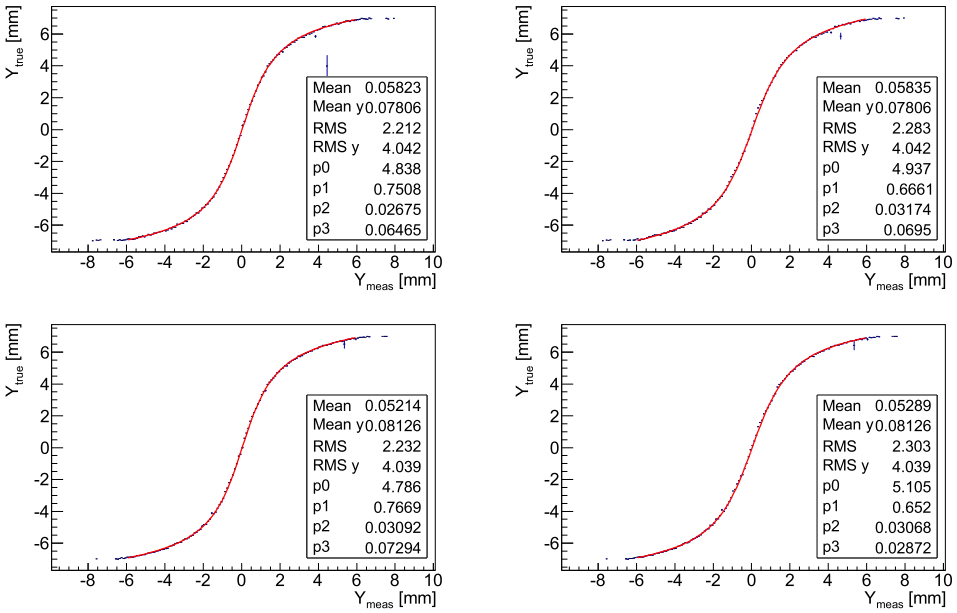

Figure 6.13: 2-D distribution of y_{true} versus y_{meas} for photons of energy 50 GeV (top plots) and 150 GeV (bottom plots) when linear weights are used to estimate the COG. The relation between y_{meas} and y_{true} is fitted with a S-shaped curve as parametrized in the Equation 6.10 and shown by the red curve in the figure. The left (right) figures refer to cases when combined (individual) fiber information is used.

Some features of the S-shape curve are summarized below:

1. At the center, x_{true} (y_{true}) = x_{meas} (y_{meas}). This is because the deposited energy is mostly contained in the central tower.

2. On moving away from the center in either direction, x_{true} (y_{true}) > x_{meas} (y_{meas}). There is an exponential fall in the spread of the energy for other towers. So linear weights E_i give more weight to the hit tower and hence the position is not correctly determined.

3. At the edge (in this case at ±6 mm), the energy is distributed equally in the adjacent towers and roughly equal weight is given to them and hence x_{true} (y_{true}) again becomes x_{meas} (y_{meas}).

Above three points essentially summarize why the S-shape arises. Instead of linear weights, log weights of energy fraction are also tried. Since the energy falls off as an exponential, the log weights compensate the exponential decrease and hence the estimated position is closer to the true one. Equation 6.9 shows the relations used to estimate the coordinates of the hit point with log weights. This equation depends highly on the value of w_0. The optimum value of w_0 depends on whether individual or combined fiber information is used. Figures 6.14 and 6.15 show the 2-D distribution of x_{true} (y_{true}) VS x_{meas} (y_{meas}) for 50 GeV and 150 GeV photons when log weights are used for the two cases of using combined or individual fiber information.

$$\begin{aligned} x_{meas} &= \Sigma x_i \times w_i / \Sigma w_i \\ y_{meas} &= \Sigma y_i \times w_i / \Sigma w_i \\ w_i &= Max(0, w0 + \ln(E_i/E_T)) \end{aligned} \tag{6.9}$$

where $w_0 = 4.7$ for combined fiber information and $w_0 = 6$ for individual fiber

information.

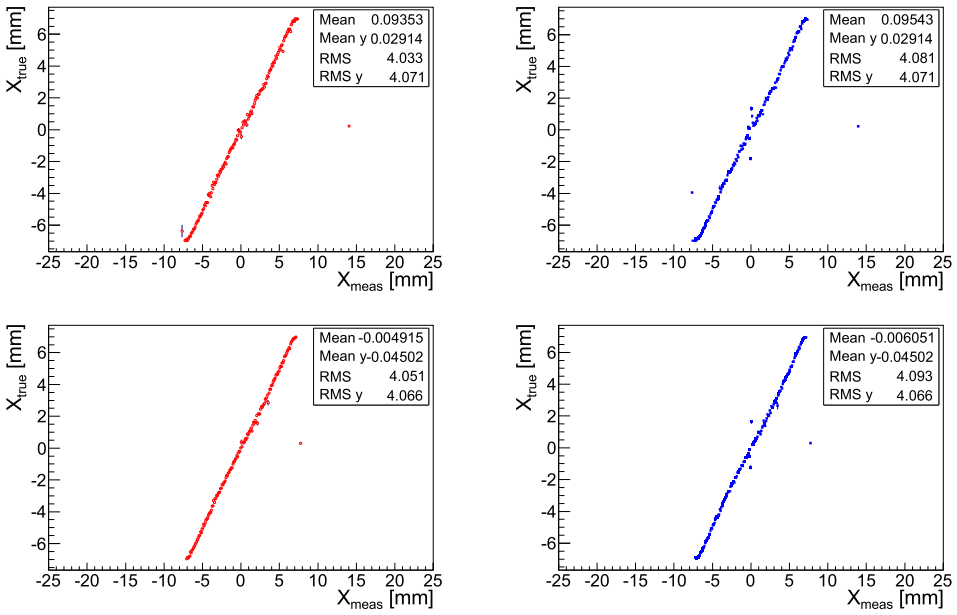

Figure 6.14: 2-D distribution of x_{true} versus x_{meas} for photons of energy 50 GeV and 150 GeV when log weights are used to estimate the COG as given in Equation 6.9. The left (right) figures refer to cases when combined (individual) fiber information is used.

For this analysis, linear weights are used to estimate the position of COG. These S-shape curves are then fitted with a function of the form

$$\begin{aligned} x_{true} &= P_0 \times \tan^{-1}\left(P_1 \times (x_{meas} - P_2)\right) + P_3 \times (x_{meas} - P_2) \\ y_{true} &= P_4 \times \tan^{-1}\left(P_5 \times (y_{meas} - P_6)\right) + P_7 \times (y_{meas} - P_6) \end{aligned} \tag{6.10}$$

Figures 6.12 and 6.13 show how the fitted functions for X and Y look like for 50 GeV and 150 GeV photons. Using these fitted functions, the x_{meas} (y_{meas}) are corrected so that the measured position coordinates are nearer to the true ones, i.e., x_{true} (y_{true}). Fitted parameters differ slightly depending on the energy of the photon. For simplicity fitted parameters from 50 GeV photons are used to fit all energy particles

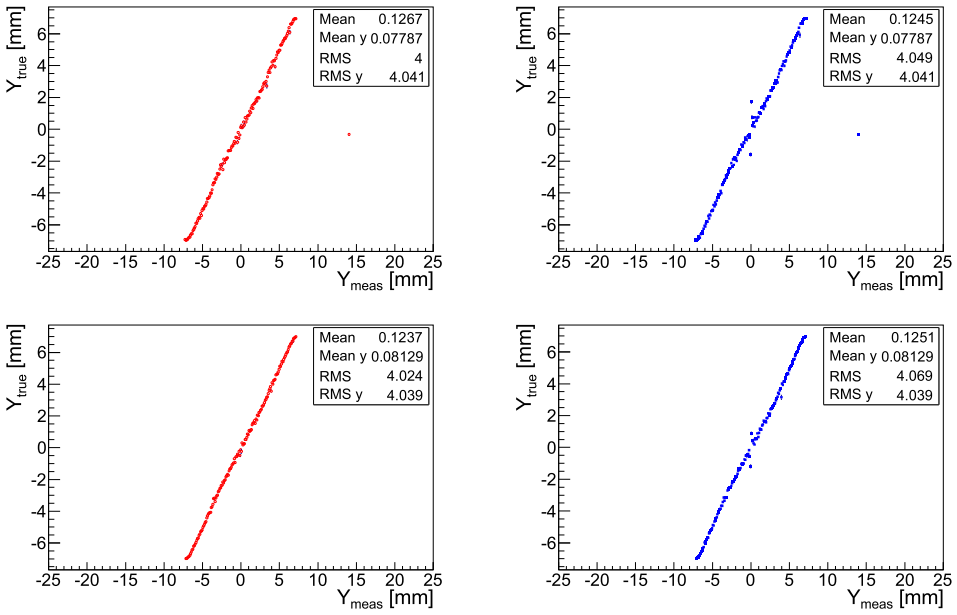

Figure 6.15: 2-D distribution of y_{true} versus y_{meas} for photons of energy 50 GeV and 150 GeV when log weights are used to estimate the COG as given in Equation 6.9. The left (right) figures refer to cases when combined (individual) fiber information is used.

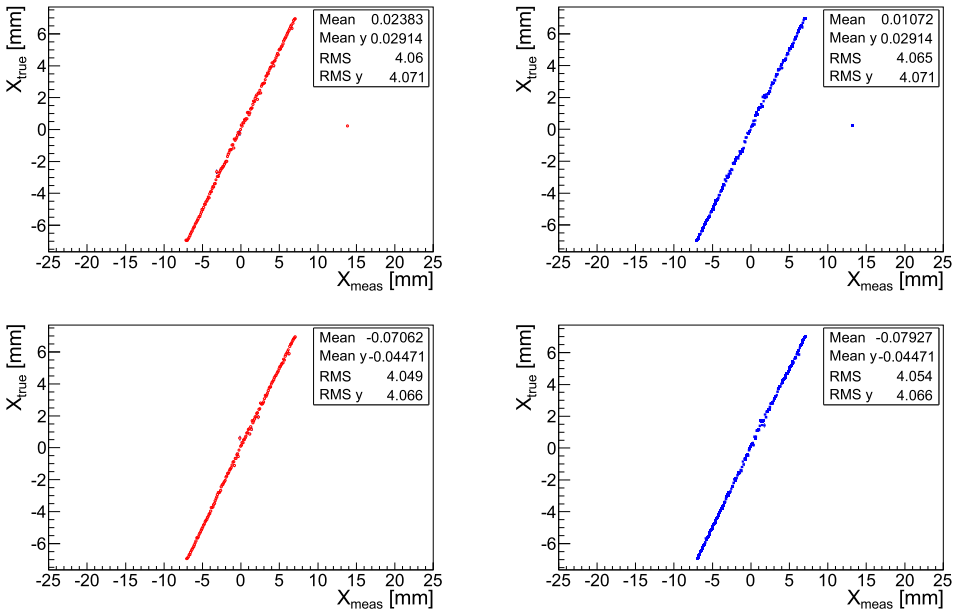

Figure 6.16: 2-D distributions of x_{true} versus S-shape corrected x_{meas} for photons of energy 50 GeV (top) and 150 GeV (bottom) when linear weights are used to estimate the COG as given in Equation 6.8. The left (right) figures refer to cases when combined (individual) fiber information is used.

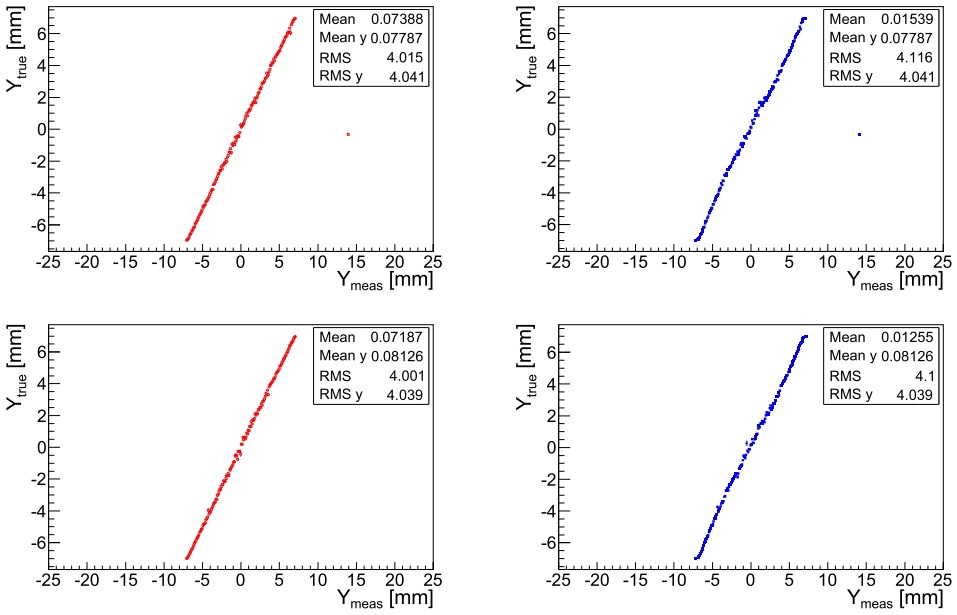

Figure 6.17: 2-D distributions of y_{true} versus S-shape corrected y_{meas} for photons of energy 50 GeV (top) and 150 GeV (bottom) when linear weights are used to estimate the COG as given in Equation 6.8. The left (right) figures refer to cases when combined (individual) fiber information is used.

and to obtain S-shape corrected $\overline{x}$ and $\overline{y}$. These S-shaped corrected positions are then used in Equation 6.12 as $\overline{x}$ and $\overline{y}$. Figure 6.16 shows the S-shape corrected X position of 50 GeV and 150 GeV photons for both the cases of combined and individual fiber information. Similarly, Figure 6.17 shows the S-shape corrected Y position of 50 GeV and 150 GeV photons.

Position resolution is studied from samples of photons produced with impact points randomly distributed on the front face of the module. The difference between the true and measured position along X and Y directions are plotted. These distributions follow roughly a Gaussian shape. The RMS of these distributions is used to estimate the position resolution of these photons. Figure 6.18 shows position resolution as a function of photon energy for three different scenario: (a) position with linear weighting in energy; (b) S-shape corrected position with linear weighting in energy; and (c) position with logarithmic weighting. Position resolution improves

as a function of the photon energy in all three cases.

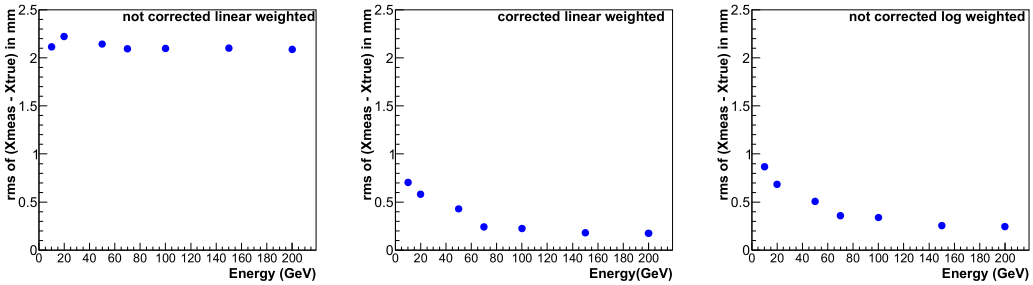

Figure 6.18: Position resolution for photons in a Shashlik detector as a function of photon energy with position reconstructed using linear weighting in energy (a); S-shape corrected position with linear weighting in energy (b); and position with logarithmic weighting (c).

Position resolution is quite large and is related to the lateral size of the tower if one simply uses linear weighting in energy in determining the impact point and without any further correction. With S-shape correction, the resolution improves significantly. The resolution is 0.70 mm for photons at 10 GeV and it improves with energy becoming 0.22 mm at 200 GeV. Logarithmic weighting takes care of the correction to some extent and even without any further correction the resolution is 0.87 mm at 10 GeV and 0.34 mm at 200 GeV. A precise measurement of the impact position is extremely useful for π^0/γ separation.

6.1.4 π^0/γ Separation

An important measure of the performance of an electromagnetic calorimeter used in a high energy physics experiment is its ability to separate between photons and π^0s. In high energy collisions any final state with photons has a background contribution from jets which fake photons. This is because π^0's in jets decay to 2γ's almost 99.9% of the time. For decays of a high energy π^0, the angle between the two photons can become comparable with or smaller than the granularity of the calorimeter. It is very difficult to separate the photons from such a decay from photons which are

coming either from the interaction vertex or from radiation off charged leptons.

In this study, the idea of exploiting the information from the four fibers for π^0/γ separation has been investigated. The idea behind using information from all the four fibers individually is that a larger fraction of the deposited energy from a single photon will be collected by the fiber which is closest to the impact point, while π^0, decaying to a pair of photons will have two impact points on the Shashlik detector and the sharing of light among the fibers will significantly increase.

6.1.4.1 Shower Shapes

In general, the lateral shower profile tends to be broader for photons coming from π^0 compared to that of prompt photons. This holds true for lower energy π^0's (less than 100 GeV). Therefore shower shape variables are useful for discriminating between π^0's and photons. For all shower shape variables, the tower with maximum energy deposit is first identified and then the shape parameters are formed around it. The following shape variables are considered:

$S1/S9$: This ratio makes use of $S1$, the maximum energy deposited in a tower, and $S9$, the energy deposited in 3×3 array around the maximum energy deposited tower. Figure 6.19 shows the array of 3×3 towers formed around the maximum energy deposited tower and the distribution of $S1/S9$ for 50 GeV, 70 GeV and 150 GeV photons and π^0's.

$S1/S4$: This ratio uses $S4$, the energy deposited in 2×2 array including the maximum energy tower. Four possible 2×2 arrays are possible which include the maximum energy tower. The combination which corresponds to the largest sum total energy is used in determining the ratio. Figure 6.20 shows the four possible combinations of 2×2 array of towers and the distributions of $S1/S4$ for 50, 70 and 150 GeV photons and π^0's.

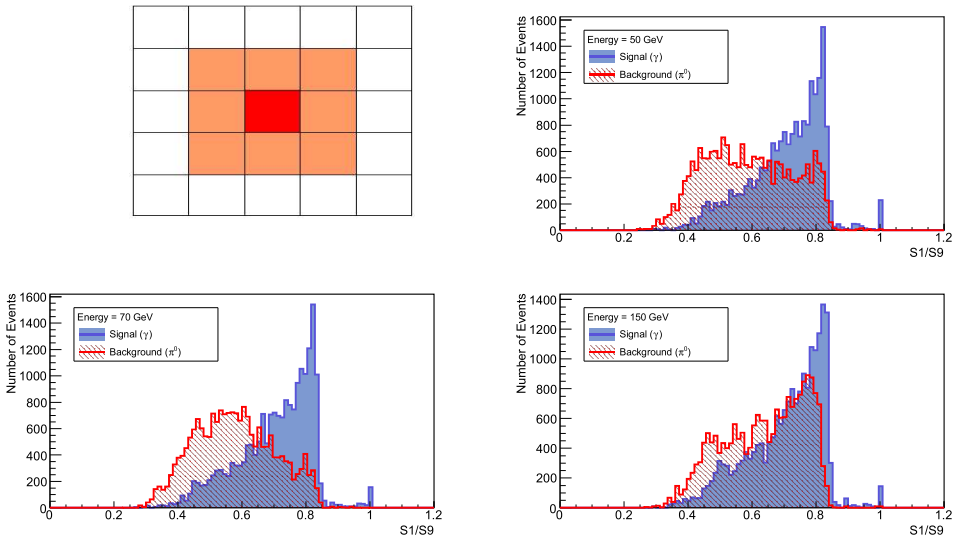

Figure 6.19: The top left diagram shows 3×3 array of towers in light orange color and the maximum energy deposited tower in red color. The top-right figure shows the distribution of S1/S9 for 50 GeV photons and π^0's. Similar distribution for 70 GeV photons and π^0's is on the bottom left; and 150 GeV photons and π^0's is on the bottom right. The blue hatched histogram is for photons and the red hatched histogram is for π^0's [123].

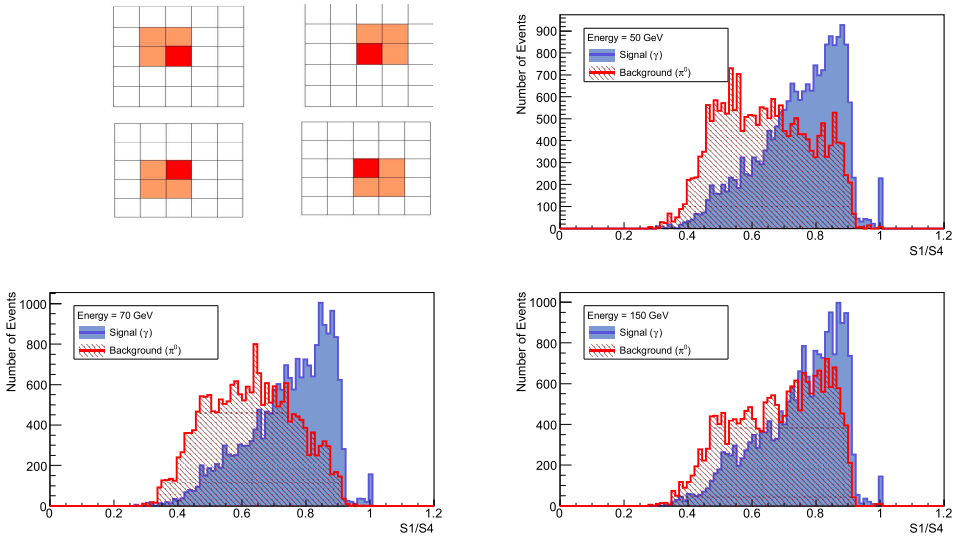

Figure 6.20: The top left diagram shows the four possible combinations of 2×2 arrays which can be formed including the maximum energy tower. The top right figure shows the distribution of S1/S4 variable for 50 GeV photons and π^0's. The bottom left and right plots correspond to 70 GeV and 150 GeV photons and π^0's. The blue hatched histogram is for photons and the red hatched histogram is for π^0's [123].

2-D distribution of F_{16} vs F_9: The variables, F_9 and F_{16}, are defined through equation 6.11.

$$\begin{aligned} F_9 &= \frac{S9 - S1}{S9} \\ F_{16} &= \frac{S16 - S4}{S16} \end{aligned} \tag{6.11}$$

where $S16$ is the energy deposited in the 4×4 array of towers that is centered on the 2×2 array of towers with the maximum energy, among the four possible combinations as explained above. Figure 6.21 shows the diagrammatic view of 4×4 array of towers around the 2×2 array of towers and the 2-D distribution of F_{16} and F_9 for 50, 70 and 150 GeV photons and π^0's.

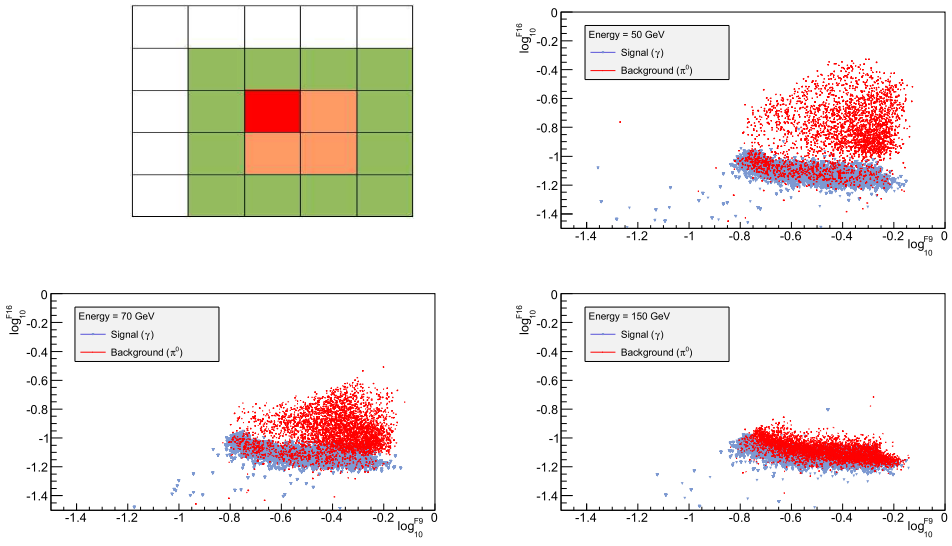

Figure 6.21: The top left diagram shows the 4×4 arrays of towers formed around that array of 2×2 towers which has maximum energy of the four possible combinations as explained in the text. The top-right plot shows the 2-D distribution of F_{16} along the Y axis and F_9 along the X axis for 50 GeV photons and π^0's. Similar plots at 70 GeV and 150 GeV are at the bottom left and at the bottom right respectively. The blue points are for photons and the red points are for π^0's [123].

The performance of the variables $S1/S9$, $S1/S4$ and F_{16} vs F_9 are summarized below:

- Shower shape variables $S1/S9$ and $S1/S4$ lose the sensitivity for γ/π^0 separation at energies above 70 GeV;
- The 2-D distribution of F_{16} vs F_9 performs better for 70 GeV γ/π^0 discrimination compared to $S1/S9$ and $S1/S4$. But again it loses power for discrimination at energies above 70 GeV.

6.1.4.2 Moment Analysis

This analysis is based on the consideration that when the π^0 decays to two γ's, the shower tends to be elliptical, as shown in Figure 6.22, whereas for a prompt photon the spread in X and Y will tend to be similar, because the shower spreads uniformly in all the directions. The above holds true for photons not converted before they reach the front face of the tower and when there is no magnetic field. Early conversion and passage through magnetic field make the decay topology more complicated.

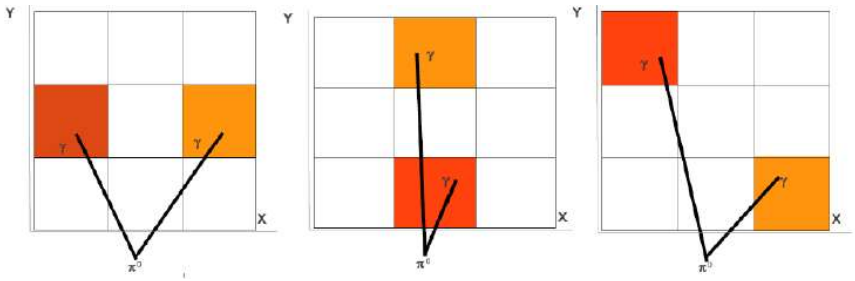

Figure 6.22: Diagram showing three different topologies of a π^0 decay.

The ratio of major axis of the ellipse to its minor axis or vice-versa is utilized to distinguish between photons and π^0's. For π^0's, the ratio between the two axes is expected to be away from 1, whereas, for photons, it is expected to be close to 1. To get the values of the length of both of the axis of the shower, a covariance matrix can be formed with the quantities as given in Equation 6.12. The eigenvalues of this matrix is related to the length of the shower axis. The spread is calculated from the point of impact of the photon or the π^0. The point of impact is estimated using the

COG method and correcting for the S-shape as discussed in Section 6.1.3. The 2×2 matrix is formed in each event as follows:

$$M = \begin{vmatrix} \sigma_x^2 & \sigma_{xy}^2 \\ \sigma_{xy}^2 & \sigma_y^2 \end{vmatrix}$$

The definition of each of the terms of the above matrix is given below

$$\begin{aligned} \sigma_x^2 &= \Sigma(x_i - \overline{x})^2 \times w_i/\Sigma w_i \\ \sigma_y^2 &= \Sigma(y_i - \overline{y})^2 \times w_i/\Sigma w_i \\ \sigma_{xy}^2 &= \Sigma(x_i - \overline{x}) \times (y_i - \overline{y}) \times w_i/\Sigma w_i, \end{aligned} \tag{6.12}$$

where $\overline{x}$ and $\overline{y}$ are the S-shape corrected Center of Gravity (COG) positions of the shower in X and Y, and w_i are the weights associated with each contribution. This matrix is then diagonalized to extract the eigenvalues, λ_+ and λ_-. The ratio of eigenvalues of this matrix, λ_-/λ_+ or λ_+/λ_- measures the eccentricity of the energy distribution and is used to discriminate direct γ from π^0.

There are two ways in which the weights, w_i are formed:

Linear weights, w_i: Here the weights, w_i are given by Equation 6.13:

$$\begin{aligned} x_{meas} &= \Sigma x_i \times w_i, \\ y_{meas} &= \Sigma y_i \times w_i, \\ w_i &= E_i/\Sigma E_i. \end{aligned} \tag{6.13}$$

Logarithmic weights, w_i: In this case, the weights, w_i are given by the Equation

6.14

$$\begin{aligned} x_{meas} &= \Sigma x_i \times w_i/\Sigma w_i, \\ y_{meas} &= \Sigma y_i \times w_i/\Sigma w_i, \\ w_i &= Max(0, w_0 + \ln(E_i/E_T)), \end{aligned} \tag{6.14}$$

where w_0 is related to the threshold for the towers below which the towers are not included in the sum, and E_T is the total energy deposited in the array.

There are two ways in which the covariance matrix can be constructed:

1. use combined information of all four fibers in a given tower [Coarse grain information];
2. use information from individual fiber in a given tower [Fine grain information].

6.1.4.2.1 Coarse grain Information In this case, E_i refers to the total energy recorded by i^{th} tower (i=1-9 for 3×3 array) and x_i and y_i are the X and Y coordinates of the center of i^{th} tower. E_i is obtained by summing the energy recorded from all four fibers of the i^{th} tower. Both linear and log weights are used in the determination of the impact point. In case of log weights, w_0 is set to be 4.7. Figures 6.23, 6.24 and 6.25 show the ratio of λ_-/λ_+ for photons and π^0's at 50 GeV, 70 GeV and 150 GeV. These plots clearly demonstrate that log weights improve the discriminating power between photons and π^0's over linear weights.

6.1.4.2.2 Fine grain information For fine grain information E_i refers to the energy recorded by i^{th} individual fiber (i=1-36 for 3 × 3 array) and x_i and y_i are the X and Y coordinates of the i^{th} fiber. The impact point is determined with both linear weights and log weights. A comparison between the two methods using photons and π^0's of 50 GeV, 70 GeV and 150 GeV indicates a higher discriminating

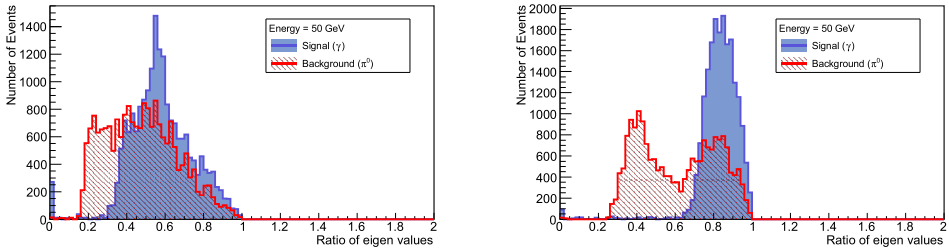

Figure 6.23: Distribution of λ_-/λ_+ for photons and π^0's of 50 GeV for the case of coarse grain information (no information from individual fibers used). The plot on the left is done with linear weights for determining the impact point while the plot on the right is done with the log weights.

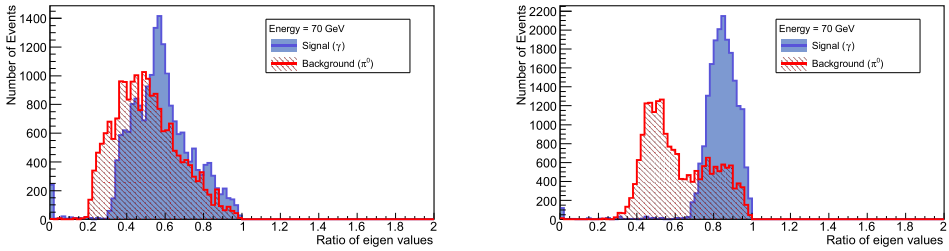

Figure 6.24: Distribution of λ_-/λ_+ for photons and π^0's of 70 GeV for the case of coarse grain information (no information from individual fibers used). The plot on the left is done with linear weights for determining the impact point while the plot on the right utilizes log weights.

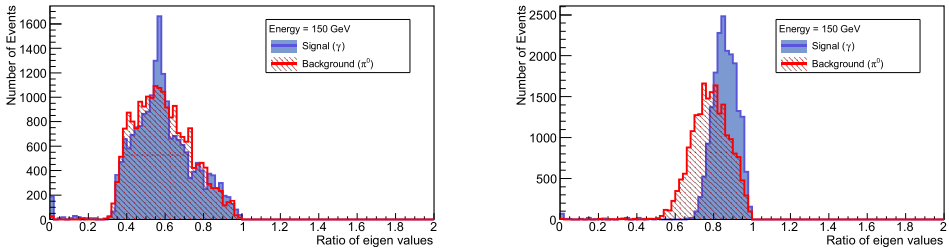

Figure 6.25: Distribution of λ_-/λ_+ for photons and π^0's of 150 GeV for the case of coarse grain information (no information from individual fibers used). The plot on the left is done with linear weights for determining the impact point while the plot on the right utilizes log weights.

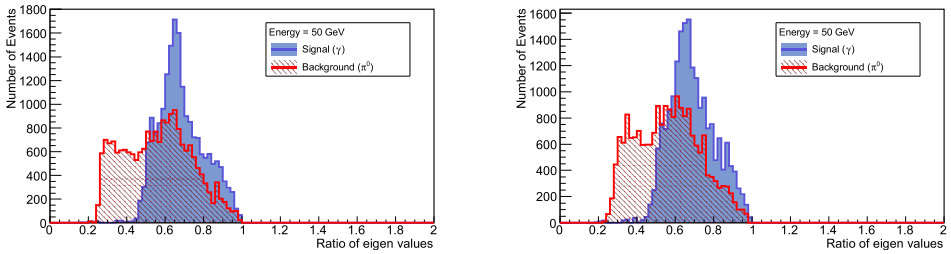

Figure 6.26: Distribution of λ_-/λ_+ for photons and π^0's of 50 GeV for the case of fine grain information (information from individual fibers used). The plot on the left is done with linear weights for determining the impact point while the plot on the right utilizes log weights.

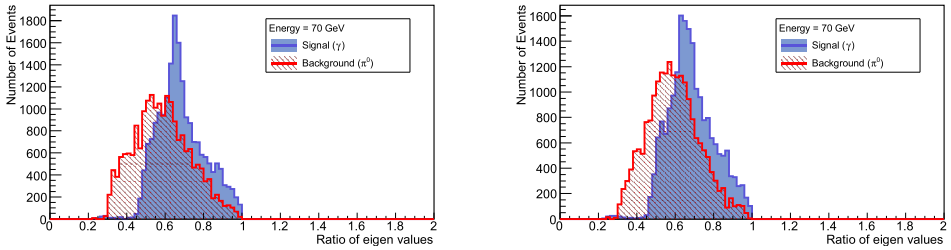

Figure 6.27: Distribution of λ_-/λ_+ for photons and π^0's of 70 GeV for the case of fine grain information (information from individual fibers used). The plot on the left is done with linear weights for determining the impact point while the plot on the right utilizes log weights.

power of the log weights. By comparing the set of plots with fine grain information in Figure 6.26, 6.27 and 6.28 with the corresponding plots for coarse grain information, it can be seen that not much additional sensitivity is added in the discriminating power by using information from individual fibers. Beyond 150 GeV, both the ways (coarse grain information and fine grain information) fail to discriminate between photons and π^0's.

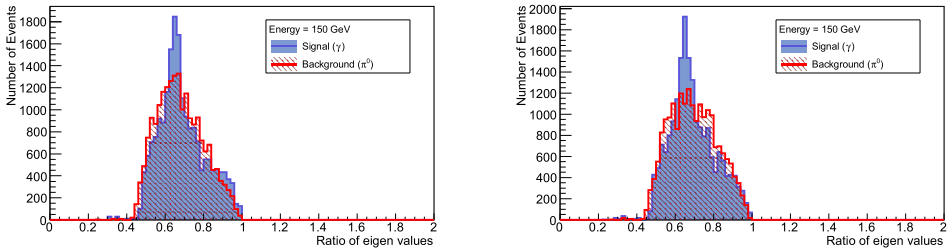

Figure 6.28: Distribution of λ_-/λ_+ for photons and π^0's of 150 GeV for the case of fine grain information (information from individual fibers used). The plot on the left is done with linear weights for determining the impact point while the plot on the right utilizes log weights.

6.1.4.3 Study using Multivariate Analysis (MVA)

As it has been described in the previous Sections, 6.2.4, 6.1.4.2.1 and 6.1.4.2.2, the discriminating power is reduced significantly for π^0's of energy above 100 GeV. An analysis has been carried out exploring the discriminating power gained by employing multivariate techniques to the problem of separating π^0s from photons using the spatial pattern of energy deposition in the ECAL. In this analysis, the classification problem is to separate π^0's from prompt photons. The following MVA classifiers are examined in this analysis:

1. Boosted Decision Tree (BDT)
2. Gradient Boosted Decision Trees (GBDT)
3. Artificial Neural Network (ANN)

In this analysis, the TMVA [124] package within ROOT [98] is used. Each MVA is trained separately on a sample of photons and π^0's. Energy from each individual tower in 3×3 array, or energy from each fiber in the 3×3 array is fed into the MVA. This analysis is done using photons and π^0's at 200 GeV. Two types of samples are produced:

Fixed gun sample: These are produced with the gun position fixed at (0 mm, 4 cm) in (x, y), with z at 3.2 m.

Random gun sample: In this case, the gun positions are uniformly distributed both in X and Y direction between −7 mm and +7 mm i.e. within the central tower.

6.1.4.3.1 Training and testing of the MVA using fixed gun samples The MVA is trained using 20000 events from fixed gun samples of 200 GeV photons and π^0's. The following two sets of training variables are used separately to train MVA:

Coarse grain information: Input to MVA is the ratio of energy from each tower in the 3×3 array to total energy in 3×3 array.

Fine grain information: Input to MVA is the ratio of energy from each individual fiber in 3×3 array to total energy in 3×3 array.

These energies are scaled to the total energy collected in the 3×3 array. Figure 6.29 shows the output response of the different MVA classifier for the case of both coarse grain and fine grain information. Figure 6.30 shows the background rejection versus signal efficiency curve for the case of coarse grain as well as fine grain information. It can be seen from the Figures 6.29 and 6.30, that the fine grain information is better for discriminating signal from background.

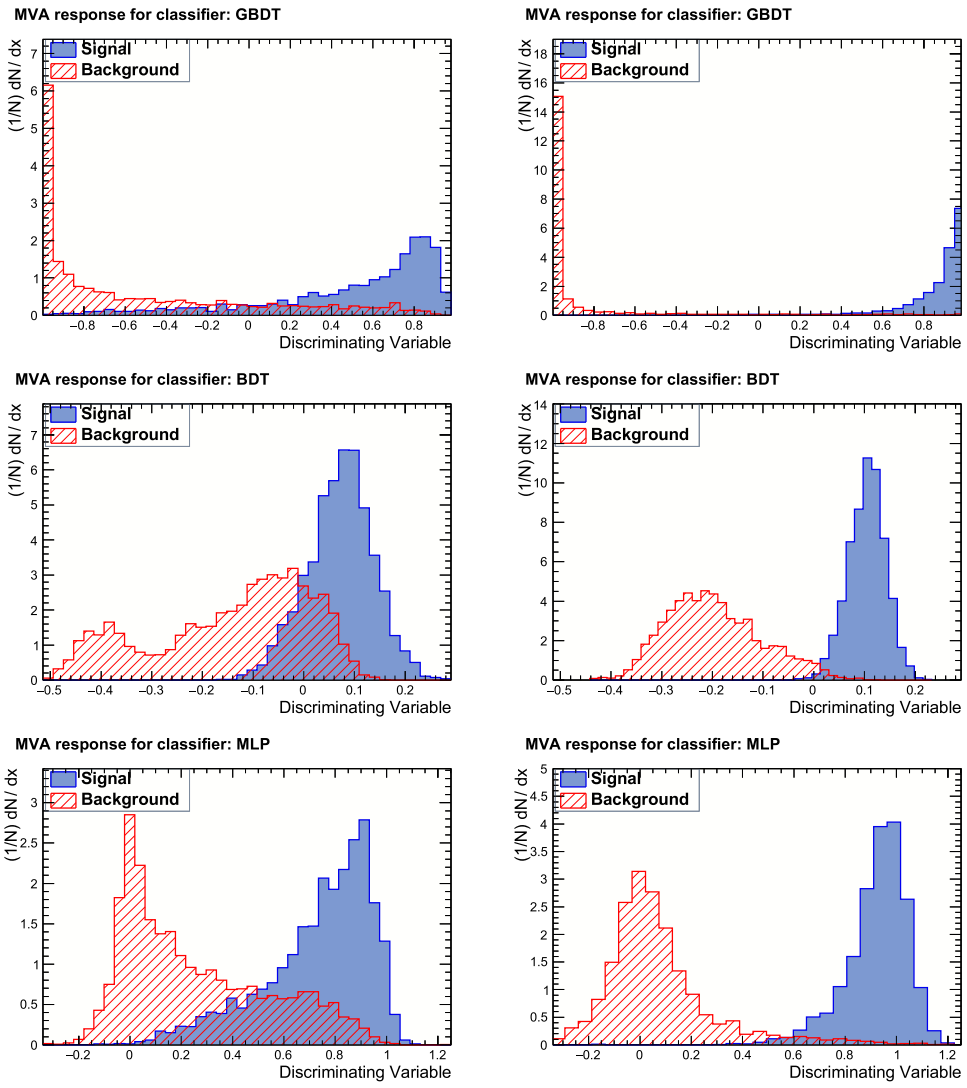

Figure 6.29: The output response of different MVA methods for fixed gun sample. The figures on the left are for coarse grain information and those on the right refer to fine grain information.

6.1.4.3.2 Training and testing of the MVA using random gun samples

In a realistic scenario a particle can hit anywhere on the face of a tower. Keeping this in mind a training is done on a sample of 20000 photons and π^0s of energy 200 GeV from random gun sources. The hit positions of the photons and π^0's are uniformly distributed in X and Y direction between -7 mm and $+7$ mm. Two different samples are used to train the MVA:

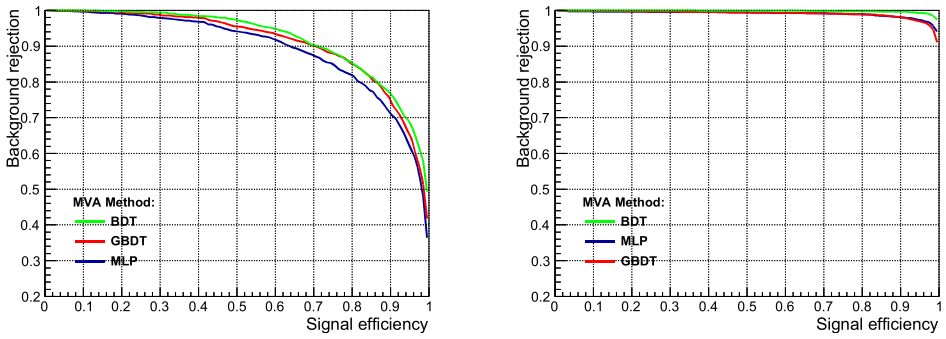

Figure 6.30: The background rejection versus the signal efficiency curve for various MVA methods using fixed gun sample. Left figure for coarse grain information and the figure on the right for fine grain information [123].

Unbinned random sample: In this case the event sample is produced over entire face of the central tower. Figure 6.31 shows the output response of the different MVA classifiers for the case of both coarse grain and fine grain information. Figure 6.32 shows the background rejection versus signal efficiency curve for the case of coarse grain as well as fine grain information using random gun sample. It can be seen from the Figures 6.31 and 6.32, that the fine grain information improves the discrimination for the case of random gun sample also.

Binned random sample: The energy deposit pattern in the matrix of Shashlik towers can vary considerably based on the location of the hit on the central tower. To take into account the dependence of the energy deposit pattern on the hit location, a hit location based MVA training is used, to further improve the separation power of the MVA. For this the central tower is divided into 7×7 matrix of virtual square regions (or virtual cells) each of dimension 2mm×2mm. Event samples are produced in each virtual cell independently. 49 separate trainings are done to obtain 49 separate trees (or networks) - one for each virtual cell. At the time of testing/using the MVA, the tree to be used is chosen using the information of the measured hit position.

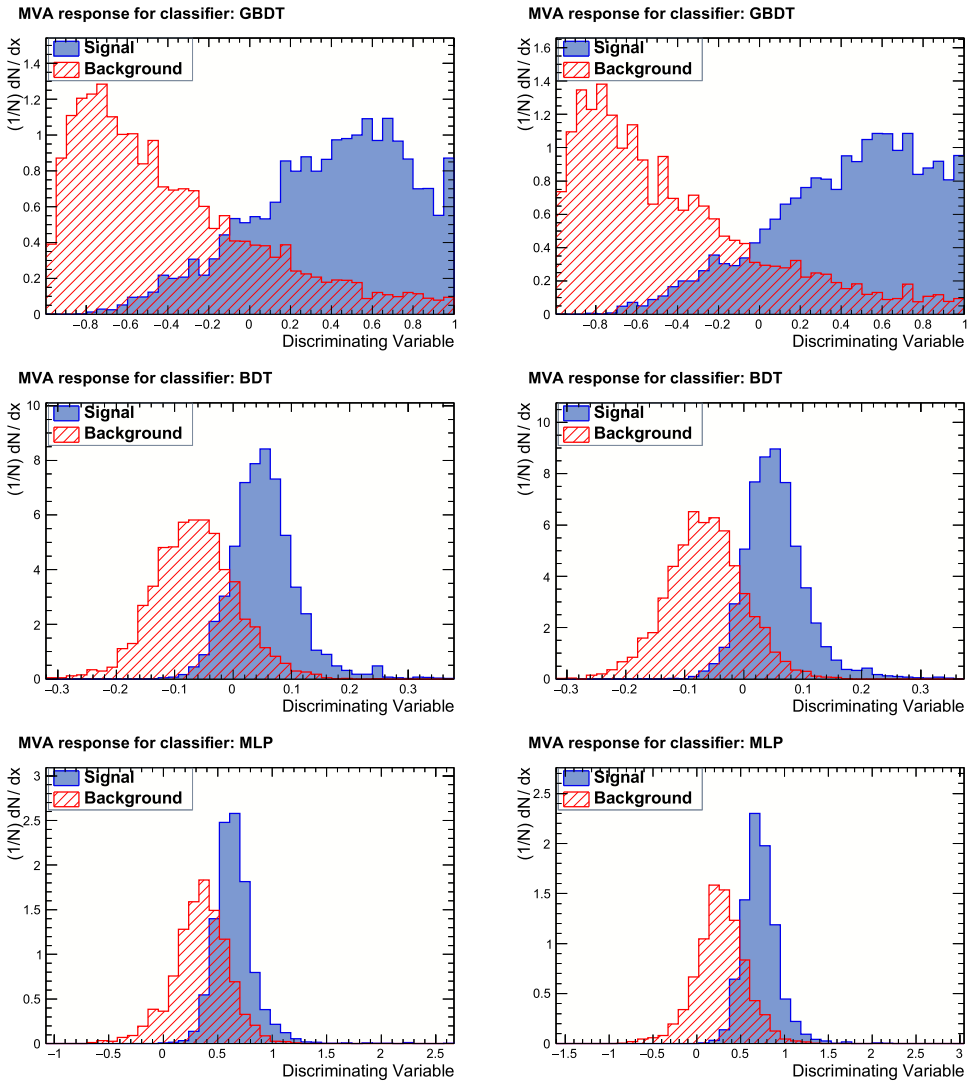

Figure 6.31: The output response of different MVA methods for unbinned random gun sample. The figures on the left are for coarse grain information and those on the right refer to fine grain information.

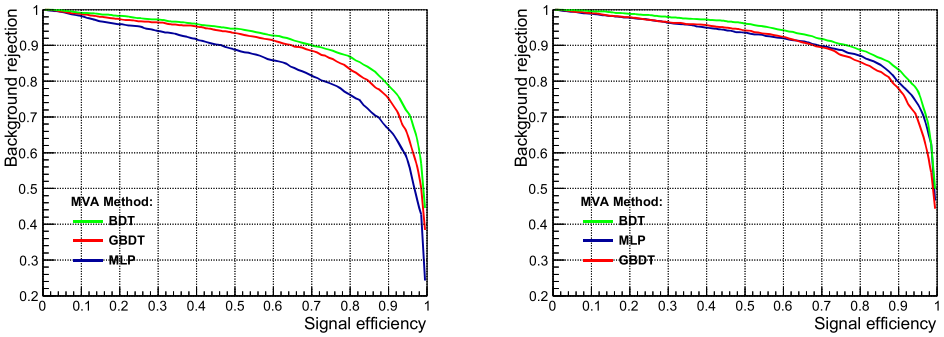

Figure 6.32: The background rejection versus the signal efficiency curve for various MVA methods using unbinned random gun sample. Left figure for coarse grain information and the figure on the right for fine grain information [123].

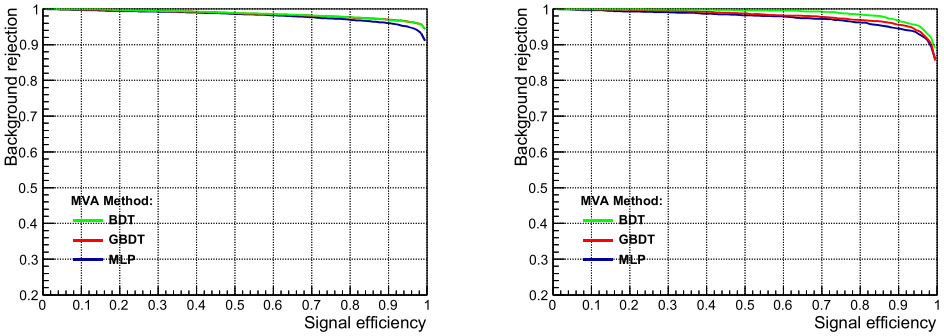

Figure 6.33: Background rejection versus signal efficiency of two virtual cells for the case of binned random samples. The left figure is for a virtual cell where the sample is randomized over a region from +3 mm to +5 mm in both X and Y direction and the right figure is for a region from −1 mm to +1 mm in the X direction and +3 mm to +5 mm in the Y direction with respect to the centre of the central tower [123].

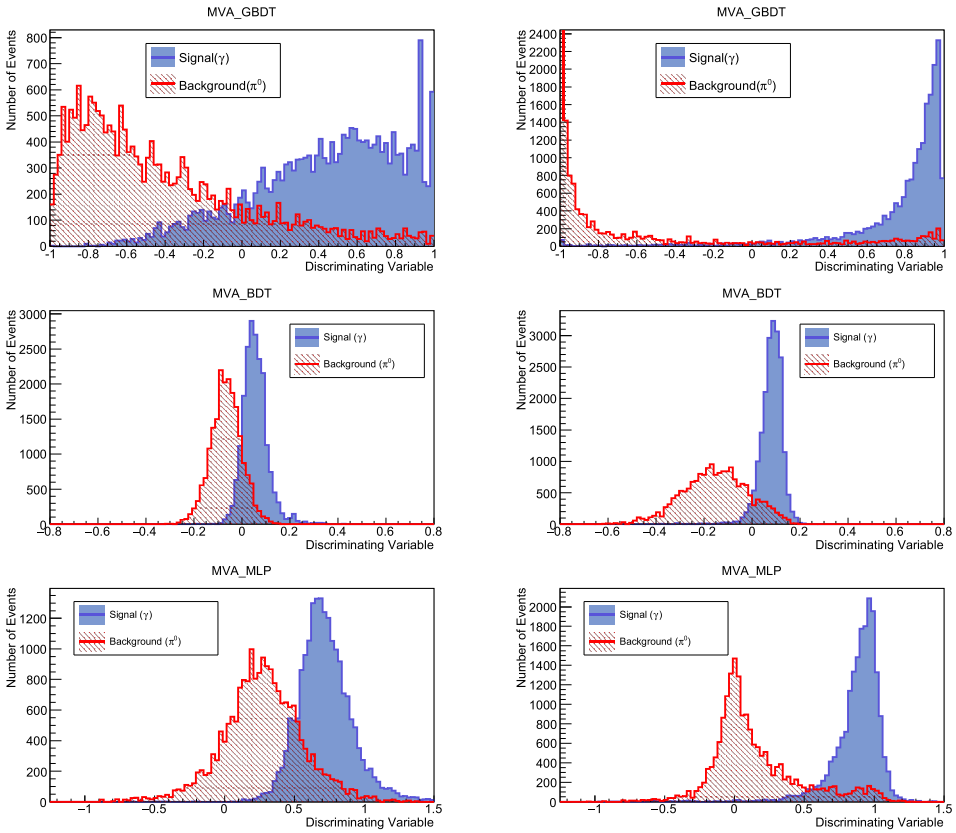

Figure 6.34: The output response of different MVA methods. The figures on the left show the response from the MVA trained with unbinned sample and the ones on the right are for the MVA trained with binned sample.

Figure 6.33 shows background rejection versus signal efficiency plots for binned random sample. Figure 6.34 shows the output response of both the MVA methods, namely the MVA trained with unbinned samples and the MVAs trained with binned training samples. For both the cases, the same test sample is used.

6.1.4.4 Comparison of Various Methods

A comparison in performance is made among all the methods described in the previous sections. This comparison is shown for 200 GeV photons and π^0's.

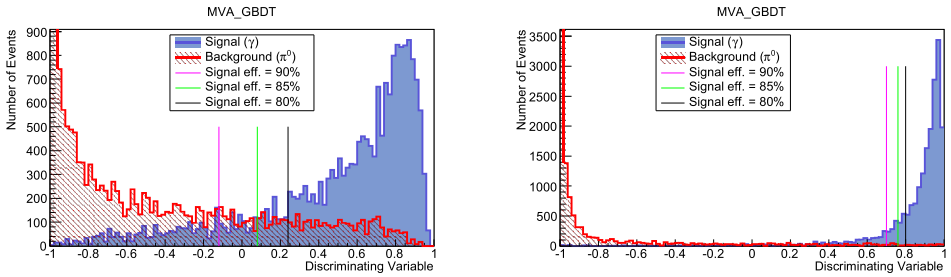

Figure 6.35: MVA response for 200 GeV photons and π^0's. The plots on the left refers to GBDT training with coarse grain information and the plots on the right makes use of GBDT algorithm trained with fine grain information, using fixed gun sample for (x,y):(0.0 mm, 4.0 mm). The black, blue and pink lines show the point where the cut is applied to achieve 80%, 85% and 90% signal efficiency (events falling on the right side of the line are selected).

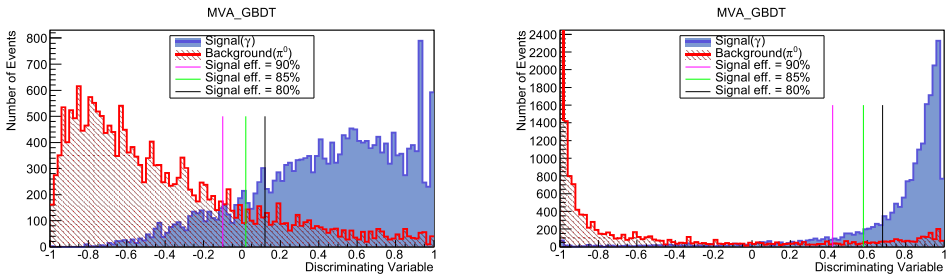

Figure 6.36: Comparison of GBDT MVA method for 200 GeV photons and π^0's. The plots in the left refers to GBDT training with unbinned sample and the plots on the right makes use of GBDT algorithm trained with binned sample. The black, green and pink lines are the point where the cut is applied to achieve 80%, 85% and 90% signal efficiency respectively [123].

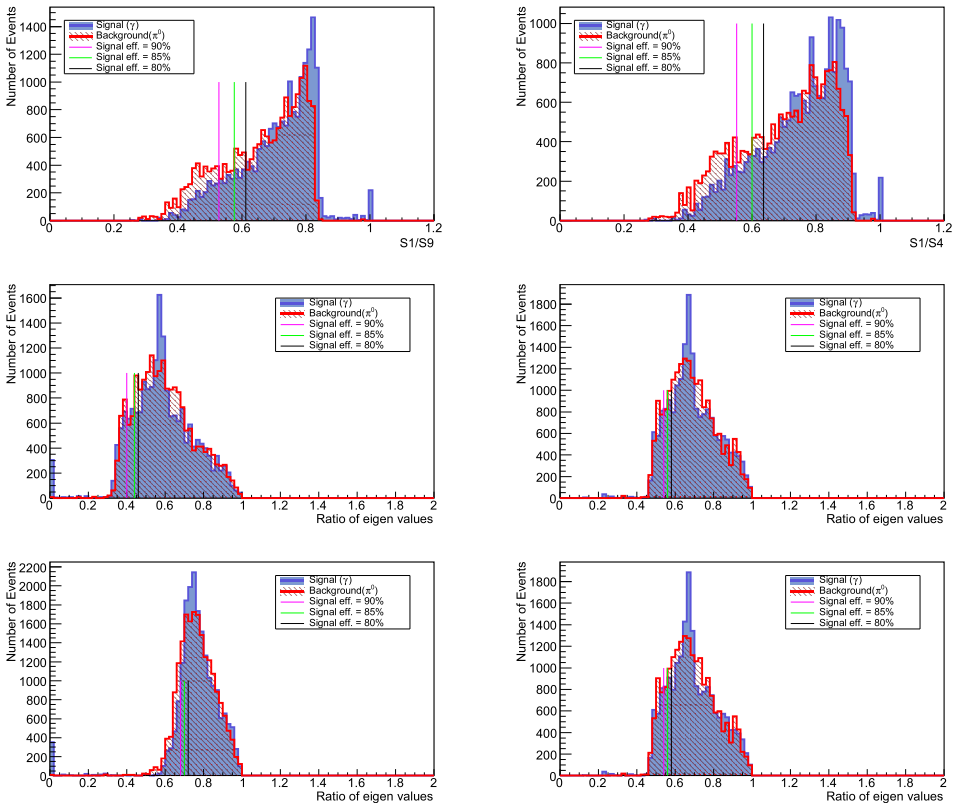

Figure 6.37: Distributions for 200 GeV photons and π^0's of (a) $S1/S9$ on the top left; (b) $S1/S4$ on the top right; (c) ratio of eigenvalues using coarse grain information and linear weights on the middle left; (d) ratio of eigenvalues using fine grain information and linear weights on the middle right; (e) ratio of eigenvalues using coarse grain information and log weights on the bottom left; (f) ratio of eigenvalues using fine grain information and log weights on the bottom right. The black line shows the point where the cut is applied to achieve 80% signal efficiency, blue line for 85% signal efficiency and the pink line for 90% signal efficiency.

Variable	Background rejection (%)		
	ϵ_{signal}=80%	ϵ_{signal}=85%	ϵ_{signal}=90%
S1/S9	33.2	27.7	21.2
S1/S4	32.7	26.8	20.1
Linear weights: Ratio of eigenvalues (coarse grain)	21.1	15.3	9.6
Linear weights: Ratio of eigenvalues (fine grain)	23.0	18.9	12.2
Logarithmic weights: Ratio of eigenvalues (coarse grain)	41.1	36.9	32.3
Logarithmic weights: Ratio of eigenvalues (fine grain)	23.1	18.4	13.2
MVA(GBDT): coarse grain (fixed gun sample)	86.3	82.0	76.5
MVA(GBDT): fine grain (fixed gun sample)	99.1	99.0	98.5
MVA(GBDT): fine grain (unbinned random gun sample)	86.3	83.3	78.9
MVA(GBDT): fine grain (binned random gun sample)	92.3	91.0	89.3

Table 6.3: Table showing the background rejection for signal efficiencies of 80%, 85% and 90% for various methods. This is shown for energy point of 200 GeV [123].

If a method shows good separation power for this high energy point, then it is good for lower energy points as well.

BDT gives the best response for the case of both coarse grain and fine grain information as can be seen from the Figures 6.30,6.32 and 6.33. The response of BDTG and BDT are similar. Here the comparison is made using the BDTG.

Table 6.3 shows the background rejection for all the various methods for a signal efficiencies of 80%, 85% and 90%.

6.1.5 Summary

The energy resolution of the Shashlik detector is dominated by the sampling fluctuation which contributes to the stochastic term. The constant term is found to be better than 1% while the stochastic term is found to be $10.3\%/\sqrt{E}$ for light yield value of 4000 p.e./MeV. The energy resolution is found to be similar for lead/LYSO and tungsten/LYSO configurations and the optimum number of layers is found to be 28 which corresponds to ∼25 radiation lengths deep detector. For 125 GeV Higgs boson decaying to a pair of photon, this detector will achieve a mass resolution of 0.64 GeV when both the photons are detected in the Shashlik detector.

The position resolution using information of the Shashlik detector alone is 2.0 mm for photons of 100 GeV. The resolution improves with energy of the photon and a better resolution is obtained when the center of gravity method uses logarithmic weighting (to 0.34 mm) or a correction is made for the S-shape (to 0.22 mm).

A study of the $\pi^0 - \gamma$ separation presented in this thesis shows that the fine grain information of the shower profile collected by individual fibers is useful for separation between π^0 and γ at high energies. With the MVA technique a background rejection efficiency of 90% with signal efficiency 90% was achieved, which is approximately three times better than the best background rejection that could be achieved by

cut-based methods. We proposed a method of virtual slicing of the hit tower and impact point based training of the network, which gives an additional improvement of 8-10%. We conclude that the $\pi^0 - \gamma$ separation power of the Shashlik calorimeter can be improved significantly by employing an MVA based method with fine grain information as input and impact point based training.

6.2 High Granularity Calorimeter

The CMS collaboration has decided to replace its current endcap calorimeters with a new High Granularity Calorimeter (HGCAL). This detector is a sampling calorimeter with silicon and plastic scintillator as the active materials. It includes both electromagnetic (EE) and hadronic (FH, BH) sections. The EE will use lead as the main absorber material and hexagonal silicon sensors as the active detector. The FH and BH will each use stainless steel as absorber and a mixture of silicon and scintillator as detectors. The EE will have 28 layers which corresponds to $\sim 25X_0$ and $\sim 1.3\lambda$.This section describes simulation of beam-test with 16 layers of EE at Fermilab and comparison with test-beam data.

6.2.1 Experimental Configuration

For the construction of the HGCAL EE prototype, hexagonal silicon sensors and readout electronics are assembled into detector modules. Each module is a glued stack comprising a CuW (25%Cu : 75%W) base plate, a polyimide foil, the silicon sensor and a PCB to host the wire bonds down to the sensor. A second PCB is plugged into connectors on this first PCB. Figure 6.38 shows the geometry of the sensors used during the test beam. These sensors are 128 channel hexagonal silicon devices made from 6 inch p-in-n silicon wafers. The physical thickness of these sensors is 320 μm with a depleted thickness of 200 μm. The cells on the sensor, except those on the edges, are hexagonal with an area of ~ 1.1 cm^2.

Sixteen modules, arranged as double-sided layers interspersed with tungsten absorbers, are used in the FNAL test beam setup. The total thickness of the setup is deliberately limited to about 15 X_0 due to the availability of relatively low energy electron beams at FNAL (maximum beam energy being 32 GeV). Figure 6.39 shows

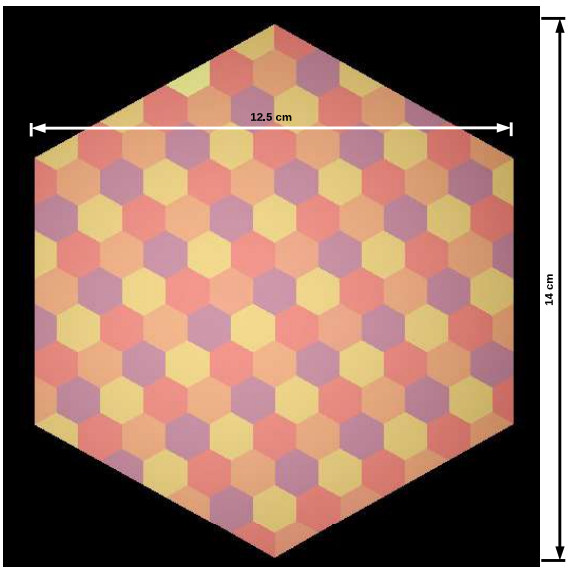

Figure 6.38: Layout of 128-cell hexagonal silicon sensor used in the simulation of test beam setup.

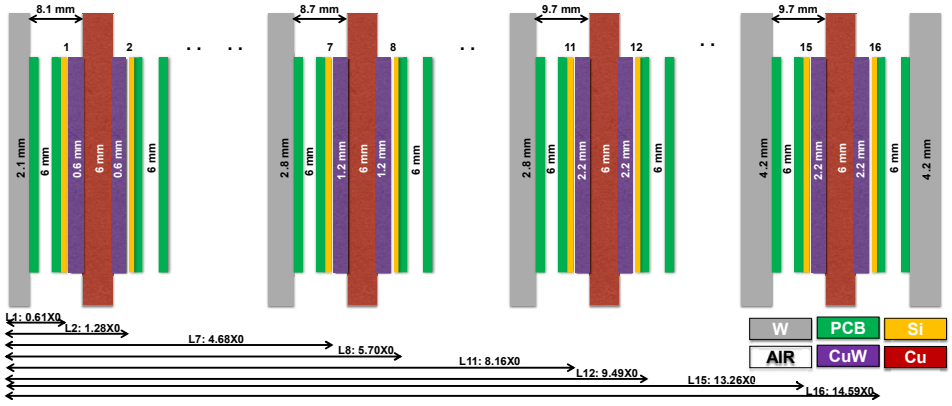

Figure 6.39: The experimental setup used at FNAL: Eight double-sided modules mounted on copper cooling plates, separated by varying thicknesses of tungsten absorbers. The total thickness is just under 15 X_0

a schematic of the FNAL setup.

6.2.2 Data

At FNAL the electron energies range between 4 GeV and 32 GeV, with the purity decreasing with energy to about 10% at the highest energies. Electrons are selected

based on energy deposits in the silicon; the resulting "offline" electron purity, verified with simulation, is estimated to be greater than 97% with 95% pion rejection. The energy spread of the electrons in the beams is 3-5%, from the lowest to the highest energies. In addition to electrons, data are taken with 125 GeV protons. Table 6.4 summarizes the data taken during test beam at each energy/particle data point.

Beams	e^-							p^+
Energy (GeV)	4	6	8	16	20	24	32	120

Table 6.4: Data taken at FNAL in July, 2016

6.2.3 Simulation

The 16 layer HGCAL EE and test beam geometry is simulated with GEANT4 [90, 114] in the framework of the standard CMS software. The materials upstream of the test setup are taken into account as much as possible to the real scenario, especially in the energy scale and transverse spread of incident electrons. The main upstream components are 2 Cerenkov detectors and several scintillation counters, giving a total radiation length of 0.6 X_0 spread over 35 m.

In the hexagonal silicon sensor, only full hexagonal cells and half-hexagon cells are simulated. The mouse-bites at the sensor corners are not simulated and not used in any analysis. As these account for a small area at the edges of the sensors, far away from the bulk of the shower, the impact on performance is negligible. The full and half-hexagonal cells are the only active elements in the simulation.

To be able to mimic the test beam setup as closely as possible, the beam momentum and lateral spreads ($\simeq$ 1% and $\simeq$ 1 cm) are taken from the data and used in the simulation.

Events are simulated with three different physics lists [114]:

- FTFP_BERT_EMM
- QGSP_FTFP_BERT_EML
- QGSP_FTFP_BERT

The closest match comes from the physics list FTFP_BERT_EMM, which is used as default in the CMS simulation program. In simulation, the energy and incidence position of the beam are stored as well as the energy from each "simhit" (raw energy deposit) in the silicon.

6.2.3.1 Purity of the Beam

In the test beam, the contamination of the electron beam with charged pions require special treatment. Although a Cerenkov detector is installed, its efficiency is not well understood so a simulation-driven method is developed, based on the fractional energies deposited by the particles in the calorimeter active layers (silicon). Individual samples of electrons and charged pions are generated for each beam energy. Figure 6.40 (left) shows an example pair of silicon energy spectra for 16 GeV elec-

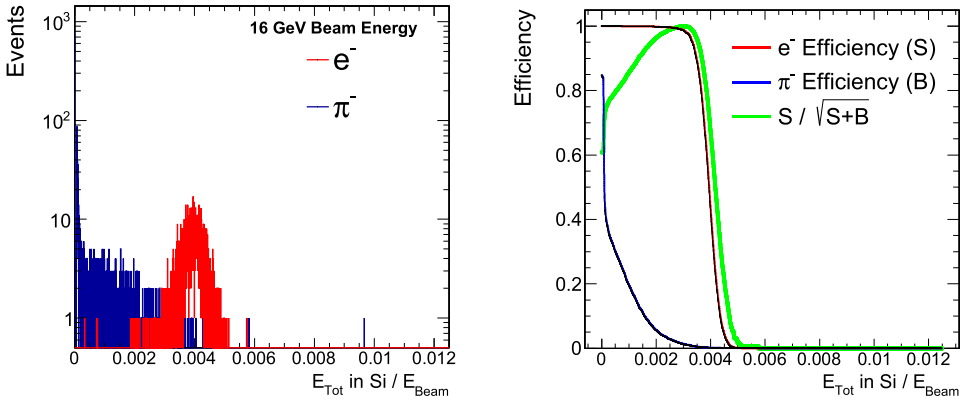

Figure 6.40: Left: the energy deposited in the silicon compared to the beam energy for 16 GeV electrons and pions. Right: The electron and pion efficiencies as functions of this normalized energy. Also shown is the signal strength curve, showing a maximum that is then used as a threshold cut.

trons and pions. A threshold is extracted by maximizing $S/\sqrt{S+B}$, where S is the signal efficiency and B is the background rejection. This is also shown in Figure 6.40 (right) as a function of the energy. The peak in this latter distribution is used to define the threshold for that energy. Using this method, the electron efficiency is always greater than 97% whilst the background rejection was greater than 95%.

6.2.3.2 Energy Deposits: Data vs Simulation

The "standard candle" for silicon sensors is the minimum ionizing particle, "MIP". This is the most-probable energy deposit for a normally-incident minimum-ionizing particle. In reality the MIPs are approximated by incident high-energy hadrons or muons. 125 GeV protons are used in this case. Events are simulated and the most probable energy deposit in the 200 μm active silicon thickness is estimated to be about $\sim$ 52 keV. This value is used when comparing energy deposits in the data and the simulation. Energy deposits in the silicon are expressed in terms of MIPs in the remainder of this chapter.

6.2.4 Longitudinal and Transverse Shower Shapes

One of the main goals of the 2016 HGCAL beam test is to verify the GEANT4 simulation of the complete system, used to evaluate its overall performance and tune the design. One of the key aspects of such simulations, especially for the HGCAL, is the reproduction of the longitudinal and transverse shower shapes for electrons at different energies.

A comparison is made between the data and the simulation based on the FTFP_BERT_EMM physics list which is the default for CMS simulation application.

The evolution of the longitudinal shower profile with energy is shown in Figure 6.41 for the data, as well as for the simulation. The simulation results agree with the

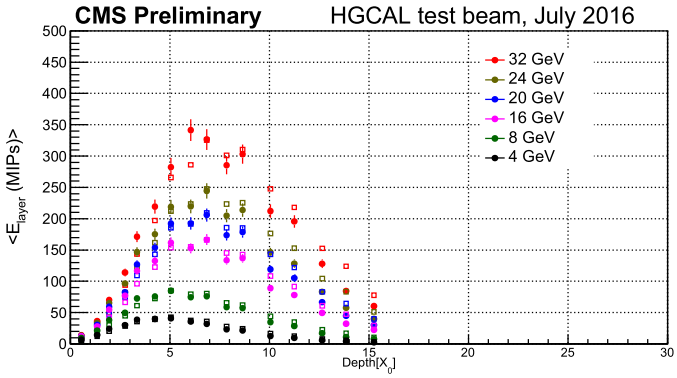

Figure 6.41: Longitudinal shower profile and variation of the shower-maximum position as a function of electron energy: Solid symbols represent data whilst the open symbols are for simulation.

data at a level of better than 10%.

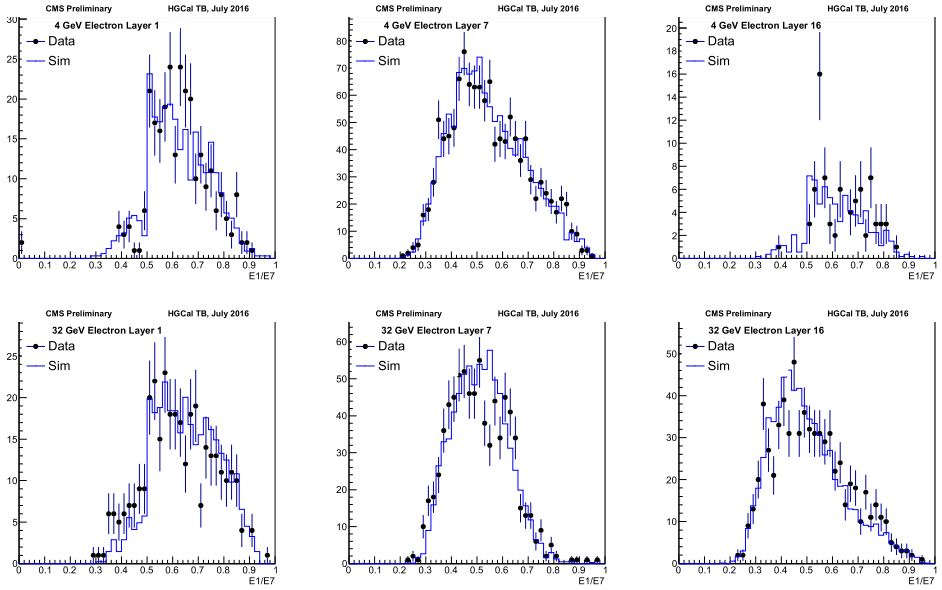

Figure 6.42: E_1/E_7 for electrons in layer 1(left), layer 7(middle) and layer 16(right). Top plots are for energy 4 GeV and bottom plots are for 32 GeV.

The energy ratios between the central (seed) cells (E1) and the total energy in 7 (E7) or 19 (E19) cells are examined to study the transverse shower shapes. Figures 6.42 and 6.43 show the distributions of E1/E7 and E1/E19 in the data and in the simulation for layer 7 for electrons of energies 4 and 32 GeV. An overall good agreement

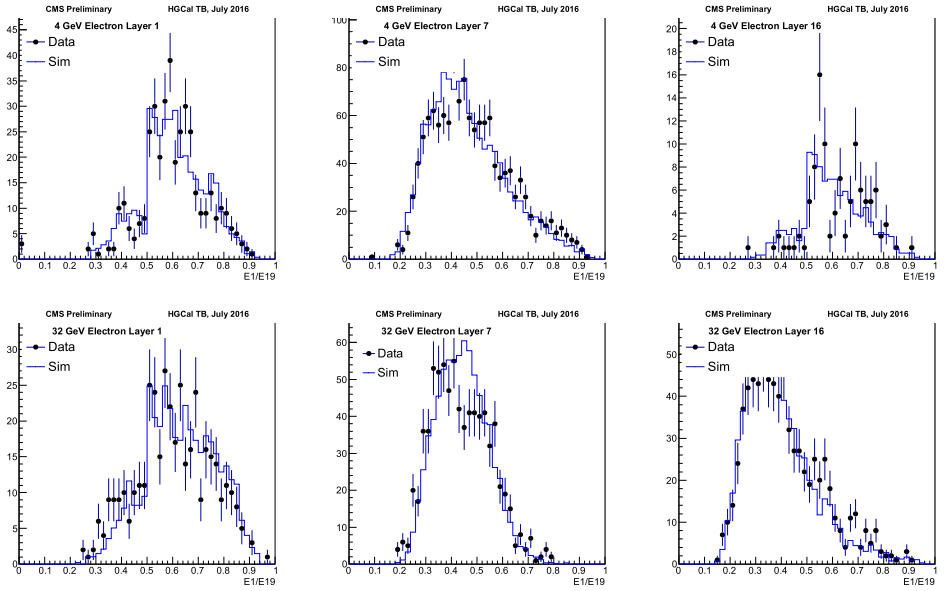

Figure 6.43: E_1/E_{19} for electrons in layer 1(left), layer 7(middle) and layer 16(right). Top plots are for energy 4 GeV and bottom plots are for 32 GeV.

between data and simulation is observed. In summary, the shower shapes measured from the data for both longitudinal and transverse profiles are well reproduced by the simulation.

6.2.5 Energy measurements and resolution

Hits with energies above 2 MIPs are selected. This corresponds to a threshold which is ∼16 times the typical intrinsic noise in a cell. The energy deposited in each active layer is obtained by summing together the energy measured by all the selected hits, with the only exception being those in the non-hexagonal cells along the edge of the sensor, which exhibit larger noise occasionally and are excluded from the analysis.

For each event, the total energy measured correspond to the sum of the energy reconstructed in the individual active layers. This energy reconstruction process is applied to both the data and the simulation for consistency. [1]

[1] Detector noise is not included in the simulation

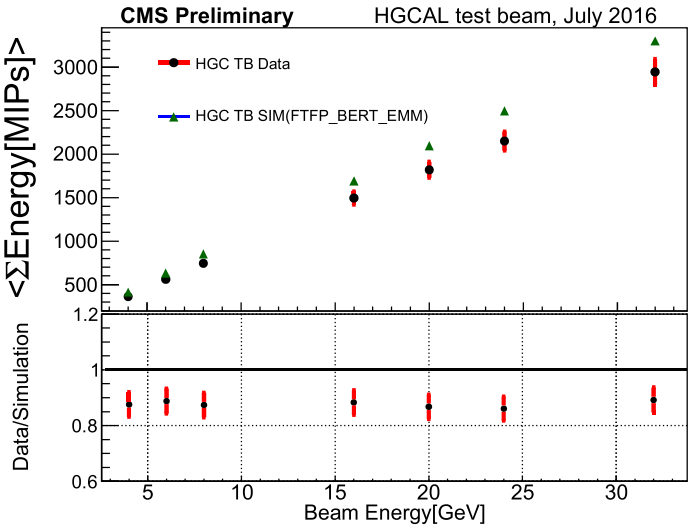

Figure 6.44: Energy reconstructed in the active layers of the detector in the data and in the simulation, expressed in units of MIPs

Figure 6.44 shows an example of the total energy measured in the active layers in units of MIPs, as a function of the beam energy. The energy measured in the simulation is about 15% above that measured in the data, after applying the reconstruction procedure as described in section 6.1.1. This offset is almost flat as a function of the energy. This difference in the energy scale may be due to the choice of a Geant4 simulation with the physics list FTFP_BERT_EMM [114], which is the one providing the best agreement in shower shapes between data and simulation (see section 6.2.4). Other lists give slightly better agreement for the overall energy scale but do not fit the data so well for the shower shapes.

Figure 6.45 shows the measured relative resolution as a function of the beam energy for both data and simulation. The simulation matches with the data at the ∼5% level for all energies.

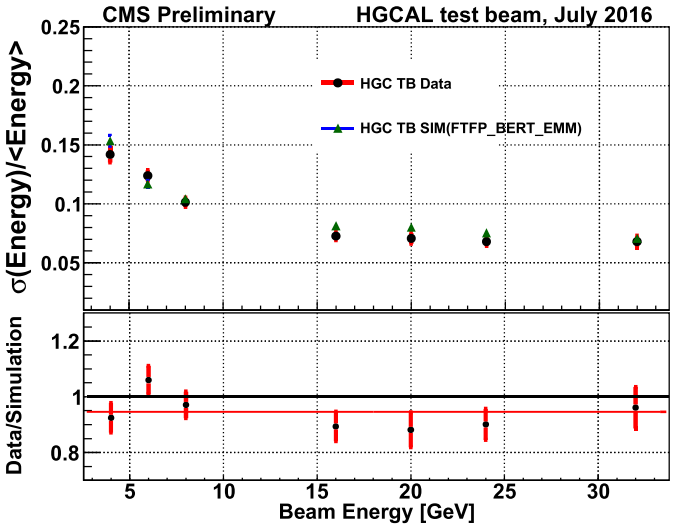

Figure 6.45: Relative energy resolution as a function of the electron energy in data and simulation.

Bibliography

[1] L. E. W. Group, "The LEP Electroweak Working Group." [Online]. Available: http://lepewwg.web.cern.ch/LEPEWWG/

[2] L. Susskind, "Dynamics of spontaneous symmetry breaking in the weinberg-salam theory," *Phys. Rev. D*, vol. 20, pp. 2619–2625, Nov 1979. [Online]. Available: https://link.aps.org/doi/10.1103/PhysRevD.20.2619

[3] D. J. Griffiths, *Introduction to elementary particles; 2nd rev. version*, ser. Physics textbook. New York, NY: Wiley, 2008. [Online]. Available: https://cds.cern.ch/record/111880

[4] M. E. P. D. V. Schroeder, *An Introduction to Quantum Field Theory*, ser. Physics textbook. Westview Press, 2004.

[5] F. Halzen and A. D. Martin, *QUARKS AND LEPTONS: AN INTRODUCTORY COURSE IN MODERN PARTICLE PHYSICS*. New York, Usa: Wiley (1984) 396p, 1984.

[6] P. B. Pal, *An introductory course of particle physics*. Boca Raton, FL: Taylor and Francis, Jul 2014. [Online]. Available: https://cds.cern.ch/record/1690642

[7] C. Patrignani *et al.*, "Review of Particle Physics," *Chin. Phys.*, vol. C40, no. 10, p. 100001, 2016.

[8] Wikipedia, "Standard Model - Wikipedia," web Page. [Online]. Available: https://en.wikipedia.org/wiki/Standard_Model

[9] E. D. Bloom, D. H. Coward, H. DeStaebler, J. Drees, G. Miller, L. W. Mo, R. E. Taylor, M. Breidenbach, J. I. Friedman, G. C. Hartmann, and H. W. Kendall, "High-energy inelastic $e-p$ scattering at 6° and 10°," *Phys. Rev. Lett.*, vol. 23, pp. 930–934, Oct 1969. [Online]. Available: https://link.aps.org/doi/10.1103/PhysRevLett.23.930

[10] M. Breidenbach, J. I. Friedman, H. W. Kendall, E. D. Bloom, D. H. Coward, H. DeStaebler, J. Drees, L. W. Mo, and R. E. Taylor, "Observed behavior of highly inelastic electron-proton scattering," *Phys. Rev. Lett.*, vol. 23, pp. 935–939, Oct 1969. [Online]. Available: https://link.aps.org/doi/10.1103/PhysRevLett.23.935

[11] O. W. Greenberg, "Spin and unitary-spin independence in a paraquark model of baryons and mesons," *Phys. Rev. Lett.*, vol. 13, pp. 598–602, Nov 1964. [Online]. Available: https://link.aps.org/doi/10.1103/PhysRevLett.13.598

[12] M. Gell-Mann, "Symmetries of baryons and mesons," *Phys. Rev.*, vol. 125, pp. 1067–1084, Feb 1962. [Online]. Available: https://link.aps.org/doi/10.1103/PhysRev.125.1067

[13] S. Weinberg, "A model of leptons," *Phys. Rev. Lett.*, vol. 19, pp. 1264–1266, Nov 1967. [Online]. Available: https://link.aps.org/doi/10.1103/PhysRevLett.19.1264

[14] R. J. Gaitskell, "Direct detection of dark matter," *Annual Review of Nuclear and Particle Science*, vol. 54, no. 1, pp. 315–359, 2004. [Online]. Available: https://doi.org/10.1146/annurev.nucl.54.070103.181244

[15] V. C. Rubin and W. K. Ford, Jr., "Rotation of the Andromeda Nebula from a Spectroscopic Survey of Emission Regions," *Astrophys. J.*, vol. 159, pp. 379–403, 1970.

[16] M. Persic, P. Salucci, and F. Stel, "Rotation curves of 967 spiral galaxies: Implications for dark matter," *Astrophys. Lett.*, vol. 33, p. 205, 1996.

[17] K. G. Begeman, A. H. Broeils, and R. H. Sanders, "Extended rotation curves of spiral galaxies: dark haloes and modified dynamics," *Monthly Notices of the Royal Astronomical Society*, vol. 249, no. 3, pp. 523–537, 1991. [Online]. Available: http://dx.doi.org/10.1093/mnras/249.3.523

[18] F. Zwicky, "On the Masses of Nebulae and of Clusters of Nebulae," *Astrophys. J.*, vol. 86, pp. 217–246, 1937.

[19] M. Girardi, G. Giuricin, F. Mardirossian, M. Mezzetti, and W. Boschin, "Optical mass estimates of galaxy clusters," *Astrophys. J.*, vol. 505, p. 74, 1998.

[20] M. Girardi, S. Borgani, G. Giuricin, F. Mardirossian, and M. Mezzetti, "Optical luminosities and mass-to-light ratios of nearby galaxy clusters," *The Astrophysical Journal*, vol. 530, no. 1, p. 62, 2000. [Online]. Available: http://stacks.iop.org/0004-637X/530/i=1/a=62

[21] D. Clowe, M. Bradac, A. H. Gonzalez, M. Markevitch, S. W. Randall, C. Jones, and D. Zaritsky, "A direct empirical proof of the existence of dark matter," *Astrophys. J.*, vol. 648, pp. L109–L113, 2006.

[22] Y. Bai, P. J. Fox, and R. Harnik, "The tevatron at the frontier of dark matter direct detection," *JHEP*, vol. 12, p. 048, 2010.

[23] P. J. Fox, R. Harnik, J. Kopp, and Y. Tsai, "Missing Energy Signatures of Dark Matter at the LHC," *Phys. Rev.*, vol. D85, p. 056011, 2012.

[24] J. Goodman, M. Ibe, A. Rajaraman, W. Shepherd, T. M. Tait *et al.*, "Constraints on Dark Matter from Colliders," *Phys.Rev.*, vol. D82, p. 116010, 2010.

[25] J. Goodman, M. Ibe, A. Rajaraman, W. Shepherd, T. M. Tait *et al.*, "Constraints on Light Majorana dark Matter from Colliders," *Phys.Lett.*, vol. B695, pp. 185–188, 2011.

[26] D. Abercrombie *et al.*, "Dark Matter Benchmark Models for Early LHC Run-2 Searches: Report of the ATLAS/CMS Dark Matter Forum," 7 2015, fERMILAB-PUB-15-282-CD.

[27] R. Bernabei *et al.*, "Final model independent result of DAMA/LIBRA-phase1," *Eur. Phys. J.*, vol. C73, p. 2648, 2013.

[28] C. E. Aalseth *et al.*, "Results from a Search for Light-Mass Dark Matter with a P-type Point Contact Germanium Detector," *Phys. Rev. Lett.*, vol. 106, p. 131301, 2011.

[29] C. E. Aalseth *et al.*, "Maximum Likelihood Signal Extraction Method Applied to 3.4 years of CoGeNT Data," 2014, arXiv 1401.6234.

[30] R. Agnese *et al.*, "Silicon Detector Dark Matter Results from the Final Exposure of CDMS II," *Phys. Rev. Lett.*, vol. 111, no. 25, p. 251301, 2013.

[31] G. Angloher *et al.*, "Results from 730 kg days of the cresst-ii dark matter search," *The European Physical Journal C*, vol. 72, no. 4, p. 1971, Apr 2012. [Online]. Available: https://doi.org/10.1140/epjc/s10052-012-1971-8

[32] T. Marrodn Undagoitia and L. Rauch, "Dark matter direct-detection experiments," *J. Phys.*, vol. G43, no. 1, p. 013001, 2016.

[33] E. Aprile *et al.*, "Dark Matter Results from 225 Live Days of XENON100 Data," *Phys. Rev. Lett.*, vol. 109, p. 181301, 2012.

[34] D. S. Akerib *et al.*, "Improved Limits on Scattering of Weakly Interacting Massive Particles from Reanalysis of 2013 LUX Data," *Phys. Rev. Lett.*, vol. 116, no. 16, p. 161301, 2016.

[35] R. Agnese *et al.*, "Search for Low-Mass Weakly Interacting Massive Particles with SuperCDMS," *Phys. Rev. Lett.*, vol. 112, no. 24, p. 241302, 2014.

[36] M. Xiao *et al.*, "First dark matter search results from the PandaX-I experiment," *Sci. China Phys. Mech. Astron.*, vol. 57, pp. 2024–2030, 2014.

[37] R. Agnese *et al.*, "New Results from the Search for Low-Mass Weakly Interacting Massive Particles with the CDMS Low Ionization Threshold Experiment," *Phys. Rev. Lett.*, vol. 116, no. 7, p. 071301, 2016.

[38] C. Amole *et al.*, "Dark Matter Search Results from the PICO-60 C_3F_8 Bubble Chamber," *Phys. Rev. Lett.*, vol. 118, no. 25, p. 251301, 2017.

[39] C. Amole *et al.*, "Dark Matter Search Results from the PICO-2L C_3F_8 Bubble Chamber," *Phys. Rev. Lett.*, vol. 114, no. 23, p. 231302, 2015.

[40] C. Amole *et al.*, "Dark matter search results from the PICO-60 CF_3I bubble chamber," *Phys. Rev.*, vol. D93, no. 5, p. 052014, 2016.

[41] C. Fu *et al.*, "Spin-Dependent Weakly-Interacting-Massive-ParticleNucleon Cross Section Limits from First Data of PandaX-II Experiment," *Phys. Rev. Lett.*, vol. 118, no. 7, p. 071301, 2017.

[42] M. G. Aartsen *et al.*, "Improved limits on dark matter annihilation in the Sun with the 79-string IceCube detector and implications for supersymmetry," *JCAP*, vol. 1604, no. 04, p. 022, 2016.

[43] S. Desai *et al.*, "Search for dark matter WIMPs using upward through-going muons in Super-Kamiokande," *Phys. Rev.*, vol. D70, p. 083523, 2004, [Erratum: Phys. Rev.D70,109901(2004)].

[44] V. Khachatryan *et al.*, "Search for new phenomena in monophoton final states in proton-proton collisions at $\sqrt{s} = 8$ TeV," *Phys. Lett.*, vol. B755, pp. 102–124, 2016.

[45] V. Khachatryan *et al.*, "Search for physics beyond the standard model in final states with a lepton and missing transverse energy in proton-proton collisions at sqrt(s) = 8 TeV," *Phys. Rev.*, vol. D91, no. 9, p. 092005, 2015.

[46] V. Khachatryan *et al.*, "Search for dark matter, extra dimensions, and unparticles in monojet events in protonproton collisions at $\sqrt{s} = 8$ TeV, " *Eur. Phys. J.*, vol. C75, no. 5, p. 235, 2015.

[47] T. Kaluza, "On the Problem of Unity in Physics," *Sitzungsber. Preuss. Akad. Wiss. Berlin (Math. Phys.)*, vol. 1921, pp. 966–972, 1921.

[48] O. Klein, "Quantum Theory and Five-Dimensional Theory of Relativity. (In German and English)," *Z. Phys.*, vol. 37, pp. 895–906, 1926, [Surveys High Energ. Phys.5,241(1986)].

[49] O. Klein, "The Atomicity of Electricity as a Quantum Theory Law," *Nature*, vol. 118, p. 516, 1926.

[50] E. Witten, "String theory dynamics in various dimensions," *Nucl. Phys.*, vol. B443, pp. 85–126, 1995.

[51] N. ArkaniHamed, S. Dimopoulos, and G. Dvali, "The hierarchy problem and new dimensions at a millimeter," *Physics Letters B*, vol. 429, no. 3, pp. 263 – 272, 1998. [Online]. Available: http://www.sciencedirect.com/science/article/pii/S0370269398004663

[52] L. Randall and R. Sundrum, "An Alternative to compactification," *Phys. Rev. Lett.*, vol. 83, pp. 4690–4693, 1999.

[53] D. J. Kapner, T. S. Cook, E. G. Adelberger, J. H. Gundlach, B. R. Heckel, C. D. Hoyle, and H. E. Swanson, "Tests of the gravitational inverse-square law below the dark-energy length scale," *Phys. Rev. Lett.*, vol. 98, p. 021101, 2007.

[54] A. A. Geraci, S. J. Smullin, D. M. Weld, J. Chiaverini, and A. Kapitulnik, "Improved constraints on non-Newtonian forces at 10 microns," *Phys. Rev.*, vol. D78, p. 022002, 2008.

[55] G. F. Giudice, R. Rattazzi, and J. D. Wells, "Quantum gravity and extra dimensions at high-energy colliders," *Nucl. Phys.*, vol. B544, pp. 3–38, 1999.

[56] T. G. Rizzo, "Pedagogical introduction to extra dimensions," *eConf*, vol. C040802, p. L013, 2004.

[57] T. Aaltonen *et al.*, "Search for large extra dimensions in final states containing one photon or jet and large missing transverse energy produced in $p\bar{p}$ collisions at $\sqrt{s} = 1.96$-TeV," *Phys. Rev. Lett.*, vol. 101, p. 181602, 2008.

[58] V. M. Abazov *et al.*, "Search for large extra dimensions in the monojet + missing e_{t} channel with the d0 detector," *Phys. Rev. Lett.*, vol. 90, p. 251802, Jun 2003. [Online]. Available: https://link.aps.org/doi/10.1103/PhysRevLett.90.251802

[59] L. E. W. Group, "Combination of lep results on direct searches for large extra dimensions," 2004, cERN Note LEP Exotica WG, 2004-03.

[60] S. Chatrchyan *et al.*, "Search for Dark Matter and Large Extra Dimensions in pp Collisions Yielding a Photon and Missing Transverse Energy," *Phys. Rev. Lett.*, vol. 108, p. 261803, 2012.

[61] A. M. Sirunyan *et al.*, "Search for new physics in the monophoton final state in proton-proton collisions at $\sqrt{s} = 13$ TeV," *JHEP*, vol. 10, p. 073, 2017.

[62] G. Aad *et al.*, "Search for new phenomena in events with a photon and missing transverse momentum in pp collisions at $\sqrt{s} = 8$ TeV with the ATLAS detector," *Phys. Rev.*, vol. D91, no. 1, p. 012008, 2015, [Erratum: Phys. Rev.D92,no.5,059903(2015)].

[63] M. Aaboud *et al.*, "Search for new phenomena in events with a photon and missing transverse momentum in pp collisions at $\sqrt{s} = 13$ TeV with the ATLAS detector," *JHEP*, vol. 06, p. 059, 2016.

[64] G. Aad *et al.*, "Search for new phenomena in final states with an energetic jet and large missing transverse momentum in pp collisions at $\sqrt{s}$ =8 TeV with the ATLAS detector," *Eur. Phys. J.*, vol. C75, no. 7, p. 299, 2015, [Erratum: Eur. Phys. J.C75,no.9,408(2015)].

[65] L. Evans and P. Bryant, "Lhc machine." *Journal of Instrumentation*, vol. 3, no. S08001, 2008. [Online]. Available: https://jinst.sissa.it/LHC/LHCmachine/2008_JINST_3_S08001.pdf

[66] "Universe Today," web Page. [Online]. Available: https://www.universetoday.com/wp-content/uploads/2008/09/lhc-sim.jpg

[67] C. Collaboration, "The cms experiment at the cern." *Journal of Instrumentation*, vol. 3, no. S08004, 2008. [Online]. Available: http://iopscience.iop.org/article/10.1088/1748-0221/3/08/S08004/pdf

[68] "Detector: CMS Experiment." [Online]. Available: https://cms.cern/detector

[69] C. Collaboration, "The cms tracker system project: technical design report." *CERN-LHCC*, vol. 006, 98. [Online]. Available: http://cdsweb.cern.ch/record/368412

[70] CMS Collaboration, "The cms tracker: addendum to the technical design report." *CERN-LHCC*, vol. 016, 2000. [Online]. Available: http://cdsweb.cern.ch/record/490194

[71] CMS Collaboration, "The electromagnetic calorimeter project: technical design report." *CERN-LHCC*, vol. 033, 97. [Online]. Available: http://cdsweb.cern.ch/record/349375

[72] S. E. e. a. PARTICLE DATA GROUP collaboration, "Review of particle physics." *Phys. Lett. B*, vol. 592, p. 1, 2004.

[73] C. Collaboration, "The hadron calorimeter project: technical design report." *CERN-LHCC*, vol. 031, 97. [Online]. Available: http://cdsweb.cern.ch/record/357153

[74] CMS Collaboration, "Cms physics technical design report volume 1: Detector performance and software." *CERN-LHCC*, vol. 001, 2006. [Online]. Available: http://cdsweb.cern.ch/record/922757

[75] CMS Collaboration, *The CMS muon project: Technical Design Report*, ser. Technical Design Report CMS. Geneva: CERN, 1997. [Online]. Available: http://cds.cern.ch/record/343814

[76] S. Chatrchyan *et al.*, "Performance of CMS muon reconstruction in pp collision events at $\sqrt{s} = 7$ TeV," *JINST*, vol. 7, p. P10002, 2012.

[77] C. Collaboration, "The tridas project, technical design report. volume 1: The level-1 trigger." *CERN-LHCC*, vol. 038, 2000. [Online]. Available: http://cdsweb.cern.ch/record/706847

[78] CMS Collaboration, "The tridas project, technical design report. volume 2: Data acquisition and high-level trigger technical design report." *CERN-LHCC*, vol. 026, 2002. [Online]. Available: http://cdsweb.cern.ch/record/578006

[79] A. M. Sirunyan *et al.*, "Particle-flow reconstruction and global event description with the CMS detector," *JINST*, vol. 12, no. 10, p. P10003, 2017.

[80] V. Khachatryan *et al.*, "Performance of Photon Reconstruction and Identification with the CMS Detector in Proton-Proton Collisions at sqrt(s) = 8 TeV," *JINST*, vol. 10, no. 08, p. P08010, 2015.

[81] V. Khachatryan *et al.*, "Performance of Electron Reconstruction and Selection with the CMS Detector in Proton-Proton Collisions at $\sqrt{s} = 8$ TeV," *JINST*, vol. 10, no. 06, p. P06005, 2015.

[82] C. Collaboration, "Isolated Photon Reconstruction and Identification at $\sqrt{s} =$ 7 TeV," 2011, cMS-PAS-EGM-10-006.

[83] M. Cacciari and G. P. Salam, "Pileup subtraction using jet areas," Phys. Lett. B **659**, 119 (2008) doi:10.1016/j.physletb.2007.09.077 [arXiv:0707.1378 [hep-ph]].

[84] CMS Collaboration, "Cut based photon id for run 2," CERN, Tech. Rep., 2016. [Online]. Available: https://twiki.cern.ch/twiki/bin/view/CMS/CutBasedPhotonIdentificationRun2

[85] CMS Collaboration, "Commissioning of the Particle-Flow reconstruction in Minimum-Bias and Jet Events from pp Collisions at 7 TeV," *CMS-PAS-PFT-10-002*, 2010.

[86] J. Alwall, R. Frederix, S. Frixione, V. Hirschi, F. Maltoni, O. Mattelaer, H. S. Shao, T. Stelzer, P. Torrielli, and M. Zaro, "The automated computation of tree-level and next-to-leading order differential cross sections, and their matching to parton shower simulations," *JHEP*, vol. 07, p. 079, 2014.

[87] T. Sjstrand, S. Ask, J. R. Christiansen, R. Corke, N. Desai, P. Ilten, S. Mrenna, S. Prestel, C. O. Rasmussen, and P. Z. Skands, "An Introduction to PYTHIA 8.2," *Comput. Phys. Commun.*, vol. 191, pp. 159–177, 2015.

[88] R. D. Ball *et al.*, "Parton distributions for the LHC Run II," *JHEP*, vol. 04, p. 040, 2015.

[89] V. Khachatryan *et al.*, "Event generator tunes obtained from underlying event and multiparton scattering measurements," *Eur. Phys. J.*, vol. C76, no. 3, p. 155, 2016.

[90] S. Agostinelli *et al.*, "GEANT4: A simulation toolkit," *Nucl. Instrum. Meth.*, vol. A506, p. 250, 2003.

[91] C. Collaboration, "Tracking and Primary Vertex Results in First 7 TeV Collisions," *CMS-PAS-TRK-10-005*, 2010.

[92] A. Askew, B. Allen, S. Bhattacharya, J. Buchanan, S. Chauhan, S. Dasu, S. Ghosh, B. Gomber, Y. Iiyama, D. Kovalskyi, C. Paus, T. Perry, A. Roy, and M. Tripathi, "Search for dark matter and large extra dimensions in monophoton final state using 2016 data", *CMS Analysis note: AN-16-224*

[93] CMS Collaboration, "Cut based electron id for run 2," CERN, Tech. Rep., 2016. [Online]. Available: https://twiki.cern.ch/twiki/bin/view/CMS/CutBasedElectronIdentificationRun2

[94] CMS Collaboration, "Baseline muon selections for run-II," CERN, Tech. Rep., 2016. [Online]. Available: https://twiki.cern.ch/twiki/bin/view/CMS/SWGuideMuonIdRun2

[95] G. Bozzi, S. Catani, G. Ferrera, D. de Florian, and M. Grazzini, "Production of Drell-Yan lepton pairs in hadron collisions: Transverse-momentum resummation at next-to-next-to-leading logarithmic accuracy," *Phys. Lett.*, vol. B696, pp. 207–213, 2011.

[96] A. Denner, S. Dittmaier, M. Hecht, and C. Pasold, "NLO QCD and electroweak corrections to W+γ production with leptonic W-boson decays," *JHEP*, vol. 04, p. 018, 2015.

[97] A. Denner, S. Dittmaier, M. Hecht, and C. Pasold, "NLO QCD and electroweak corrections to $Z+\gamma$ production with leptonic Z-boson decays," *JHEP*, vol. 02, p. 057, 2016.

[98] "ROOT webpage." [Online]. Available: https://root.cern.ch//

[99] ATLAS and CMS Collaborations, The LHC Higgs Combination Group, "Procedure for the LHC Higgs boson search combination in Summer 2011," CERN, Geneva, Tech. Rep. CMS-NOTE-2011-005. ATL-PHYS-PUB-2011-11, Aug 2011.

[100] T. Junk, "Confidence level computation for combining searches with small statistics," *Nucl. Instrum. Meth.*, vol. A434, pp. 435–443, 1999.

[101] A. L. Read, "Presentation of search results: The CL(s) technique," *J. Phys.*, vol. G28, pp. 2693–2704, 2002, [,11(2002)].

[102] A. Boveia *et al.*, "Recommendations on presenting LHC searches for missing transverse energy signals using simplified s-channel models of dark matter," arXiv:1603.04156 [hep-ex].

[103] A. Nelson, L. M. Carpenter, R. Cotta, A. Johnstone and D. Whiteson, "Confronting the Fermi Line with LHC data: an Effective Theory of Dark Matter Interaction with Photons," Phys. Rev. D **89**, no. 5, 056011 (2014) doi:10.1103/PhysRevD.89.056011 [arXiv:1307.5064 [hep-ph]].

[104] D. S. Akerib *et al.* [LUX Collaboration], "Results from a search for dark matter in the complete LUX exposure," Phys. Rev. Lett. **118**, no. 2, 021303 (2017) doi:10.1103/PhysRevLett.118.021303 [arXiv:1608.07648 [astro-ph.CO]].

[105] A. Tan *et al.* [PandaX-II Collaboration], "Dark Matter Results from First 98.7 Days of Data from the PandaX-II Experiment," Phys. Rev. Lett. **117**, no. 12, 121303 (2016) doi:10.1103/PhysRevLett.117.121303 [arXiv:1607.07400 [hep-ex]].

[106] G. Angloher *et al.* [CRESST Collaboration], "Results on light dark matter particles with a low-threshold CRESST-II detector," Eur. Phys. J. C **76**, no. 1, 25 (2016) doi:10.1140/epjc/s10052-016-3877-3 [arXiv:1509.01515 [astro-ph.CO]].

[107] K. Choi *et al.* [Super-Kamiokande Collaboration], "Search for neutrinos from annihilation of captured low-mass dark matter particles in the Sun by Super-Kamiokande," Phys. Rev. Lett. **114**, no. 14, 141301 (2015) doi:10.1103/PhysRevLett.114.141301 [arXiv:1503.04858 [hep-ex]].

[108] E. Behnke *et al.*, "Final Results of the PICASSO Dark Matter Search Experiment," Astropart. Phys. **90**, 85 (2017) doi:10.1016/j.astropartphys.2017.02.005 [arXiv:1611.01499 [hep-ex]].

[109] CMS Collaboration, "Search for new physics in the monophoton final state in proton-proton collisions at $\sqrt{s} = 13$ TeV", JHEP **1710** (2017) 073, [arXiv: 1706.03794 [hep-ex]] doi: 10.1007/JHEP10(2017)073

[110] C. Collaboration, "Technical Proposal for the Phase-II Upgrade of the CMS Detector," CERN, Geneva, Tech. Rep. CERN-LHCC-2015-010. LHCC-P-008. CMS-TDR-15-02, Jun 2015. [Online]. Available: https://cds.cern.ch/record/2020886

[111] D. W. Cooke, K. J. McClellan, B. Bennett, J. M. Roper, M. Whittaker, R. Muenchausen, and R. C. Sze, "Crystal growth and optical characterization of cerium-doped lu1.8y0.2sio5," *Journal of Applied Physics*, vol. 88, pp. 7360 – 7362, 2000.

[112] T. Kimble, M. Chou, and B. H. T. Chai, "Scintillation properties of lyso crystals," *2002 IEEE Nuclear Science Symposium Conference Record*, vol. 3, pp. 1434–1437 vol.3, Nov 2002.

[113] R.-Y. Zhu, "Cms forward calorimetry meeting," 2012, private communication, talk given at Geneva, Switzerland.

[114] "Geant4 webpage." [Online]. Available: http://geant4.cern.ch/

[115] J. B. Birks, "Scintillations from organic crystals: Specific fluorescence and relative response to different radiations," *Proceedings of the Physical Society. Section A*, vol. 64, no. 10, p. 874, 1951. [Online]. Available: http://stacks.iop.org/0370-1298/64/i=10/a=303

[116] Y. KOBA, H. Iwamoto, K. KIYOHARA, T. NAGASAKI, G. WAKABAYASHI, Y. UOZUMI, and N. MATSUFUJI, "Scintillation efficiency of inorganic scintillators for intermediate-energy charged particles," *Progress in Nuclear Science and Technology*, vol. 1, pp. 218–221, 02 2011.

[117] A. Ledovskoy, "Cms forward calorimetry taskforce meeting," 2013, private communication, talk given at CERN, Geneva, Switzerland.

[118] F.-X. Gentit, "SLitrani," web Page. [Online]. Available: https://crystalclear.web.cern.ch/crystalclear/SLitraniX/SLitrani/index.html

[119] F.-X. Gentit, "Litrani: a general purpose Monte-Carlo program simulating light propagation in isotropic or anisotropic media," web Page.

[Online]. Available: https://crystalclear.web.cern.ch/crystalclear/LitraniX/Litrani/litrani/index.html

[120] G. Grindhammer, M. Rudowicz, and S. Peters, "The fast simulation of electromagnetic and hadronic showers," *Nuclear Instruments and Methods in Physics Research Section A: Accelerators, Spectrometers, Detectors and Associated Equipment*, vol. 290, no. 2, pp. 469 – 488, 1990. [Online]. Available: http://www.sciencedirect.com/science/article/pii/016890029090566O

[121] R.-Y. Zhu, "Crystal calorimeters in the next decade," *Physics Procedia*, vol. 37, no. Supplement C, pp. 372 – 383, 2012, proceedings of the 2nd International Conference on Technology and Instrumentation in Particle Physics (TIPP 2011). [Online]. Available: http://www.sciencedirect.com/science/article/pii/S1875389212017087

[122] R.-Y. Zhu, "Cms forward calorimetry taskforce meeting," 2012, private communication, talk given at CERN, Geneva, Switzerland.

[123] A. Roy, S. Jain, S. Banerjee, S. Bhattacharya, and G. Majumder, "Simulation of 0 - separation study for proposed cms forward electromagnetic calorimeter," *Journal of Physics: Conference Series*, vol. 759, no. 1, p. 012074, 2016. [Online]. Available: http://stacks.iop.org/1742-6596/759/i=1/a=012074

[124] A. H. et al., "TMVA - toolkit for multivariate data analysis with ROOT," 2013, web Page. [Online]. Available: http://tmva.sourceforge.net/